BIO-ENABLED SYNTHESES OF FUNCTIONAL MINERAL OXIDE THIN FILMS

A Thesis

Presented to

The Academic Faculty

by

Yihong Li

In Partial Fulfillment

of the Requirements for the Degree

Master of Sciences in the

School of Materials Science and Engineering

Georgia Institute of Technology

Dec. 2013

BIO-ENABLED SYNTHESES OF FUNCTIONAL MINERAL OXIDE THIN FILMS

Approved by:

Dr. Kenneth H. Sandhage, Advisor

School of Materials Science and Engineering

Georgia Institute of Technology

Dr. David Bucknall

School of Materials Science and Engineering

Georgia Institute of Technology

Dr. E Kent Barefield

School of Chemistry and Biochemistry

Georgia Institute of Technology

Date Approved: Nov. 15, 2013

ACKNOWLEDGEMENTS

I would like to express my deepest gratitude to my advisor, Dr Kenneth H. Sandhage. I was so much influenced by his brilliant ideas and dedicated working attitude and managed to be a researcher with confidence, persistence, and consistence, as advised by Dr Sandhage. My gratitude is also to my committee members: Dr. E Kent Barefield and Dr. David Bucknall for taking the time out to guide my research and provide me help and advice.

The members in our group have also made a great contribution to my research and my life. Dr. Yunnan Fang, the person who taught and helped me a lot since I joined this group two years ago, has offered a lot of precious help in the XRD and SEM work in this thesis. Dr. Yunshu Zhang, with whom I cooperated on part of my research, is a most kind elder and friend to me, I am so grateful for all the help I got from him. Dr. Cai Ye, who offered such generous help on the TEM work of my samples, is also highly appreciated by me. My most sincere appreciation also goes to Ben Deglee and Phillip Brooke, who did part of the AFM and SEM work for me when I was extremely busy with other parts of my research work. I'd also like to give my most sincere thanks to Craig Cameron, Dan Berrigan, Brandon Goodwin, Taylor McLachlan, Ari Gordan for their technical expertise, scientific advice and willingness to discuss ideas.

Thanks to my families for their life-long support for all the way. Their encouragement and love has helped me achieve more than I could ever could have on my own. I can never imagine what my life is going to be like without my families' unconditional love and trust for me for so many years.

TABLE OF CONTENTS

LIST OF TABLES

LIST OF FIGURES

LIST OF SYMBOLS AND ABBREVIATIONS

TiBALDH	Titanium(IV) bisammoniumlactato dihydroxide
LbL	layer-by-layer
PS	polystyrene spheres
GMRs	glass microsphere resonators
2D	two dimensional
3D	three dimensional
DI	deionized
hr	hour
min	minute
Tris	tris(hydroxymethyl)aminomethane
DMSO	dimethyl sulfoxide
GMRs	glass microsphere resonators
QCM-D	quartz crystal microbalance with dissipation monitoring
AFM	atomic force microscopy
n	number of deposition cycles
ΔF	change in frequency
ΔD	change in energy dissipation
SDS	sodium dodecyl sulfate
SEM	scanning electron microscopy
TEM	transmission electron microscopy
XRD	X-ray diffraction

SUMMARY

The bio-enabled syntheses of functional nano-structured metal oxide thin films is of importance for a range of application, in photonics, electronics, sensing, cell engineering, and biochemical devices. This type of novel syntheses method can overcome problems common in conventional oxide processing. In general, conventional oxide processes often require thermal treatment, caustic chemicals, and mechanical processing when producing shape-controlled inorganic materials. In contrast, biological processes are usually carried out under mild conditions (low temperature, neutral pH, and atmospheric pressure) and are therefore promising for the development of benign processes. Functional materials synthesized at room temperature using biomolecules are promising due to their expediency. During recent years, significant progress has been made in developing new applications for such biomimetic oxide-based minerals. However, much of the research has focused on SiO- and TiO-bearing organic-inorganic hybrid materials, of which a significant limitation is that there are relatively few water-soluble inorganic oxide precursors commercially available for such biological syntheses. Two common compounds that are used in the biomimetic syntheses of SiO_2 and TiO_2 are tetramethoxisilane (TMOS) and Ti(IV)-bis(ammonium lactato) dihydroxide (TiBALDH).

As a result, approaches to synthesize new water-soluble transition metal complexes for use as precursors in the biomineralization of the corresponding functional metal oxide thin films were explored in this work, in order to expand the range of functional oxide chemistries formed via bio-enabled methods.

A Ti-containing TiBALDH-like compound was synthesized to compare the behavior of commercially-available and as-synthesized TiBALDH. Another titanium-

containing complex with citrate ligands, instead of lactate, was also synthesized to investigate the influence of the ligand type on the deposition behavior of the precursors. Zirconium- and hafnium-containing complexes were also synthesized to demonstrate the feasibility and versatility of the idea of applying bio-enabled syntheses to the fabrication of functional mineral oxides other than the reported SiO_2 and TiO_2.

The second part of this thesis focuses on developing a novel way to fabricate porous functional mineral oxide thin films with controlled pore size, which can be used in a variety of applications, such as dye loading for optical, photochemical, or electrochemical purposes. Commercially-available, carboxyl-group-terminated polystyrene spheres of different sizes were utilized as pore-size controllers in the bio-enabled syntheses of TiO_2 by protamine. This approach has been found to be an effective means of creating uniform pores in inorganic mineral oxide coatings.

The accomplishments of this work have the potential to be integrated so as to expand the boundaries of biomineralization in materials science and engineering.

CHAPTER 1: SYNTHESES, PURIFICATION, AND CHARACTERIZATION OF TI-, ZR-, HF-CONTAINING COMPLEXES

1.1 SUMMARY

In this chapter, several water-soluble, atoxic, pH- and thermally-stable, Ti(IV)-, Zr(IV)-, Hf(IV)-containing complexes were synthesized and characterized by ^{1}HNMR and ^{13}CNMR, which confirmed the presence of designed ligands on these complexes. The precursor syntheses route is demonstrated to be very simple and environmentally friendly, and could be applied to many other transition metals than Ti, Zr, and Hf. The synthesized complexes will, for the first time, be applied as precursors for the bio-inspired layer-by-layer fabrication of the corresponding inorganic oxide thin films.

1.2 INTRODUCTION

Syntheses of Water-soluble Transitional-Metal-Containing Complex Precursors

Due to the growing significance of nanocrystalline inorganic functional materials in the fields of catalysis, electronics, and energy conversion, together with the increasing demand of society for safer, softer, and "greener" technologies, considerable attention has been drawn towards water-based solution processes for the syntheses of such materials.[1-6] In this respect, complex oxides containing d_0-transition metals, such as Ti, Nb, or Ta, represent an outstanding challenge bio-enabled syntheses due to the narrow range or absence of suitable precursor compounds compatible with aqueous systems. The limited water-soluble metal-bearing anionic compounds hinder the range of materials comprising these elements that can be synthesized by water-based, bio-enabled syntheses techniques. At the same time, these elements are important as basic components of functional ceramics including photo catalysts and phosphors, which are manufactured on a large scale in industry.[7-12]

A key aspect of water-soluble, transitional-metal-containing complexes is that organic compounds are usually applied as ligands or chelating agents bonded to the metal ion, to allow for solubility in water and to control reactions leading to desired oxide precipitates and films. The organic ligands or chelating agents are often hydroxycarboxylic acids, such as lactic acid, citric acid, glycolic acid, malic acid, etc, which are biodegradable organic compounds widely present in nature.[5,6,13-26] While some work has been done on the syntheses and characterization of aqueous precursor complexes for several metal ions other than titanium, such as Mo(VI)[13], Cu(II), Zn(II) and Cd(II)[14], V(V)[15] and several lanthanides(III)[16] plus Th(IV)[17], perhaps the most

remarkable progress has been achieved in the development of new water-soluble complexes of titanium, and considerable experience has been accumulated in the application of these latter compounds for the syntheses of nanocrystalline titanium-containing oxides. Kakihanaet, et al.[18-20] have synthesized water-soluble Ti-complexes, such as a titanium-citrate complex ($[Ti_4(C_6H_4O_7)_4(O_2)_4]^{8-}$), titanium-lactate complex ($[Ti(C_3H_4O_3)_3]^{2-}$) and a titanium-glycolate complex ($[Ti_4(C_2H_2O_3)_4(C_2H_3O_3)_2(O_2)_4O_2]^{6-}$). As the water-soluble complexes have negative charge, hydrolysis by the attack of OH^- does not occur. Tomita, et al.[20] reported that their complexes could be converted selectively into nanopowders of brookite, rutile, and mixtures of rutile and anatase under hydrothermal conditions. Deng, et al.[24] reported a syntheses route to make titanium-based mixed oxides from a series of titanium(IV) citrate complexes, such as $(NH_4)_2[M(H_2O)]_6[Ti(C_6H_4O_7)_3]_2 \cdot 6H_2O$, *M*(II) = Mn, Fe, Co, Ni, Cu, and Zn.

Overall, two basic methods have been reported for the syntheses of these water-soluble precursors. The first method is a non-peroxo route, which is based on a direct reaction between either titanium tetrachloride or titanium alkoxide[27] and almost exclusively citric acid (Route A). Route A has been used for the syntheses of mononuclear titanium citrato complexes, and a representative overall reaction can be written as follows[25]:

$$TiCl_4 + 3H_4cit^* + 10OH^- \longrightarrow [Ti(cit^*)(Hcit^*)_2]^{6-} + 4Cl^- + 10H_2O \quad (1)$$

Where H_4cit^* is an abbreviation for citric acid ($C_6H_8O_7$: $CH_2COOHC(OH)(COOH)CH_2COOH$) including four possible dissociative protons; thus cit* stands for the fully deprotonated tetra-anionic form of the citrate. Titanium tetrachloride is added slowly with continuous stirring to an aqueous solution of citric acid,

followed by slow addition of an aqueous solution of either sodium hydroxide or ammonia for adjustment to the appropriate pH. The degree of deprotonation in H_4cit^* depends mainly on the pH of the solution, in addition to determining the final form of the titanium citrato complexes.[23] As the pH of the solution is increased, more highly deprotonated citric acid species are coordinated to titanium. Indeed, crystallization of $[Ti(H_2cit^*)_3]^{2-}$, $[Ti(Hcit^*)_2(H_2cit^*)]^{4-}$, $[Ti(cit^*)(Hcit^*)_2]^{6-}$, and $[Ti(cit^*)_3]^{8-}$ with several different counter-ions was confirmed at pH 2,[23] 4,[20] 6,[22] and 7,[25] respectively.

The peroxo route is based on a ligand-exchange reaction of a given hydroxo-peroxo titanium species such as $[Ti(O_2)(OH)_3]^-$ with a wide range of chelating ligands including citric acid, etc.[18-26] (Route B). In Route B, the first step involves the preparation of peroxo-hydroxo titanium complexes, such as $[Ti(O_2)(OH)_3]^-$ and $[Ti(O_2)(OH)_2]$, which can be achieved by either direct reaction between titanium tetra-chloride and hydrogen peroxide under acidic conditions (eqs. 2-4) or reaction of metallic titanium powder with hydrogen peroxide in the presence of ammonia (eq 5):

$$Ti^{4+} + H_2O_2 + H_2O \rightarrow [Ti(O_2)(OH)]^+ + 3H^+ \quad (2)$$

$$Ti^{4+} + H_2O_2 + 2H_2O \rightarrow [Ti(O_2)(OH)_2] + 4H^+ \quad (3)$$

$$Ti^{4+} + H_2O_2 + 3H_2O \rightarrow [Ti(O_2)(OH)_3]^- + 5H^+ \quad (4)$$

$$Ti + 3H_2O_2 + NH_3 \rightarrow [Ti(O_2)(OH)_3]^- + NH_4^+ + H_2O \quad (5)$$

The second step of Route B is to promote a ligand exchange reaction for $[Ti(O_2)(OH)_3]^-$, or similar types of peroxo-hydroxo titanium complexes, with an appropriate ligand. As shown in equ. 6, when citric acid is used as a chelating reagent, it reacts with the peroxo titanium complex formed in equ. 5 to produce a stable peroxo-citrato titanium complex, $[Ti_4(cit^*)_4(O_2)_4]^{8-}$:[18]

$$4[Ti(O_2)(OH)_3]^- + 4H_4cit^* \rightarrow [Ti_4(cit^*)_4(O_2)_4]^{8-} + 4H_3O^+ + 8H_2O \quad (6)$$

For these two syntheses routes, there are different choices for the ligands. The most frequently reported ligands are hydroxycarboxylic acids that can form stable complexes with titanium in aqueous solutions, including glycolic acid ($CH_2(OH)COOH$); lactic acid ($CH_3CH(OH)COOH$); malic acid ($CH_2COOHCH(OH)COOH$); tartaric acid ($CH(OH)COOHCH(OH)COOH$); citric acid ($CH_2COOHC(OH)COOHCH_2COOH$); and an aromatic hydroxycarboxylic acid, mandelic acid (C_6H_5-$CH(COOH)OH$). The resulting alkoxylato and carboxylato groups may simultaneously coordinate titanium, forming a chelate ring. The ring is responsible for the stability of the resulting complex in a given aqueous solution[13-26].

. In my work, I chose the non-peroxo route which is more environmentally- and economically-friendly. For the chelating ligands, I used lactic acid to react with $TiCl_4$ to generate a Ti(IV)-containing complex with a similar structure as commercially-available TiBALDH (titanium(IV) bisammonium-lactato-dihydroxide), a precursor which has been used widely in the bio-enabled syntheses of TiO_2.[27-30] Besides the ammonium Ti(lactate) complex, ammonium Zr(lactate) and ammonium Hf(lactate) were also synthesized through the reactions of lactic acid with the corresponding salts, $ZrCl_4$ and $HfCl_4$. To allow for a comparison with those lactates, citric acid was also chosen to react with $TiCl_4$, $ZrCl_4$, and $HfCl_4$ for the reason that citric acid has a higher chelating stability constant with Ti(IV) than lactic acid,[31,32] which would make the synthesized citrate complexes more stable than the lactates. Thus, there would be some difference between the deposition behaviors of the citrate complexes and the lactate complexes. Besides citric acid, mandelic acid was also chosen as a chelating ligand to react with $TiCl_4$, $ZrCl_4$ and

$HfCl_4$. As mandelic acid has a benzene ring on the side chain, it is much bigger in size than lactic acid. This would influence the structure of the corresponding mandelate complexes which may affect the deposition behavior of these complexes by a peptide. These synthesized lactate, citrate, and mandelate complexes were utilized in the peptide-enabled, layer-by-layer deposition of the corresponding metal oxide thin films in the next chapter.

1.3 EXPERIMENTAL PROCEDURES

The methods used to synthesize and characterize the Ti-, Zr-, Hf-containing precursors are discussed in this section.

The chemicals used in the syntheses and characterization process are as below: deionized (DI) water (18.2 MΩ·cm), methanol (99.8+% purity, Alfa Aesar, Ward Hill, MA), isopropanol (99.8+% purity, Acros, New Jersey, NJ), 28% w/w ammonum hydroxide (Alfa Aesar, Ward Hill, MA), L-lactic acid (98% purity, Alfa Aesar, Ward Hill, MA), citric acid monohydrate (99.5+% purity, Alfa Aesar, Ward Hill, MA), mandelic acid (99+% purity, Sigma-Aldrich, St. Louis, MO), titanium tetrachloride (99+% purity, Alfa Aesar, Ward Hill, MA), zirconium tetrachloride (99.5+% purity, Alfa Aesar, Ward Hill, MA), hafnium tetrachloride (99.9% purity, Alfa Aesar, Ward Hill, MA), 50% w/w TiBALDH (Ti(IV) bis-ammoniumlactato-dihydroxide, Sigma-Aldrich, St. Louis, MO), Deuterium oxide (99.8% purity, Alfa Aesar, Ward Hill, MA), and Dimethyl sulfoxide-d_6 (99.9% purity, Sigma-Aldrich, St. Louis, MO).

1.3.1 Thermal Analysis of starting reactants

To verify the purity of the starting reactants, thermal analysis was conducted on $ZrCl_4$ and $HfCl_4$. Containers with 3.2349 g $ZrCl_4$ and 3.4594 g $HfCl_4$ were heated to 800°C in a tube furnace (Lindberg / Blue M, NC USA) at a ramp rate of 3°C/min for 6 hrs (AutoFire® Controller, Orton Ceramic Foundation, OH, USA outfitted with a k-type thermocouple, OMEGA Engineering, Inc., CT, USA) in air to convert $ZrCl_4$ and $HfCl_4$ to ZrO_2 and HfO_2 to evaluate the purity of the two chlorides.

1.3.2 Syntheses and purification of Ti-containing Complexes

(1) Preparation of Ammonium Ti(lactate) Complex

L-lactic acid (2.70 g, 30.0 mmol) was placed in a flask (15 mL, Ace Glass Inc., Vineland, NJ) and dissolved in 5 mL of DI H_2O. Subsequently, titanium tetrachloride (1.90 g, 10.0 mmol) was added slowly and under continuous stirring. After reaction for 12 hrs, 28 wt% ammonia solution was then added slowly to adjust the pH to a final value of ~8.0, as measured by a pH/mV meter (UB-10, Denver Instrument, Bohemia, NY). Initially, the resulting reaction mixture was slightly cloudy. After filtration (454, Quantitative filter paper, Ashless, Fash Flow, distributed by VWR international), the resulting clear solution was kept for further use.

The same procedure was duplicated to make a second bottle of ammonium titanium lactate complex solution, which was then placed in the refrigerator at 4 °C for 12 hrs. 5.0 mL of cold isopropanol (99.8+% purity, Acros, New Jersey, NJ) at 4 °C was added into the solution until the solution became cloudy. After 2 weeks, a light-yellow solid formed in the bottle. This product was isolated by filtration (454 filter paper, Quantitative, Ashless, Fash Flow, distributed by VWR international) and dried in *vacuo* (pressure ~ $1*10^{-2}$ Pa) for 8 hrs at room temperature for subsequent solution NMR analyses.[18]

(2) Preparation of Ammonium Ti(citrate) Complex

Citric acid monohydrate (6.30 g, 30.0 mmol) was placed in a flask (15 mL, Ace Glass Inc., Vineland, NJ) and dissolved in 10 mL of DI H_2O. Subsequently, titanium tetrachloride (1.90 g, 10.0 mmol) was added slowly and under continuous stirring. The

subsequent steps were the same as for the synthesis of the ammonium Ti(lactate) complex.

(3) Preparation of Ammonium Ti(mandelate) Complex

Mandelic acid (4.56 g, 30.0 mmol) was placed in a flask (25 mL, Ace Glass Inc., Vineland, NJ) and dissolved in 10 of mL DI H_2O. Subsequently, titanium tetrachloride (1.90 g, 10.0 mmol) was added slowly and under continuous stirring. The subsequent steps were the same as for the synthesis of the ammonium Ti(lactate) complex.

(4) Preparation of Solid Powder of TiBALDH from Sigma

In order to conduct the ^{1}H and ^{13}C-NMR analyses of this TiBALDH material from Sigma-Aldrich, solid powder of TiBALDH from aqueous solution was obtained by the following method: 10 mL of isopropanol was added into a flask with 2 mL of 50 wt% TiBALDH in aqueous solution. White precipitates formed immediately once the two solutions were mixed with each other. After filtration (454 filter paper, Quantitative, Ashless, Fash Flow, distributed by VWR international) the white precipitate was collected and dried in *vacuo* (pressure ~ $1*10^{-2}$ Pa) for 8 hrs at room temperature for subsequent NMR characterization.

1.3.3 Syntheses and purification of Zr-containing Complexes

(1) Preparation of Ammonium Zr(lactate) Complex

L-lactic acid (1.80 g, 20.0 mmol) was placed in a flask (15 mL, Ace Glass Inc., Vineland, NJ) and dissolved in 5 DI mL H_2O. Subsequently, zirconium tetrachloride (2.33 g, 10.0 mmol) was added slowly and under continuous stirring. The subsequent steps were the same as for the synthesis of the ammonium Ti(lactate) complex.

(2) Preparation of Ammonium Zr(citrate) Complex

Citric acid monohydrate (6.30 g, 30.0 mmol) was placed in a flask and dissolved in 10 mL DI H_2O. Subsequently, zirconium tetrachloride (2.33 g, 10.00 mmol) was added slowly and under continuous stirring. The following steps were the same with the synthesis of ammonium Ti(lactate) complex.

(3) Preparation of Ammonium Zr(mandelate) Complex

Mandelic acid (1.52 g, 10.0 mmol) was placed in a flask and dissolved in 10 mL DI H_2O. Subsequently, zirconium tetrachloride (2.33 g, 10.0 mmol) was added slowly and under continuous stirring. The following steps were the same with the synthesis of ammonium Ti(lactate) complex.

1.3.4 Syntheses and purification of Hf-containing Complexes

(1) Preparation of Ammonium Hf(lactate) Complex

L-lactic acid (1.80 g, 20.0 mmol) was placed in a flask and dissolved in 5 mL DI H_2O. Subsequently, hafnium tetrachloride (3.20 g, 10.0 mmol) was added slowly and under continuous stirring. The following steps were the same with the synthesis of ammonium Ti(lactate) complex.

(2) Preparation of Ammonium Hf(citrate) Complex

Citric acid monohydrate (4.80 g, 30.0 mmol) was placed in a flask and dissolved in 10 mL H_2O. Subsequently, hafnium tetrachloride (2.33 g, 10.0 mmol) was added slowly and under continuous stirring. The following steps were the same with the synthesis of ammonium Ti(lactate) complex.

(3) Preparation of Ammonium Hf(mandelate) Complex

Mandelic acid (1.52 g, 10.0 mmol) was placed in a flask and dissolved in 10 mL H_2O. Subsequently, hafnium tetrachloride (3.2 g, 10.0 mmol) was added slowly and under continuous stirring. The following steps were the same with the synthesis of ammonium Ti(lactate) complex.

1.3.5 ^{1}H and ^{13}C NMR Solution Spectroscopy Characterization of Synthesized Ti-, Zr- and Hf-Complexes

For L-lactic acid, citric acid, TiBALDH from Sigma-Aldrich, and the lactate and citrate complexes, the samples for solution NMR analyses were prepared by dissolving the dried powders in D_2O, at concentrations in the range of 0.02 - 0.1 M. Because mandelic acid and the mandelate complexes possess low solubility in D_2O, they were dissolved in DMSO (dimethyl sulfoxide-d_6), at concentrations in the same range as for the lactates and citrates. NMR spectra were recorded on a Bruker AM360 (^{1}H and ^{13}C) spectrometer (Cambridge Scientific, Watertown, MA). Chemical shifts (δ) are reported in ppm, relative to an external reference of tetramethylsilane.

1.4 RESULTS AND DISCUSSION

1.4.1 Thermal analysis results of $ZrCl_4$ and $HfCl_4$

After heat treatment at 800℃ for 6 hrs, $ZrCl_4$ and $HfCl_4$ were thoroughly converted to ZrO_2 and HfO_2. The mass of ZrO_2 obtained after firing was 1.7056 g, and the mass of HfO_2 obtained after firing was 2.2681g.

The purity of starting reactant $ZrCl_4$ was calculated as below: purity of $ZrCl_4 = 1.7056 \div 123.223 \times 233.037 \div 3.2349 = 99.71\%$ (M.W. of $ZrCl_4$ 233.037 g/mol, M.W. of ZrO_2 123.223 g/mol, mass of starting $ZrCl_4$ 3.2349 g). This result matched with the purity indicated by Alfa Aesar (99.5+%).

Similarly, the purity of starting reactant $HfCl_4$ was calculated as below: purity of $HfCl_4 = 2.2681 \div 210.4909 \times 320.3048 \div 3.4594 = 99.77\%$ (M.W. of $HfCl_4$ 320.3048 g/mol, M.W. of HfO_2 210.4909 g/mol, mass of starting $HfCl_4$ 3.4594 g), this result was close to the purity indicated by Alfa Aesar (99.9%).

1.4.2 ^{1}H and ^{13}C-NMR Spectroscopy results of Ti-, Zr-, Hf-containing Complexes

Though the solid powders of the synthesized Ti-, Zr-, Hf-containing complex salts were all collected and NMR analyses were conducted on these salts, three complexes, ammonium Hf(lactate), ammonium Zr(mandelate), and ammonium Hf(mandelate), failed to display resolvable NMR spectra. All of the other precursors, (i.e., TiBALDH from Sigma, TiBALDH synthesized (ammonium Ti(lactate)), ammonium Ti(citrate), ammonium Ti(mandelate), ammonium Zr(lactate), ammonium Zr(citrate), ammonium Zr(mandelate), and ammonium Hf(citrate)), did yield resolvable NMR spectra.

For comparison, solution ^{1}H and ^{13}C NMR analyses were also conducted on the starting reacting ligands: L-lactic acid, citric acid, and mandelic acid.

Figs. 1.2 - 1.5 reveal solution ^{1}H and ^{13}C NMR spectra of citric acid, ammonium Ti(citrate), ammonium Zr(citrate), and ammonium Hf(citrate).

For citric acid, the two CH_2COOH chains are enantiotopic, but the methylene protons H_a and H_b are diastereotopic (the molecule has a plane of symmetry perpendicular to the page and passing through the central carbon, but there is no plane of symmetry passing between the protons of each methylene group and this renders proton H_a and H_b on each CH_2 group diastereotopic, see **Fig. 1.1** for proton types in citric acid below). Thus, citric acid displays an AB quartet in its ^{1}H NMR spectrum. The methylene protons, H_a and H_b, are diastereotopic. They have different chemical shifts centered at δ 2.759 ppm and δ 2.937 ppm with J = 16 Hz and show a splitting interaction, which appears as an AB pattern doublet, as shown in **Fig. 1.2.**[33] The side peak around 3.249 ppm was probably from CH_3OH[37], which may have been present in the citric acid sample as an impurity.

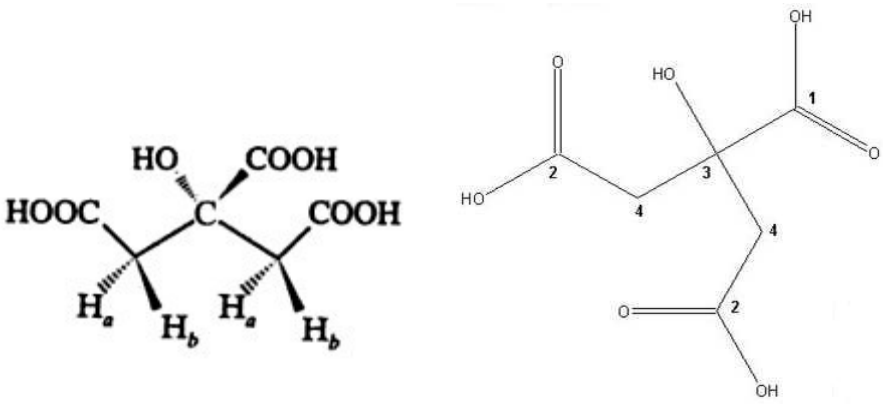

Figure 1.1: The proton and carbon types in citric acid for NMR analysis.

For the ^{13}C NMR characterization, citric acid contains four nonequivalent carbon atoms. Accordingly, in the spectra of citric acid, there should be four signals. From **Fig.**

1.2 it can be seen that in the lowest fields were located the signals of the carbon atoms of the carboxylic groups. The δ 176.52 ppm peak corresponds to the carbon atom in 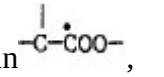 , and the δ 173.12 ppm peak to the carbon atom in the 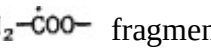 fragment[38]. At higher field, a signal δ 43.04 ppm was observed for the methylene carbon atoms, while a signal at δ 73.04 ppm corresponded to the quaternary carbon atom[38]. The peak at δ 48.61 ppm was likely due to the carbon atom in methanol[37], which is consistent with the peak observed in the ^{1}H NMR spectrum.

For ammonium Ti(citrate), **Fig. 1.3** shows that there is an AB pattern centered at δ 2.452 ppm and 2.561 ppm, with J = 15 Hz, similar to the quartet of peaks for free citric acid ligand, but shifted to higher field by about 0.287 ppm, which may be due to the coordination of the ligand with the metal atom[34]. The peak at δ 3.256 ppm for methanol was present in this spectrum, which has shifted very little with respect to the spectrum for citric acid. The ^{13}C NMR spectrum in **Fig. 1.3** also showed the four representative signals of a citrate ligand at δ 181.66 ppm, δ 178.94 ppm, δ 74.94 ppm, and δ 45.35 ppm. However, comparing with the peaks of free citric acid, the peaks have shifted (δ 43.04 ppm, δ 73.04 ppm, δ 173.12 ppm, δ 176.52 ppm) to lower fields (δ 45.35 ppm, δ 74.94 ppm, δ 178.94 ppm, δ 181.66 ppm). The peak for methanol was not present in the ^{13}C NMR spectrum of ammonium Ti(citrate). The concentration of methanol in this sample was apparently too low for detection.

For ammonium Zr(citrate) in **Fig. 1.4** of the ^{1}H NMR spectrum, the AB pattern for the CH_2 group in citric acid was shifted about 0.304 ppm to higher field, with J = 15.5 Hz, in a manner similar to that observed for ammonium Ti(citrate). The ^{13}C NMR

spectrum exhibited four signals corresponding to the four types of carbon in the citrate, δ 181.83 ppm, δ 179.15 ppm, δ 75.01 ppm, δ 45.49 ppm, which were also shifted to lower fields when compared with free citric acid. The ^{1}H and ^{13}C NMR spectra in **Fig. 1.5** revealed a similar case for ammonium Hf(citrate). Thus, we can conclude that the citrate ligand was bound to the metal ion in these complexes, although we cannot determine the number of citrate residues or other ligands associated with the metal ions.

The solvent peaks for D_2O in **Figs. 1.2 – 1.5** were all at about 4.71 ppm[37], shown below as peaks with the highest intensity.

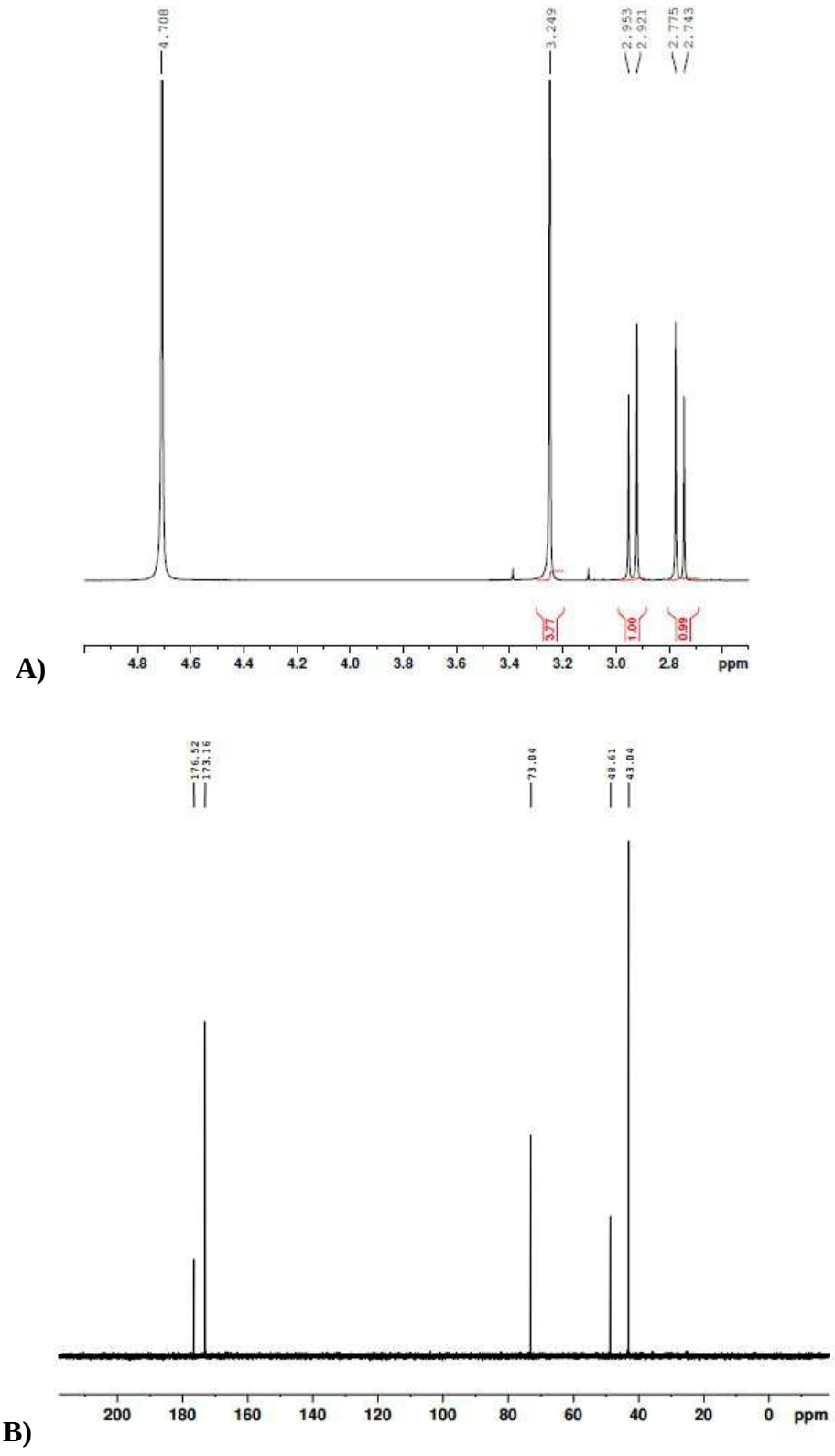

Figure 1.2: Solution ^{1}H NMR (A), ^{13}C NMR (B) spectra of the starting reactant citric acid in D_2O

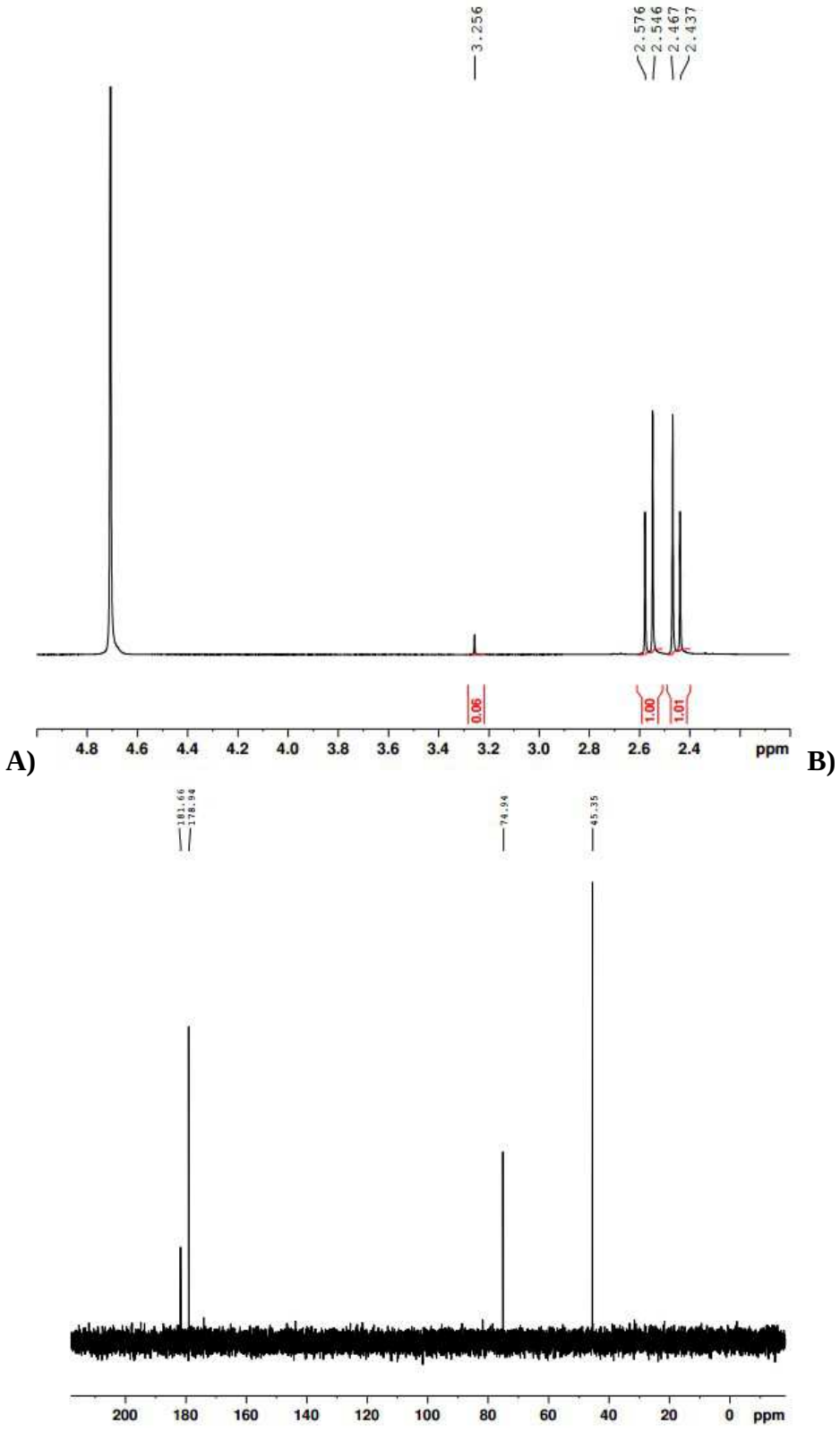

Figure 1.3: Solution ^{1}H NMR (A), ^{13}C NMR (B) spectra of the ammonium Ti(citrate) complex in D_2O

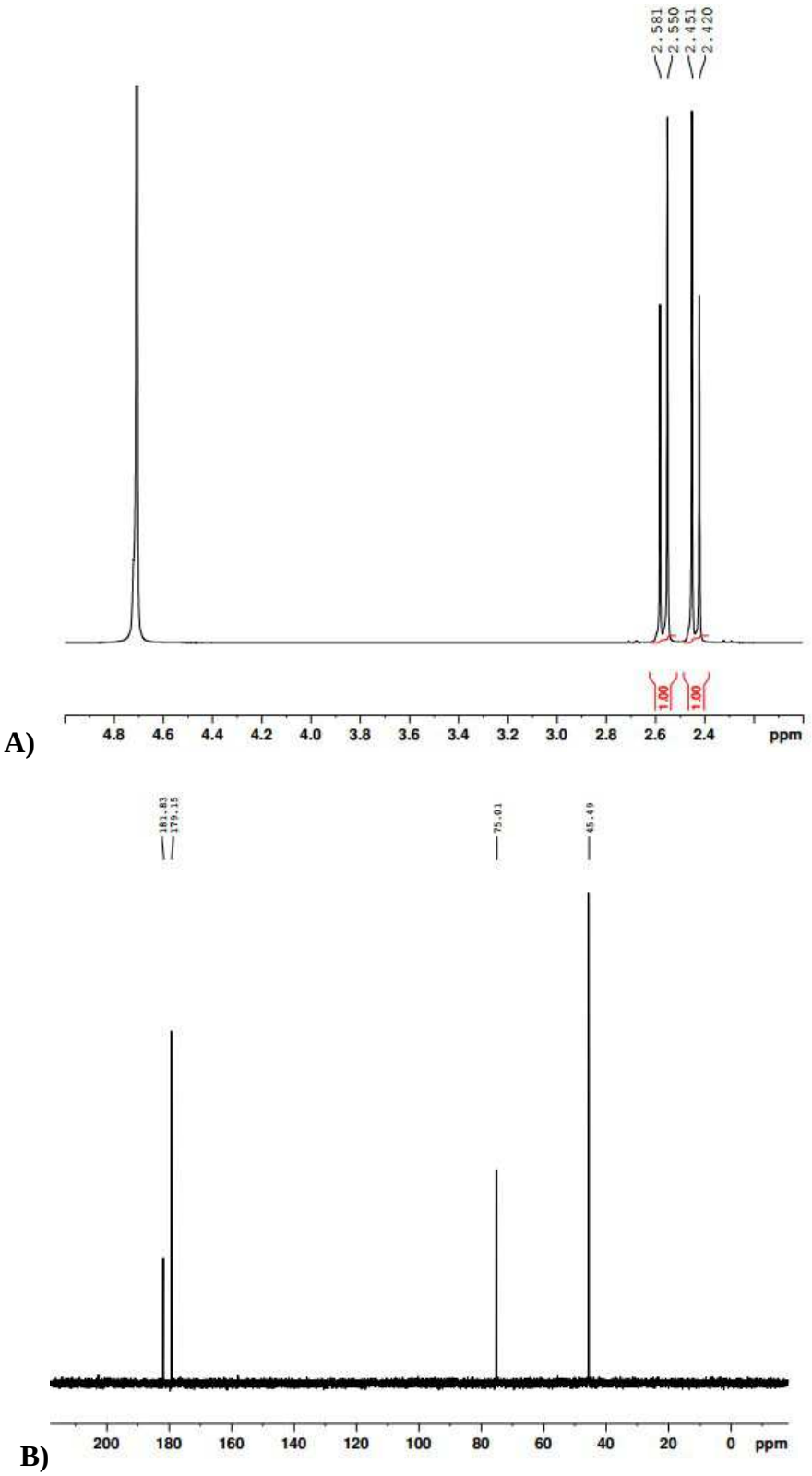

Figure 1.4: Solution ^{1}H NMR (A), ^{13}C NMR (B) spectra of the ammonium Zr(citrate) complex in D_2O

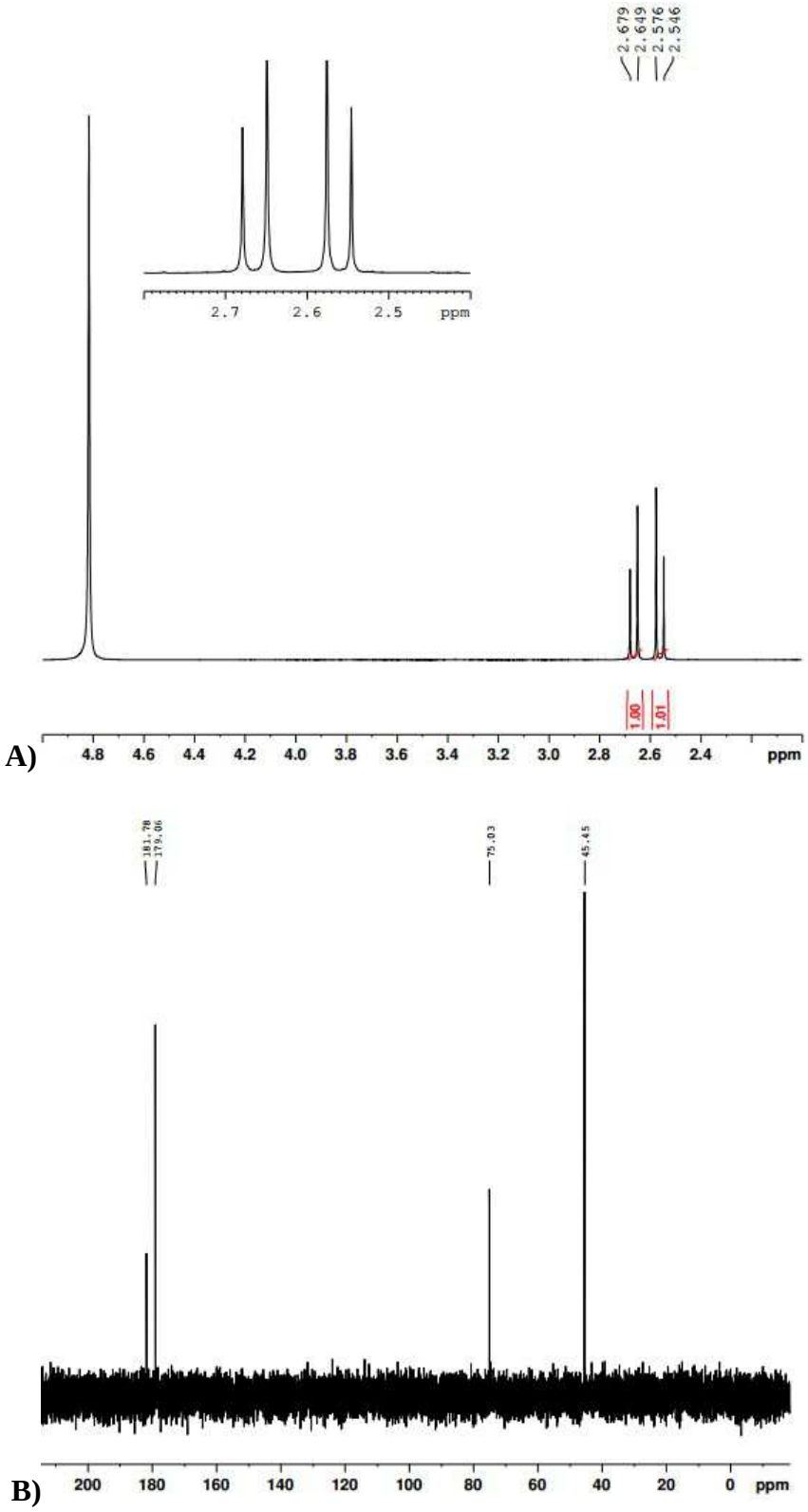

Figure 1.5: Solution ^{1}H NMR (A), ^{13}C NMR (B) spectra of the ammonium Hf(citrate) complex in D_2O

Fig. 1.7 - 1.10 are solution ^{1}H and ^{13}C NMR spectra of L-lactic acid, TiBALDH from Sigma, synthesized TiBALDH (i.e., ammonium Ti(lactate), and ammonium Zr(lactate).

For lactic acid, as shown in **Fig. 1.7**, the chemical shifts of non-equivalent methyl and tertiary C-H gave rise to a quartet centered at δ 4.266 ppm with J = 7 Hz, and a doublet at δ 1.302 ppm with J = 7 Hz (for the active protons would exchange with D_2O solvent and would not appear in the spectrum[33]). For ^{13}C NMR spectroscopy, there are 3 nonequivalent carbons in the L-lactic acid. C_1 corresponds to the peak at the highest field, δ 19.01 ppm, C_2 at δ 66.16 ppm, and C_3 at the lowest field, δ 178.34 ppm.[35]

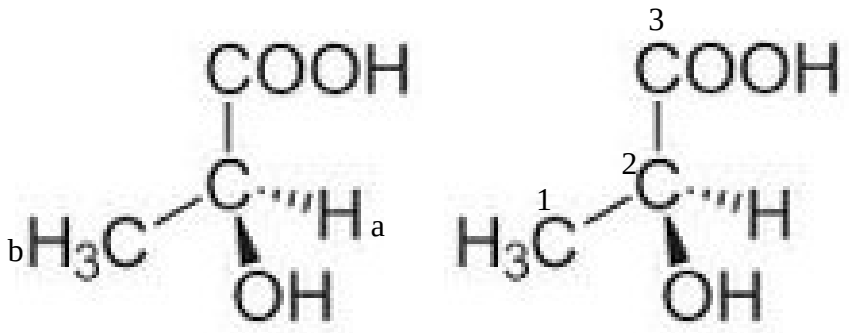

Figure 1.6 : The proton and carbon types in L-lactic acid for NMR analysis.

For TiBALDH from Sigma, **Fig. 1.8** shows that the solvent peak has shifted from δ 4.71 ppm to δ 5.326 ppm, after adjusting the other peaks by substracting this shift, the quartet was at δ 4.021 ppm with J = 7 Hz. Compared with the quartet of free L-lactic acid, these have shifted to higher fields by around 0.245 ppm, which may due to the coordination of the ligand with the metal atom. The doublet was at δ 1.235 ppm with J = 7 Hz. Compared with the doublet of free L-lactic acid, these peaks have shifted to higher

fields by around 0.067 ppm (i.e., a small shift comparing to the quartet). There are also some side peaks around the doublet, but the concentrations of the proton associated with these side peaks was very low compared with doublet proton. The ^{13}C NMR spectrum in **Fig. 1.8** also showed the three representative signals of a lactate ligand, at δ 182.81 ppm, δ 68.84 ppm, and δ 20.42 ppm. Comparing with the peaks of free L-lactic acid, the peaks have shifted (δ 19.01 ppm, δ 66.16 ppm, δ 178.34 ppm.) to lower fields (δ 20.42 ppm, δ 68.84 ppm, δ 182.81 ppm). There is also a side peak at δ 82.63 ppm.

For synthesized TiBALDH (i.e., ammonium Ti(lactate)) in **Fig. 1.9**, similar with commercial TiBALDH, the solvent peak had shifted from 4.71 ppm to 5.326 ppm. By substracting the shift from the proton peaks, the quartet was at δ 4.024 ppm with J = 7 Hz. Compared with the quartet of free L-lactic acid, these peaks have shifted to higher fields by around 0.242 ppm, which may due to the coordination of the ligand with the metal atom. The doublet was at δ 1.238 ppm with J = 7 Hz. Compared with the doublet of free L-lactic acid, these peaks have shifted to higher fields by around 0.064 ppm (i.e., a small shift comparing to the quartet). The ^{13}C NMR spectrum in **Fig. 1.9** for synthesized TiBALDH also exhibited the three representative signals of a lactate ligand at δ 182.80 ppm, δ 68.83 ppm, and δ 20.42 ppm. Comparing with the peaks of free L-lactic acid, these peaks have shifted (δ 19.01 ppm, δ 66.16 ppm, δ 178.34 ppm) to lower fields (δ 20.42 ppm, δ 68.83 ppm, δ 182.80 ppm).

For ammonium Zr(lactate) in **Fig. 1.10**, the case was quite similar, though there were more peaks unaccounted for in the spectrum. The solvent peak had shifted very little in the ^{1}H NMR spectrum, and the quartet was at δ 4.063 ppm with J = 7 Hz.

Compared with the quartet of free L-lactic acid, these peaks have shifted to higher fields by around 0.203 ppm, which may due to the coordination of the ligand with the metal atom. The doublet was at δ 1.250 ppm with J = 7 Hz. Compared with the doublet of free L-lactic acid, these peaks have shifted to higher fields by around 0.052 ppm (i.e., a small shift comparing to the quartet). There are also several low intensity resonances in the ^{1}H NMR spectrum due to impurities in the complex sample. The ^{13}C NMR spectrum in **Fig. 1.10** for ammonium Zr(lactate) has a peak at δ 188.30 ppm, which would correspond to the carbon in -COO- (shifting from δ 178.34 ppm in free lactic acid). There is also a peak located at δ 19.76 ppm with the strongest intensity, which corresponds to carbon in $-CH_3$ (little shift comparing with that peak of free L-lactic acid at δ 19.01 ppm). The peak for carbon in -CH- has been shifted from δ 66.16 ppm to δ 82.01 ppm, which means the complexation of the ligand with the Zr atom would affect the chemical environment of carbon in -CH- greatly. Besides the peaks for the lactate ligand, there are also several peaks in ^{13}C NMR spectrum of ammonium Zr(lactate) due to unknown substances, which indicates that further purification work should be conducted for this precursor in the future.

Thus, we can conclude from the above analyses that the lactate ligand does exist in the complexes (i.e., TiBALDH from Sigma, synthesized TiBALDH, ammonium Zr(lactate)), while future characterization is needed to determine the number of ligands and complexation status of the ligands with the metal atoms.

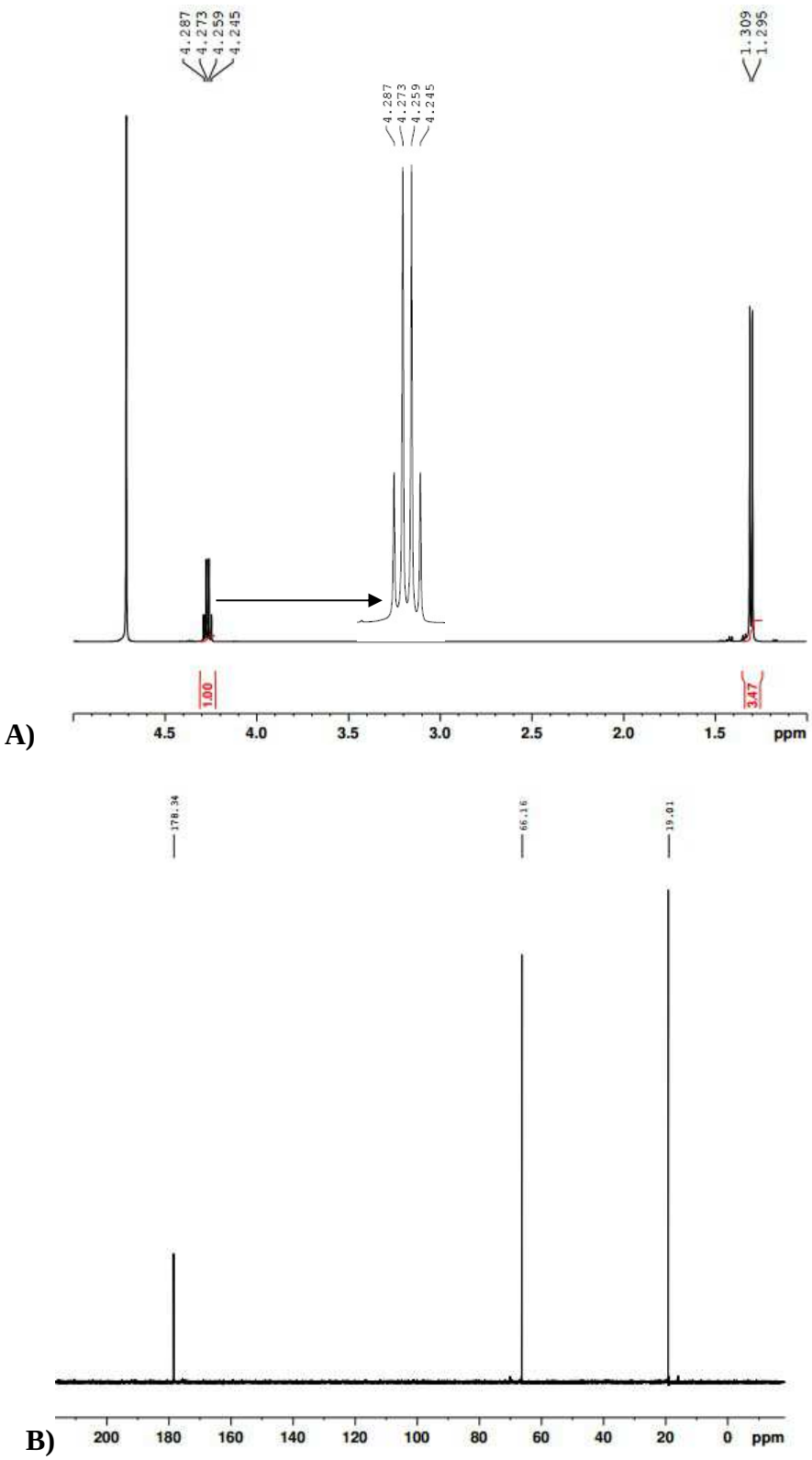

Figure 1.7: Solution ^{1}H NMR (A), ^{13}C NMR (B) spectra of the starting reactant L-lactic acid in D_2O

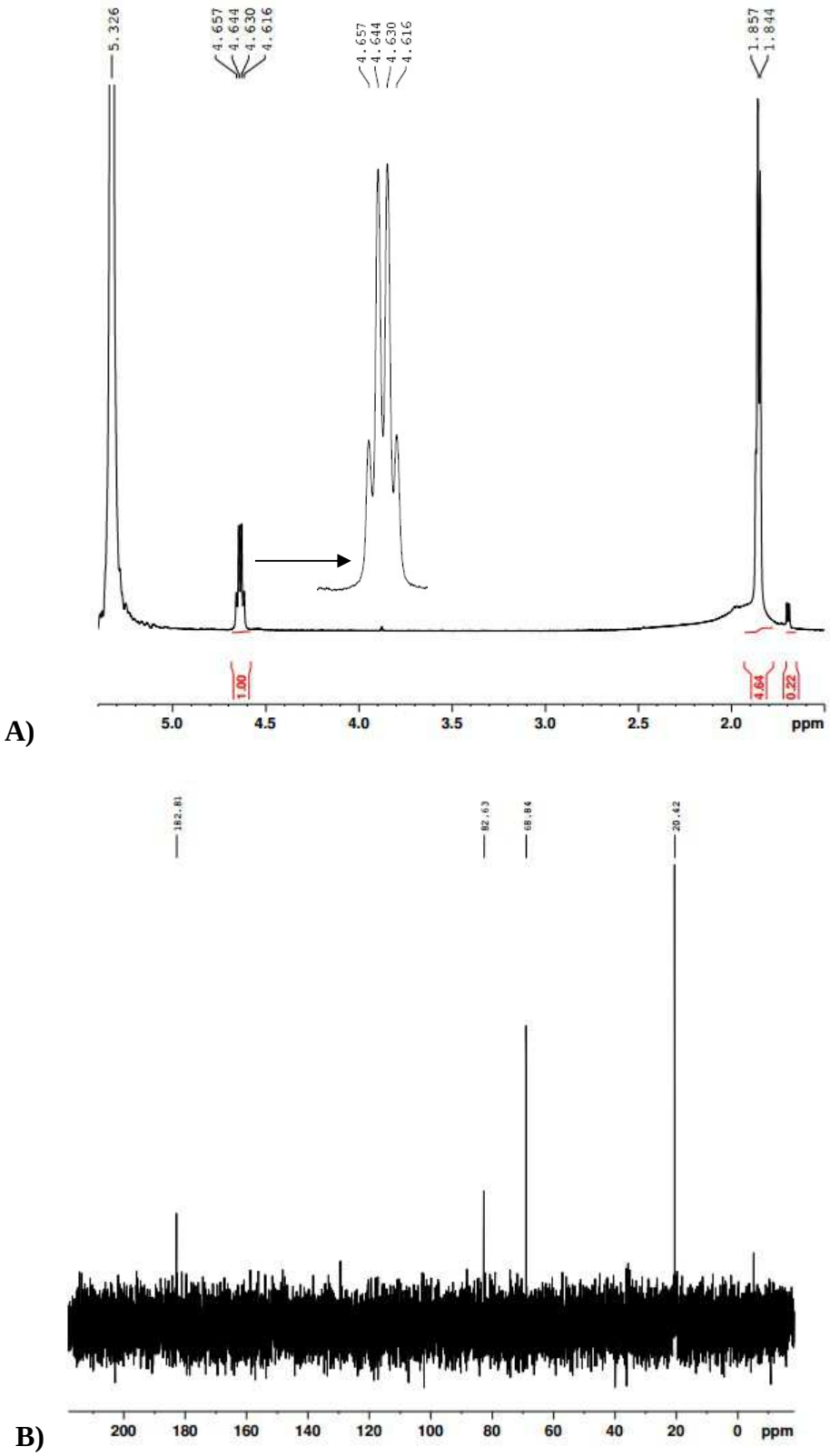

Figure 1.8: Solution ^{1}H NMR (A), ^{13}C NMR (B) spectra of the TiBALDH from Sigma in D_2O

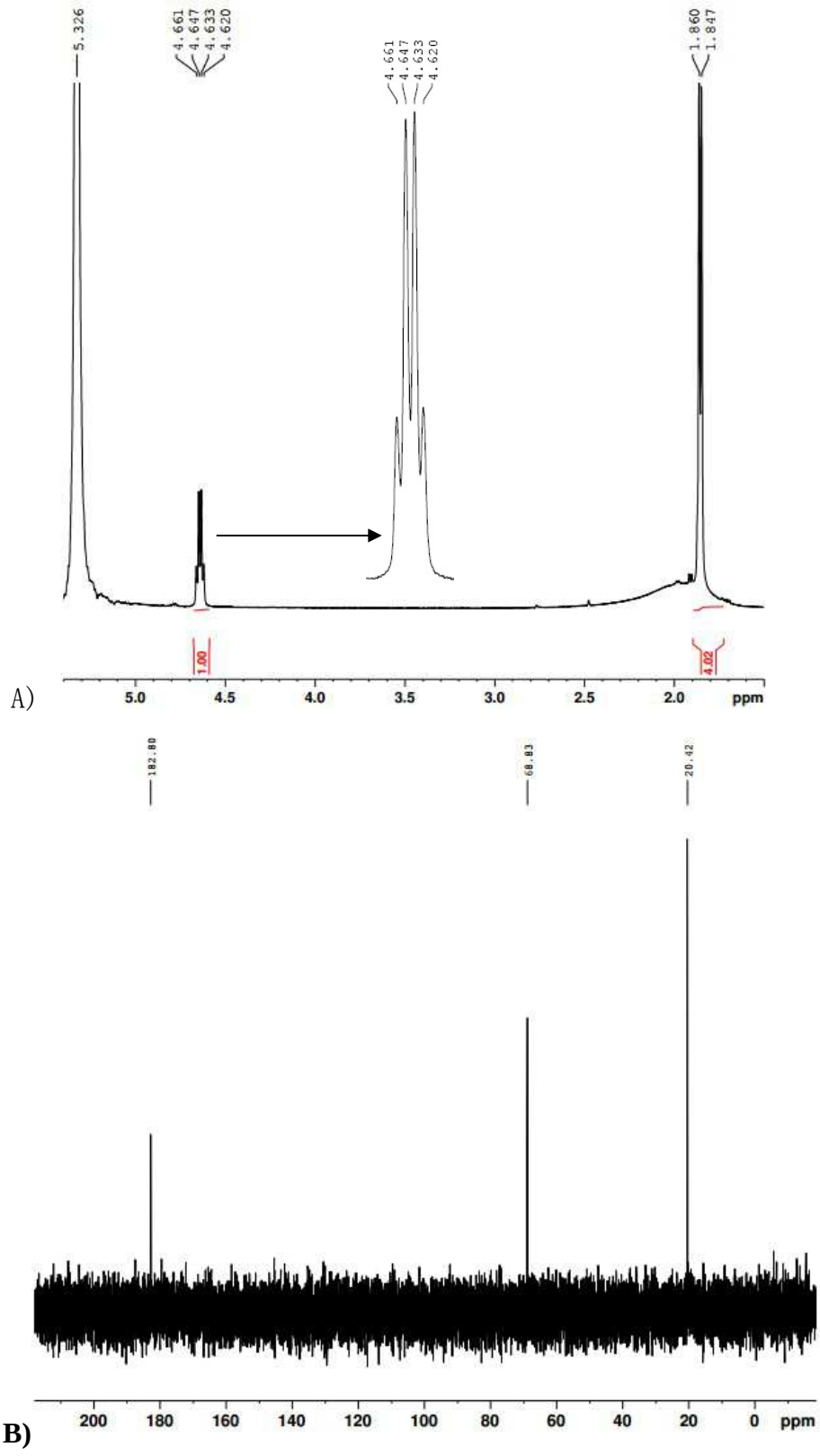

Figure 1.9: Solution ^{1}H NMR (A), ^{13}C NMR (B) spectra of the synthesized TiBALDH (i.e. ammonium Ti(lactate)) in D_2O.

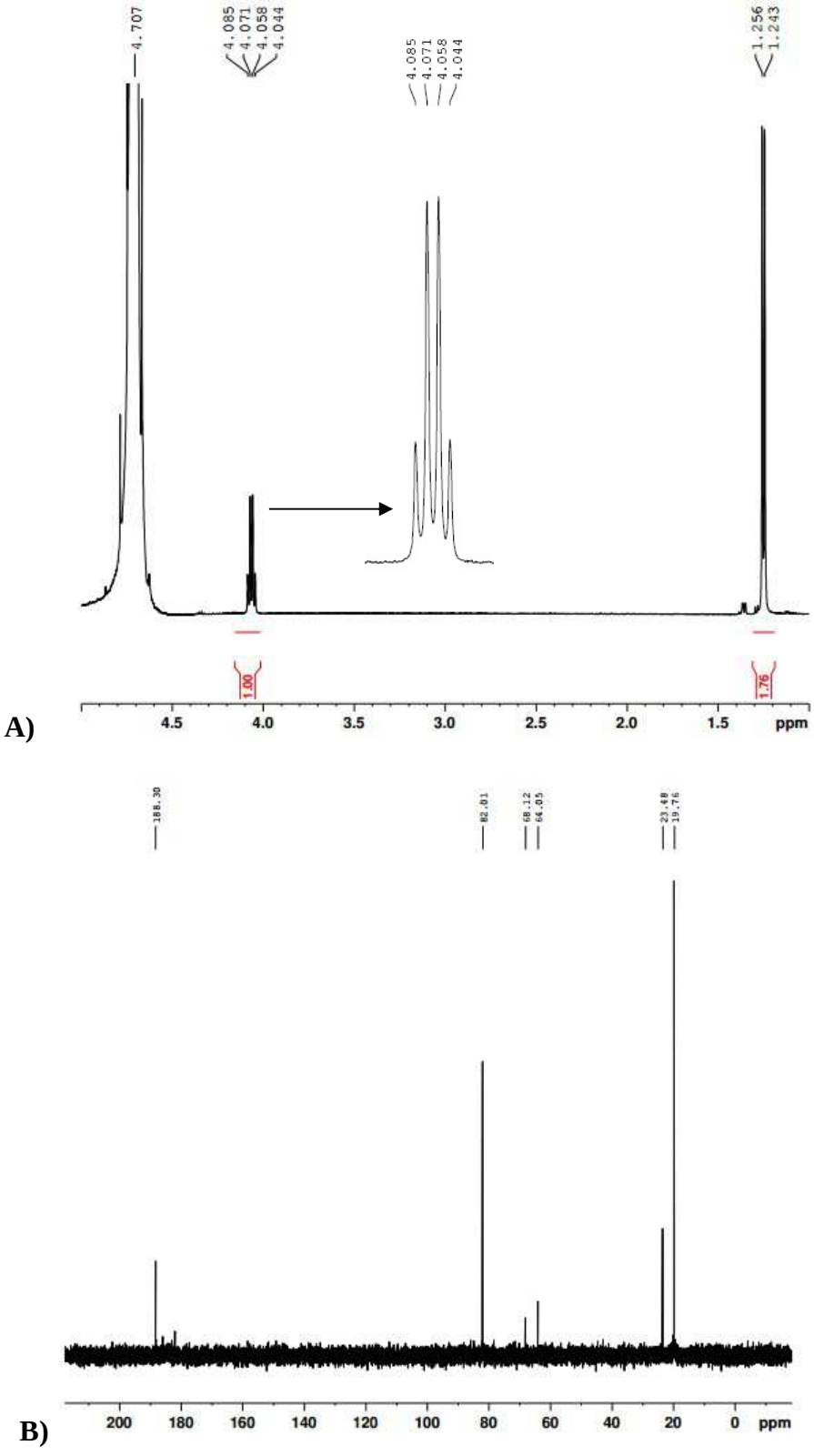

Figure 1.10: Solution ^{1}H NMR (A), ^{13}C NMR (B) spectra of the ammonium Zr(lactate) in D_2O

For mandelic acid, there are four types of non-equivalent protons except for protons in -OH and -COOH, as shown in **Fig. 1.11**. It can be seen from **Fig. 1.12** that the solvent peak for DMSO had shifted from δ 2.50 ppm[36] to δ 4.723 ppm. By adjusting the shifts, the singular peak at δ 5.034 ppm (originally at δ 7.257 ppm) corresponded to H_a in -CH-. The multiplet centered at δ 7.731 ppm (originally at 9.584) corresponded to three types of protons on the benzene ring (i.e., H_b, H_c, and H_d) which are spin-coupled to each other.[37] As DMSO is a solvent with low polarity, the active protons in -OH and -COOH would also have peaks in the spectrum. In **Fig. 12**, the broad peak at about δ 12.613 ppm after adjusting (originally at about δ 14.836 ppm) corresponded to the proton in -COOH, and the broad peak at about δ 6.851 ppm after adjusting (originally at about δ 8.074 ppm) corresponded to the proton in -OH. For ^{13}C NMR spectroscopy, there are 6 nonequivalent carbons in the mandelic acid as shown in **Fig. 1.11**. C_1 corresponded to the peak in lower field, δ 174.4 ppm, C_6 to δ 72.67 ppm, C_2 corresponded to the peak at δ 140.5 ppm, and C_3, C_4 and C_5 corresponded to the peaks from δ 126.92 ppm and 128.42 ppm.[37] The set of multiplet peaks from δ 39.41 ppm to 40.08 ppm corresponded to the carbon peaks from the solvent DMSO.[35]

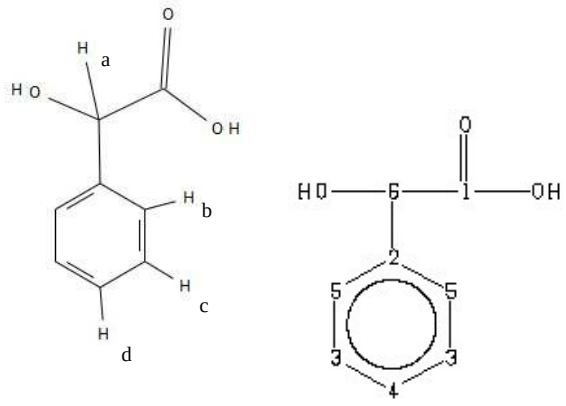

Figure 1.11: The proton and carbon types in mandelic acid in for NMR analysis.

For the ^{1}H NMR spectrum of ammonium Ti(mandelate), **Fig. 1.13** reveals a multiplets centered at δ 7.423 ppm, which indicated the existence of the benzene ring in the complex.[37] There was also a singular peak at about δ 5.586 ppm corresponding to the proton in -CH-,[37] and a peak at δ 2.513 for the solvent proton[35]. From this spectrum, many peaks with high intensity can be seen which don't belong to the mandelate ligand, which means that the purity of the ammonium Ti(mandelate) was not high. From the ^{13}C NMR spectrum in **Fig. 1.13**, the peak at δ 182.67 ppm, which shifted from δ 174.4 ppm for free mandelic acid, corresponded to the carbon in -COO-. The peaks at δ 144.36, δ 127.07ppm and 127.62 ppm were the signature peaks for benzene rings, which coincided with the ^{1}H NMR spectrum quite well. The peak at δ 73.40 ppm, shifting from δ 72.67 ppm for free mandelic acid, corresponded to the carbon in -CH-.[37] The solvent peaks are from δ 39.61 ppm to δ 39.94 ppm[35]. Besides these peaks, there were still three side peaks present in the spectra, which indicated that the ammonium Ti(mandelate) solution contained has other impurities. Further purification work is needed for this precursor. From the above analysis of the ^{1}H NMR and ^{13}C NMR spectra, the mandelate ligand does exist in the ammonium Ti(mandelate) precursor. Future purification and characterization work needs to be conducted to determine the number of ligands and complexation status of the ligands with the Ti atom.

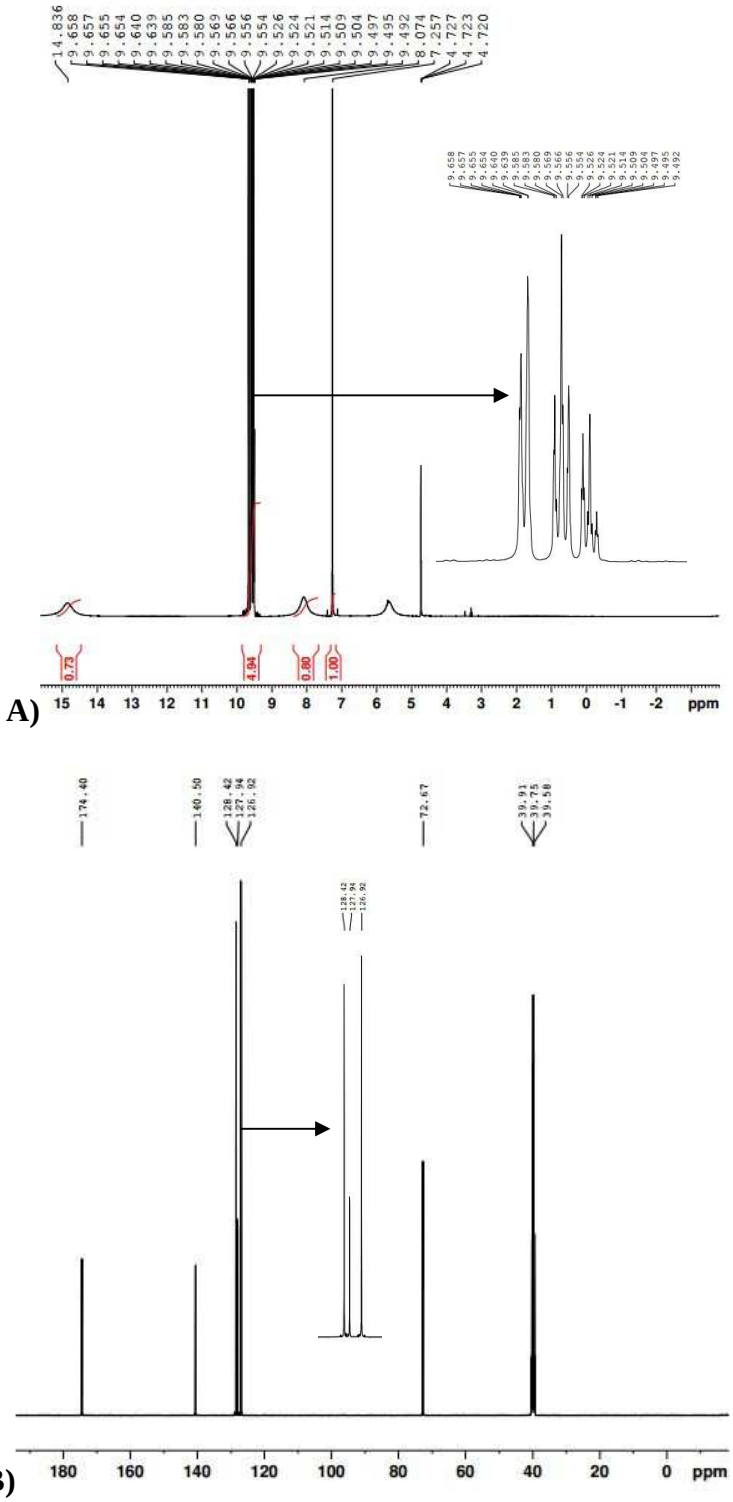

Figure 1.12: Solution ^{1}H NMR (A), ^{13}C NMR (B) spectra of the starting reactant mandelic acid in DMSO.

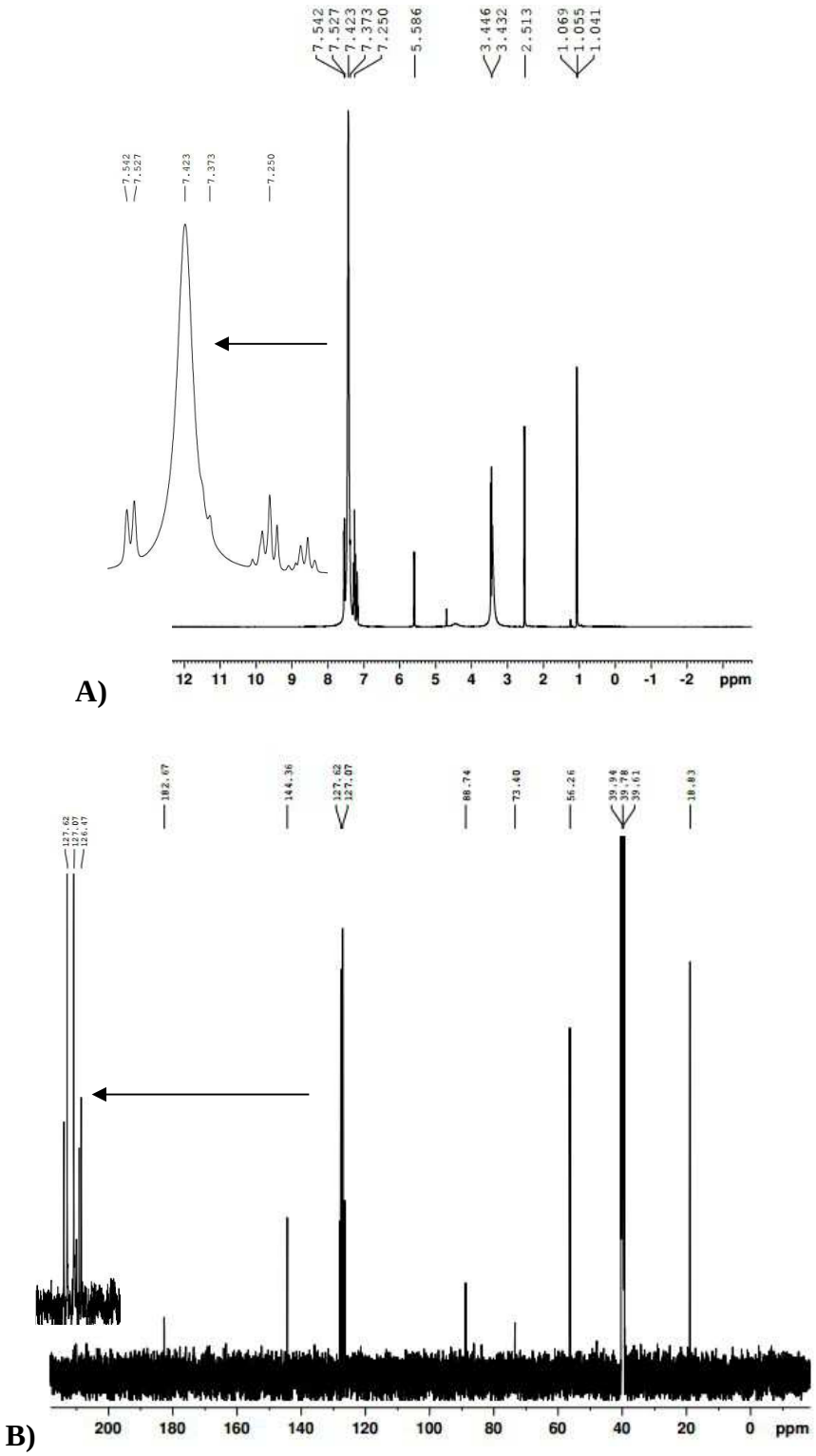

Figure 1.13: Solution ^{1}H NMR (A), ^{13}C NMR (B) spectra of the ammonium Ti(mandelate) in DMSO.

1.5 SUMMARY AND OUTLOOK

In this work, several Ti-, Zr- and Hf-containing complexes with different types of ligands were synthesized. Solution ^{1}H and ^{13}C NMR spectroscopic analyses were conducted on these complexes. The NMR spectroscopic analyses of ammonium Ti(lactate), ammonium Ti(citrate), ammonium Ti(mandelate), ammonium Zr(lactate), ammonium Zr(citrate), ammonium Hf(citrate) indicated that these complexes did possess the desired ligands. But for some precursors (i.e., TiBALDH from Sigma, ammonium Zr(lactate), ammonium Ti(mandelate)), the NMR spectra indicated that they were not pure (i.e., there were some side peaks which could not be attributed to the ligands of there complexes). Thus, work is left to future researchers to further purify these complexes. Moreover, solution ^{1}H and ^{13}C NMR analyses were not able to unambiguously determine the structure of those complexes. Additional characterization work, such as FT-IR, element analysis, TGA, XRD, etc, is needed on these complexes. For ammonium Zr(mandelate), ammonium Hf(lactate), ammonium Hf(mandelate), NMR spectra were not obtained.

All the complexes synthesized here were utilized in the next chapter in the peptide-enabled, layer-by-layer deposition of the corresponding functional mineral oxide thin films. With the syntheses route used in this chapter for metal-containing complexes, and the potential of these complexes to be utilized as precursors in peptide-enabled layer-by-layer deposition process, a variety of other functional mineral oxide thin films may be fabricated for multiple applications in scientific and engineering fields.

1.6 REFERENCES

[1] B. Oregan and M. Grätzel, "A low-cost, high-efficiency solar cell based on dye-sensitized colloidal TiO_2 films", *Nature*, 1991, **353**, 737.

[2] L.R. Skubal, N.K. Meshkov and M.C. Vogt, "Detection and identification of gaseous organics using a TiO_2 sensor", *J. Photochem. Photobiol. A*, 2002, **148**, 103.

[3] A.G. Agrios and P. Pichat, "State of the art and perspectives on materials and applications of photocatalysis over TiO_2", *J. Appl. Electrochem.* 2005, **35**, 655.

[4] A. Fujishima and K. Honda, "Electrochemical photolysis of water at a semiconductor electrode", *Nature,* 1972, **238**, 37.

[5] K. Tomita, M. Kobayashi, V. Petrykin, S. Yin, T. Sato, M. Yoshimura and M. Kakihana, "Hydrothermal synthesis of TiO_2 nano-particles using novel water-soluble titanium complexes", *J. Mater. Sci.* 2008, **43**, 2217.

[6] K. Yamamoto, K. Tomita, K. Fujita, M. Kobayashi, V. Petrykin and M. Kakihana, "Synthesis of TiO_2 using glycolato titanium complex and post-synthetic hydrothermal crystal growth of TiO_2", *J. Cryst. Growth,* 2009, **311**, 619.

[7] R. C. Mehrotra, and A. Singh, "Chemistry of oxo-alkoxides of metals", *Chem. Soc. Rev*. 1996, 1.

[8] L. G. Hubert-Pfalzgraf, "Some trends in the design of homo- and heterometallic molecular precursors of high-tech oxides", *Inorg. Chem. Commun.*, 2003, **6**, 102.

[9] S. Doeuff, Y. Dromzee, F. Taulelle, and C. Sanchez, "Synthesis and solid- and liquid-state characterization of a hexameric cluster of titanium(IV): $Ti_6(.mu._2\text{-}O)_2(.mu._3\text{-}O)_2(.mu._2\text{-}OC_4H_9)_2(OC_4H_9)_6(OCOCH_3)_8$", *Inorg. Chem.*, 1989, **28**, 4439.

[10] T. J. Boyle, T. M. Alam, C. J. Tafoya, and B. L. Scott, "Formic acid modified $Ti(OCHMe_2)_4$. Syntheses, characterization, and x-ray Structures of $Ti_4(\mu_4\text{-}O)(\mu\text{-}O)(OFc)_2(\mu\text{-}OR)_4(OR)_6$ and $Ti_6(\mu_3\text{-}O)_6(OFc)_6(OR)_6$ (OFc = O_2CH; OR = $OCHMe_2$)", *Inorg. Chem.*, 1998, **37**, 5588.

[11] T. M. Alam, T. J. Boyle, C. D. Buchheit, R. W. Schwartz, and J. W. Ziller, "Formation, structure, and material properties from the reaction product of $M(OCHMe_2)_4$ (M=Ti, Zr) and HOAc", *Mater. Res. Soc. Symp. Proc.*, 1994, **346**,35.

[12] R. Papiernik, L. G. Hubert-Pfalzgraf, J. Vaissermann, and M. C. H. B. Goncalves, "Synthesis and characterization of new titanium hexanuclear oxo carboxylato alkoxides. Molecular structure of $[Ti_6(\mu_3\text{-}O)_6(\mu\text{-}O_2CC_6H_4OPh)_6(OEt)_6]$", *Dalton Trans.*, 1998, 2285.

[13] A. Cuin and A.C. Massabni, "Synthesis and characterization of solid molybdenum(VI) complexes with glycolic, mandelic and tartaric acids. Photochemistry behaviour of the glycolate molybdenum complex", *J. Coord. Chem.*, 2007, **60,** 1933

[14] Z. Warnke, “Investigation on divalent metal complexes with oxyacids in aqueous solutions and potentiometric investigation on copper(II), zinc(II), and cadmium(II) Complexes with Glycolic Acid”, *Rocz. Chem.,* 1969, **43**, 1939.

[15] L.L.G. Justino, M.L. Ramos, M.M. Caldeira and V. M. S. Gil, “Peroxovanadium(V) complexes of glycolic acid as studied by NMR spectroscopy”, I*norg. Chim. Acta,* 2000, **311**, 119.

[16] Z. Hnatejko, S. Lis and M. Elbanowski, “Spectroscopic study of lanthanide(III) complexes with chosen aminoacids and hydroxyacids in solution”, *J. Alloys Compd.* 2000, **300**, 38.

[17] T. Toraishi, I. Farkas, Z. Szabo and I. Grenthe, “Complexation of Th(IV) and various lanthanides(III) by glycolic acid; potentiometric, ^{13}C-NMR and EXAFS studies”, *J. Chem. Soc. Dalton Trans.,* 2002, 3805.

[18] M. Kakihana, M. Tada, M. Shiro, V. Petrykin, M. Osada and Y. Nakamura, “Structure and Stability of Water Soluble $(NH_4)_8[Ti_4(C_6H_4O_7)_4(O_2)_4]\cdot 8H_2O$”, *Inorg. Chem.,* 2001,**40**, 891.

[19] M. Kakihana, K. Tomita, V. Petrykin, M. Tada, S. Sasaki and Y. Nakamura, “Chelating of titanium by lactic acid in the water-soluble diammonium Tris(2-hydroxypropionato)titanate(IV)”, *Inorg. Chem.*, 2004, **43**, 4546.

[20] K. Tomita, V. Petrykin, M. Kobayashi, M. Shiro, M. Yoshimura and M. Kakihana, “A water-soluble titanium complex for the selective synthesis of nanocrystalline brookite, rutile, and anatase by a hydrothermal method”, *Angew. Chem. Int. Ed.*, 2006, **45**, 2378.

[21] Y. Deng, Y. Jiang, Q. Hong and Z. Zhou, “Speciation of water-soluble titanium citrate: Synthesis, structural, spectroscopic properties and biological relevance”, *Polyhedron*, 2007, **26**, 1561.

[22] A. Hardy, J. D’Haen, M.K. Van Bael and J. Mullens, “An aqueous solution–gel citratoperoxo–Ti(IV) precursor: synthesis, gelation, thermo-oxidative decomposition and oxide crystallization”, *J. Sol-Gel. Sci. Technol.,* 2007, **44**, 65.

[23] E.T. Kefalas, P. Panagiotidis, C.P. Raptopoulou, A. Terzis , T. Mavromoustakos and A. Salifoglou, “Mononuclear titanium(IV)−citrate complexes from aqueous solutions: pH-specific synthesis and structural and spectroscopic studies in relevance to aqueous titanium(IV)−citrate speciation”, *Inorg. Chem*., 2005, **44**, 2596

[24] Y. Deng, H. Zhang, Q. Hong, W. Weng, H. Wan, and Z. Zhou, “Titanium-based mixed oxides from a series of titanium(IV) citrate complexes”, *Journal of Solid State Chemistry*, 2007, **180**, 3152

[25] M. Kakihana, M. Kobayashi, K. Tomita, V. Petrykin, “Application of water-soluble titanium complexes as precursors for synthesis of titanium-containing oxides via aqueous solution processes”, *Bull. Chem. Soc. Jpn*., 2010, **83**, 1285

[26] J.M. Collins, R. Uppal, C.D. Incarvito, A.M. Valentine, “Titanium(IV) citrate speciation and structure under environmentally and biologically relevant conditions”, *Inorg. Chem.* 2005, **44**, 3431

[27] N.R. Haase, S.S. Shian, K.H. Sandhage, and N. Kroger, “Biocatalytic nanoscale coatings through biomimetic layer-by-layer mineralization”, *Adv. Func. Mater.*, 2011, **21**, 4243

[28] Y. Fang, Q. Wu, M.B. Dickerson, Y. Cai, S. Shian, J. Berrigan, N. Poulsen, N. Kroger and K.H. Sandhage, “Protein-mediated layer-by-layer syntheses of freestanding microscale titania structures with biologically assembled 3-D morphologies”, *Chem. Mater.*, 2009, **21**, 5704

[29] J.D. Berrigan, T.S. Kang, Y. Cai, J. R. Deneault, M.F. Durstock and K.H. Sandhage, “Protein-enabled layer-by-layer syntheses of aligned, porous-wall, high-aspect-ratio TiO_2 nanotube arrays”, *Adv. Func. Mater.*, 2011, **21**, 1693

[30] Y. Jiang, D. Yang, L. Zhang, Q. Sun, X. Sun, J. Li and Z. Jiang, “Preparation of protamine-titania microcapsules through synergy between layer-by-layer assembly and biomimetic mineralization”, *Adv. Func. Mater.*, 2009, **19**, 150

[31] A.V. Zholnin and V.N. Podchainova, “Titanium(IV) complex-formation with Lactic Acid”, *Zhur. neorg. Khim.*, 1971, **16**, 1162.

[32] A. V. Zholnin, “Complexing of Ti(IV) with citric acid”, *Zhur. neorg. Khim.*,1971, **16**, 1010.

[33] P.S. Kalsi, Spectroscopy of Organic Compounds, *New Age International, New Delhi, India*, 2004, 244.

[34] M. Kalivac, E. Kyriakakis, C. Gabriel, C.P. Raptopoulou, A. Terzis, J.-P. Tuchagues, A. Salifoglou, “Synthesis, isolation, spectroscopic and structural characterization of a new pH complex structural variant from the aqueous vanadium(V)-peroxo-citrate ternary system”, *Inorganica Chimica Acta*, 2006, **359**, 4535 - 4548,

[35] Human Metabolome Database, http://www.hmdb.ca/spectra/nmr_one_d/1162.

[36] M.J. O’Neil, P.E. Heckelman, C.B. Koch, K.J. Roman, The Merck Index, an Encyclopedia of Chemicals, Drugs, and Biologicals – Fourteenth Edition, *Merck Co., Inc. Whitehouse Station, NJ* ,2006.

[37] Chemical Book Database, http://www.chemicalbook.com/SpectrumEN_611-71-2_1HNMR.htm.

[38] Human Metabolome Database, http://www.hmdb.ca/spectra/nmr_one_d/1141.

CHAPTER 2: LAYER-BY-LAYER FABRICATIONS OF BIO-ENABLED FUNCTIOANL METAL-OXIDE THIN-FILMS USING THE SYNTHESIZED COMPLEX PRECURSORS

2.1 SUMMARY

For the first time, several synthesized Ti-, Zr- and Hf-containing complexes were utilized in the bio-inspired, layer-by-layer fabrication of corresponding functional inorganic oxide (i.e., TiO_2, ZrO_2, HfO_2), thin films.

Si wafer templates were exposed, in alternating fashion, to aqueous protamine- and titania or zirconia or hafnia precursor-bearing solutions. Protamine, a polycationic peptide obtained from a variety of fish, possesses 31 amino acids, most of which are arginines. Protamine is able to electrostatically bind to surfaces that are negatively charged and can induce the formation of TiO-, ZrO-, HfO- precipitates upon exposure to the synthesized precursors. Subsequent pyrolysis of the protamine-derived coatings yielded thin-film coatings consisting of networks of interconnected pores and titania or zirconia or hafnia nanoparticles respectively.

The QCM-D results of the synthesized complexes indicated that the citrate precursors, (i.e., ammonium Ti(citrate), ammonium Zr(citrate), ammonium Hf(citrate)) could not be utilized as precursors in the protamine-enabled layer-by-layer deposition process, while the other five precursors (i.e., ammonium Ti(lactate), ammonium Ti(mandelate), ammonium Zr(lactate), ammonium Zr(mandelate), ammonium Hf(mandelate)) could be used as precursors in the protamine-enabled layer-by-layer deposition process. Apart from ammonium Ti(mandelate), all the other four precursors

(i.e., ammonium Ti(lactate), ammonium Zr(lactate), ammonium Zr(mandelate), ammonium Hf(mandelate)), followed the active volume deposition model, which involves a transitional point from exponential to linear growth during the deposition process. Ammonium Ti(mandelate) exhibited a linear growth during the deposition process, which conformed to an active surface model. The AFM analyses of the samples coated by these precursors coincided well with the QCM-D analyses. The ligand type and the metal element type had a significant influence on the deposition behavior of the complexes.

2.2 INTRODUCTION

Introduction to Biomineralization and peptide-enabled Layer-by-Layer deposition

Functional materials synthesized under mild conditions are of growing interest to the materials research community and may find promising applications in a range of bio- and nanotechnologies.[1-4] If we turn our eyes to nature, we can find that nature possesses an extraordinary and unique capability to assemble inorganic components into a wide range of complex micro- and nanopatterned architectures under mild conditions.[5-7] Learning from nature, we could perfect our ability to fabricate nanostructured materials for a wide variety of applications and shed light on fundamental mechanisms to elucidate some nano and microscale phenomena in biomineralization.[8-11] One of the most investigated examples is the study of the role of biomolecules, such as silicatein and silaffin, in the biosilification process.[12-14] Various chemically-synthesized analogues of silaffins, including a 19-amino-acid R5 peptide, homopolymers composed of key amino acids, long-chain polyamines, short-chain amines and even mono-amines have also been successfully employed for the rapid precipitation of nano-structured silica.[15-19] Many other peptides and proteins have also been discovered that are capable of inducing the precipitation of inorganic materials, such as CdSe, GeO_2, Fe_3O_4, Co_3O_4, Ga_2O_3, $BaTiO_3$, etc., that are useful in scientific and engineering applications.[20-25] Morse, et al.[26] found that silicatein, an enzymatic biocatalyst purified from the glassy skeletal elements of a marine sponge, is also capable of catalyzing and templating the hydrolysis, and subsequent polycondensation, of a water-stable alkoxide-like conjugate of titanium to form titanium dioxide at low temperature and pressure and of neutral pH. Sewell and Wright[27] reported that the R5 peptide, a bio-inspired analogue derived from the NatSil

protein in the diatom *Cylindrotheca fusiformis*, can form titanium dioxide in a concentration-dependent manner from the nonnatural substrate, titanium bis(ammonium lactato) dihydroxide. However, compared with silica, the biomimetic syntheses of titania nanomaterials, and the associated mechanism under ambient conditions, are still not well investigated and understood. It was reported that the electrostatic interaction between biomolecules and inorganic species may play a crucial role in biomineralization.[28–36]

Fang, et al. employing the 31-residue peptide protamine (PA), with sequence $H3N^{+}$-ARRRRSSSRPIRRRRPRRRTTRRRRAGRRRR-CO_2^{-}, as the mineralizing polyamine to enable the Layer-by-Layer (LbL) deposition of mineral oxides.[37] The process of LbL mineralization occurred by the alternating exposure of surfaces to solutions containing protamine and a precursor of silicon- or titanium-oxide (Si-O or Ti-O, respectively) in aqueous solutions at near-neutral pH. PA adsorbs to negatively-charged mineral surfaces and induces the deposition of Si-O or Ti-O upon exposure of the protamine-coated surface to the mineral precursor. This process results in a newly-formed surface with a negative charge for Si-O and Ti-O coatings, allowing for the adsorption of more protamine and subsequent mineral oxide deposition. A graphic representation of LbL mineralization is given in Scheme 1.1.[37] The significance of the electrostatic interaction of protamine and the mineral oxide surface was made evident by Fang and co-workers, who showed a decrease in titania deposition when LbL was attempted in solutions that were sufficiently acidic or contained high NaCl concentrations.[38] An acidic solution reduced the presence of negative charges on the mineral oxide surface, while high salt concentrations screened the negative charges via Na^{+} Ions.

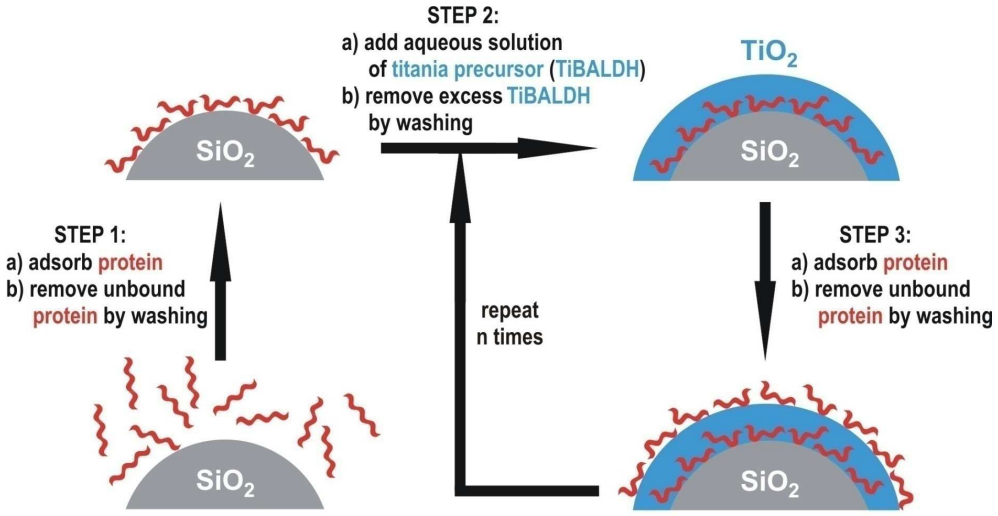

Figure 2.1: The Protamine-induced Layer-by-layer (LBL) deposition of Ti-O, Si-O coatings.[37]

LbL mineralization has been also performed to coat Ti-O or Si-O on $CaCO_3$ spheres that contain entrapped enzymes.[39-44] After the deposition of multiple mineral oxide layers, the $CaCO_3$ was dissolved and the protamine/mineral oxide coatings became free-standing, resulting in an enzyme-containing solution encased by the mineral oxide shell. LbL mineralization has also been utilized by Berrigan, et al. to deposit conformal Ti-O coatings on porous anodic alumina membranes. These coatings were subjected to a thermal treatment to remove organic material, leaving behind a semi-conductive TiO_2 coating. Subsequent dissolution of the alumina template yielded aligned TiO_2 nanotube arrays that were then utilized in a photovoltaic cell.[45]

As the present work will demonstrate, other acidic oxide (pI < 7) besides SiO_2 or TiO_2, such as ZrO_2 and HfO_2, can also be synthesized in a protamine-enabled layer-by-layer fashion.

2.3 EXPERIMENTAL PROCEDURES

The methods used to generate and characterize the TiO_2, ZrO_2 and HfO_2 thin films, using the synthesized Ti-, Zr-, and Hf-containing precursors discussed in Chapter 1 are discussed in this section.

The chemicals discussed in the Experiment Section are as below: deionized (DI) water (18.2 MΩ·cm), protamine sulfate (Grade X, Sigma-Aldrich, St. Louis, MO), pH 8 Tris-HCl buffer (Alfa Aesar, Ward Hill, MA), 98% w/w H_2SO_4 (Alfa Aesar, Ward Hill, MA), and 98% w/w H_2O_2 (Alfa Aesar, Ward Hill, MA).

2.3.1 Quartz Crystal Microbalance Characterization of Synthesized TiO-, ZrO-, and HfO-bearing coatings

The potential for utilizing the synthesized Ti-, Zr-, Hf- complexes as precursors for protamine-enabled layer-by-layer deposition was investigated with a quartz crystal microbalance with simultaneous dissipation monitoring (QCM-D, Q-sense E1 system, Biolin Scientific, Inc., Vastra Frolunda, Sweden). Standard gold-coated quartz sensors were coated with a thin layer (~50 nm) of SiO_2 (Model QSX303, Biolin Scientific, Inc., Vastra Frolunda, Sweden). The 1^{st}, 3^{rd}, 5^{th}, 7^{th}, 9^{th}, 11^{th} , and 13^{th} harmonics were measured simultaneously during all QCM-D experiments. The 5^{th} harmonic was selected for analysis because smaller harmonics (1^{st} and 3^{rd}) sensed larger areas that were affected by the O-ring used to hold the sensor, and analyses with higher harmonics (11^{th} and 13^{th}) became less sensitive with thicker coatings.

All sensors were cleaned by a 10 min. UV-ozone treatment (UV/Ozone ProCleaner, Bioforce Nanoscience, Inc., Ames, IA, USA) followed by incubation for 30 min. in a 2% v/v sodium dodecyl sulfate (SDS, 99+% purity, Amresco, Solon, OH, USA)

solution. The sensors were rinsed thoroughly with water, dried under nitrogen flow for 10 min, and then cleaned by UV-ozone treatment for 10 min. QCM-D was used to examine ten deposition cycles at a solution flow rate of 0.1 mL/min and 22 ℃.

For protamine-mediated deposition of TiO-, ZrO-, and HfO-bearing films, a single cycle consisted of four steps: (1) exposure to protamine sulfate (100 ug/ml in pH 8 100 mM Tris-HCl buffer) for 10 min., (2) exposure to a buffer (pH 8 100 mM Tris-HCl) rinse for 5 min.; (3) exposure to a precursor solution (~5 mM in pH 8 100 mM Tris-HCl buffer) for various times, t, according to the number of cycles; and (4) exposure to a buffer (pH 8 100 mM Tris-HCl) rinse for 5 min. The precursor solution exposure time varied for each cycle due to changes in reaction kinetics, and precursor solutions flow continued until the resonance frequency change plateaued (i.e., ΔF varied by less than 1 Hz per min.), which indicated that the reaction of those precursors with the deposited protamine was essentially completed.

QCM analyses of the protamine-enabled deposition of films using TiBALDH from Sigma (serving as a control), ammonium Ti(lactate), ammonium Ti(citrate), ammonium Ti(mandelate), ammonium Zr(lactate), ammonium Zr(citrate), ammonium Zr(mandelate), ammonium Hf(citrate), and ammonium Hf(mandelate) complexes have been completed.

2.3.2 Fabrication of LbL Protamine-Enabled TiO_2, ZrO_2 and HfO_2 Thin-Film Coatings on Silicon Wafer Substrates

The QCM result analyses indicated that, none of the citrates yielded layer-by-layer coatings by protamine. Thus, ammonium Ti(lactate), ammonium Ti(mandelate), ammonium Zr(lactate), ammonium Zr(mandelate), ammonium Hf(mandelate) were

chosen as precursors for the protamine-enabled deposition of thin film coatings on silicon wafer substrates.

(1) Fabrication of TiO_2 Thin Films on Silica Wafer Substrates Using Ammonium Ti(lactate) and Ammonium Ti(mandelate) Precursor Solutions

TiO-bearing films were deposited onto silicon wafer substrates (Wafernet, Inc., San Jose, CA, USA) that were incubated in a piranha solution (9 M H_2SO_4 and 3 M H_2O_2) for 30 min. at room temperature. After rinsing with a large amount of water, the wafers were rinsed in ethanol, and then dried with nitrogen at room temperature for 5 min. The wafers were then cleaned by rinsing in ethanol, followed by water, and dried with flowing nitrogen at room temperature for 5 min. The wafers were then cut into 2 cm by 2 cm pieces for coating.

Prior to deposition, the Si substrates were incubated in a 100 mM pH 8 buffer solution for at least 15 min to allow the surface to reach equilibrium. For each cycle, the coating procedure was as follows: The silica wafers were first incubated in a 1 mg/mL protamine sulfate solution in the 100mM pH 8 Tris-HCl buffer for 10 min to allow for protamine binding to the silica surface. The protamine-treated substrates were rinsed three times with the Tris-HCl buffer, and then incubated in a 4.82 ± 0.04 mM ammonium titanium lactate complex solution (diluted directly from the original synthesized precursor solution) for *t* minutes, where *t* was based upon the time required for saturation according to QCM-D measurements, which was as shown in **Table 2.1**. The Si wafer was then rinsed three times in buffer to remove excess ammonium titanium lactate.

By repeating this deposition cycle *n-1* times, *n* number of layers were deposited. For the TiO-bearing coating, the deposition process was repeated for 1, 3, 5, 7, and 9

times, which resulted in TiO-bearing Si substrates with coatings generated with a total of 2, 4, 6, 8, 10 cycles respectively. For each coating session, there were 2 Si wafers that underwent the same procedure. After the coating process was finished, one specimen was rinsed with DI water and dried with flowing nitrogen at room temperature for 5 min, while the other was heated in a tube furnace (Lindberg / Blue M, NC USA) at a ramp rate of 1.5 °C/min to 500°C (AutoFire® Controller, Orton Ceramic Foundation, OH, USA outfitted with a k-type thermocouple, OMEGA Engineering, Inc., CT, USA) followed by holding at 500°C for 4 hrs in air to allow for organic pyrolysis of the protamine.

When using the commercial TiBALDH solution from Sigma, the coating procedure was exactly the same as above.

When using the ammonium Ti(mandelate) precursor, the coating procedure was exactly the same as above except for substitution of the 4.82 ± 0.04 mM ammonium Ti(lactate) solution with a 4.51 ± 0.05 nM ammonium Ti(mandelate) precursor solution.

After the coating and firing processes, 10 Si wafer substrates exposed to 2, 4, 6, 8, 10 coating cycles, were characterized before & after firing by multiple analytical methods (SEM, TEM, XRD, and AFM analyses).

Table 2.1. Precursor incubation times for protamine-enabled deposition using TiBALDH from Sigma, synthesized TiBALDH, or ammonium Ti(mandelate) precursor.

Time (min) \ Cycles	1, 2	3, 4	5, 6	7, 8	9, 10
TiBALDH from Sigam	5	10	15	20	30
Synthesized TiBADLH	5	10	15	20	30
Ammonium Ti(mandelate)	5	10	10	15	15

(2) Fabrication of ZrO_2 Thin-films on Silica Wafer Substrates Using Ammonium Zr(lactate) and Ammonium Zr(mandelate) Precursor Solutions

The coating procedure was exactly the same as for the ammonium Ti(lactate) complex, except for substitution of the 4.82 ± 0.04 mM ammonium Ti(lactate) precursor solution with a 4.61 ± 0.03 mM ammonium Zr(lactate) precursor solution or a 4.42 ± 0.05 mM ammonium Zr(mandelate) precursor solution. The firing condition for these coated samples consisted of a ramp rate of 1.5 °C/min to 600℃, followed by holding at 600℃ for 6 hrs in air.

After the coating and firing processes, 16 Si wafer substrates exposed to 2, 4, 6, 8, 10, 12, 14, or 16 coating cycles, were characterized before & after firing by multiple analytical methods (SEM, TEM, XRD, and AFM analyses).

(3) Fabrication of HfO_2 Thin-films on Silica Wafer Substrates Using an Ammonium Hf(mandelate) Precursor Solution

The coating procedure was exactly the same as for the coating process of the ammonium Ti(lactate) complex, except for substitution of the 4.82 ± 0.04 mM ammonium Ti(lactate) precursor solution with a 4.32 ± 0.03 mM ammonium Hf(mandelate) solution. The firing condition for these coated samples consisted of a ramp rate of 1.5 °C/min to 600℃, followed by holding at 600℃ for 6 hrs in air.

After the coating and firing processes, 16 Si wafer substrates exposed to 2, 4, 6, 8, 10, 12, 14, 16 coating cycles, were characterized before & after firing by multiple analytical methods (SEM, TEM, XRD, AFM).

The incubation time for protamine-enabled LbL deposition using ammonium Zr(lactate), ammonium Zr(mandelate) or ammonium Hf(mandelate) precursors was as shown below in **Table 2.2**.

Table 2.2. Precursor incubation times for protamine-enabled deposition using ammonium Zr(lactate), ammonium Zr(mandelate) and ammonium Hf(mandelate) precursors.

Time (min) \ Cycles	1, 2	3, 4	5, 6	7, 8	9, 10	11, 12	13, 14	15, 16
Ammonium Zr(lactate)	5	10	10	15	15	20	20	30
Ammonium Zr(mandelate)	5	10	10	15	15	20	20	30
Ammonium Hf(mandelate)	5	10	10	15	15	20	20	30

2.3.3 Characterization of LBL Protamine-Enabled TiO_2, ZrO_2, and HfO_2 Thin Film Coatings on Si Wafer Substrates

(1) Atomic Force Microscopy Characterization

Atomic force microscopy (AFM, Digital Instruments Nanoscope@ III, Tonawanda, NY, USA) was conducted on protamine-derived films on silicon wafers after *n* number of deposition cycles (where *n* varied for different precursors) before and after firing in air. The measurements were conducted in tapping mode using 10 nm radius of curvature general purpose probes (Mikromasch AFM NSC36, Mikromasch USA, San Jose, CA, USA) with a spring constant of 0.6 N/m and a resonant frequency of 75 Hz. After deposition was completed, a razor was used to make several cuts through the coating. Thickness measurements were then conducted across the coated/uncoated boundary with

a scan area of 10 μm by 20 μm defined with Nanoscope Analysis software V1.4r1 (Veeco Instruments, Plainview, NY, USA).

Topographical images of the coated area on as-coated and heat treated films were obtained over a 15 μm by 15 μm area. The images were plane-leveled and the root-mean square roughness of the films was measured using Nanoscope Analysis software over five different 5 μm by 5 μm areas.

AFM thickness measurements were conducted on the following samples: i) protamine-enabled films before firing using TiBALDH from Sigma, synthesized TiBALDH (i.e., ammonium Ti(lactate)), ammonium Ti(mandelate), ammonium Zr(lactate), ammonium Zr(mandelate), or ammonium Hf(mandelate) precursors; and ii) some of these protamine-enabled films after firing (for films using synthesized TiBALDH (i.e., ammonium Ti(lactate), ammonium Ti(mandelate), and ammonium Zr(mandelate) precursor).

(2) X-ray Diffraction Analyses of the TiO_2, ZrO_2, HfO_2 Thin Films

X-ray diffraction (XRD) analyses were conducted with Cu Kα radiation using an X-Pert Pro Alpha 1 diffractometer equipped with an incident beam Johannsen monochromator and an X' Celerator linear detector (PANalytical, Almelo, The Netherlands). For titanium dioxide, zirconium dioxide, and hafnium dioxide, the samples were scanned from 20 to 60 2θ with a step size of 0.02 and a preset time of 25 s. All peaks were identified according to the JCPDS file. The samples characterized by XRD analyses were: 6-cycles-coated Si wafer substates after firing using ammonium Ti(lactate), ammonium Ti(mandelate), ammonium Zr(lactate), ammonium Zr(mandelate), ammonium Hf(mandelate) precursor solutions.

(3) SEM & TEM Characterization of the TiO_2, ZrO_2, and HfO_2 Thin Films

Scanning electron microscopy was conducted with a field emission scanning electron microscope (Leo 1530 FEG SEM, Carl Zeiss SMT Ltd., Cambridge, UK) equipped with an energy dispersive X-ray spectrometer (INCA EDS, Oxford Instruments, Bucks, UK).

A focused ion beam (FIB) instrument (Model Nova Nanolab 200, FEI, Oregon, USA) was used to generate cross sections of the films. Ion milled thin foil cross sections of the films were characterized with a transmission electron microscope (Model JEM 4000EX, JEOL, Tokyo, Japan) operated at 400 kV.

The samples characterized by SEM and TEM were: 6-cycles-coated Si wafer substates after firing using ammonium Ti(lactate), ammonium Ti(mandelate), ammonium Zr(lactate), ammonium Zr(mandelate), or ammonium Hf(mandelate) precursor solutions (the same samples as for the XRD analyses).

2.4 RESULTS AND DISCUSSION

2.4.1 Quartz Crystal Microbalance Characterization of Synthesized TiO-, ZrO-, and HfO-bearing Coatings

The reaction kinetics of the protamine-enabled layer-by-layer deposition of the Ti-, Zr-, Hf-containing complexes during each stage of the deposition process were examined using QCM-D analyses. For the three Ti-containing precursors (i.e., ammonium Ti(lactate), ammonium Ti(citrate), ammonium Ti(mandelate)), there were a total of ten depositions completed on a SiO_2-coated sensor at pH 8.0, a flow rate of 100 μL min^{-1} and 22℃. For the ammonium Zr(lactate), ammonium Zr(citrate), ammonium Zr(mandelate), ammonium Hf(citrate), and ammonium Hf(mandelate) precursors, the total number of deposition cycles went up to 16. To be consistent with the former work of J. D. Berrigan[46] on protamine-enabled deposition of TiO-bearing coatings using commercial TiBALDH from Sigma, the 5^{th} harmonic was selected for QCM-D analyses. .

(1) Comparison of deposition behavior of Synthesized Ammonium Ti(lactate), Ammonium Ti(citrate), or Ammonium Ti(mandelate) precursors vs. TiBALDH from Sigma*

* For simplicity, synthesized TiBALDH was used to refer to the synthesized ammonium Ti(lactate) complex.

The frequency changes (ΔF) of the 5th harmonic of the quartz crystal, during the deposition using synthesized TiBALDH, ammonium Ti(citrate), ammonium Ti(mandelate), or TiBALDH from Sigma, are shown in **Figure 2.2**.

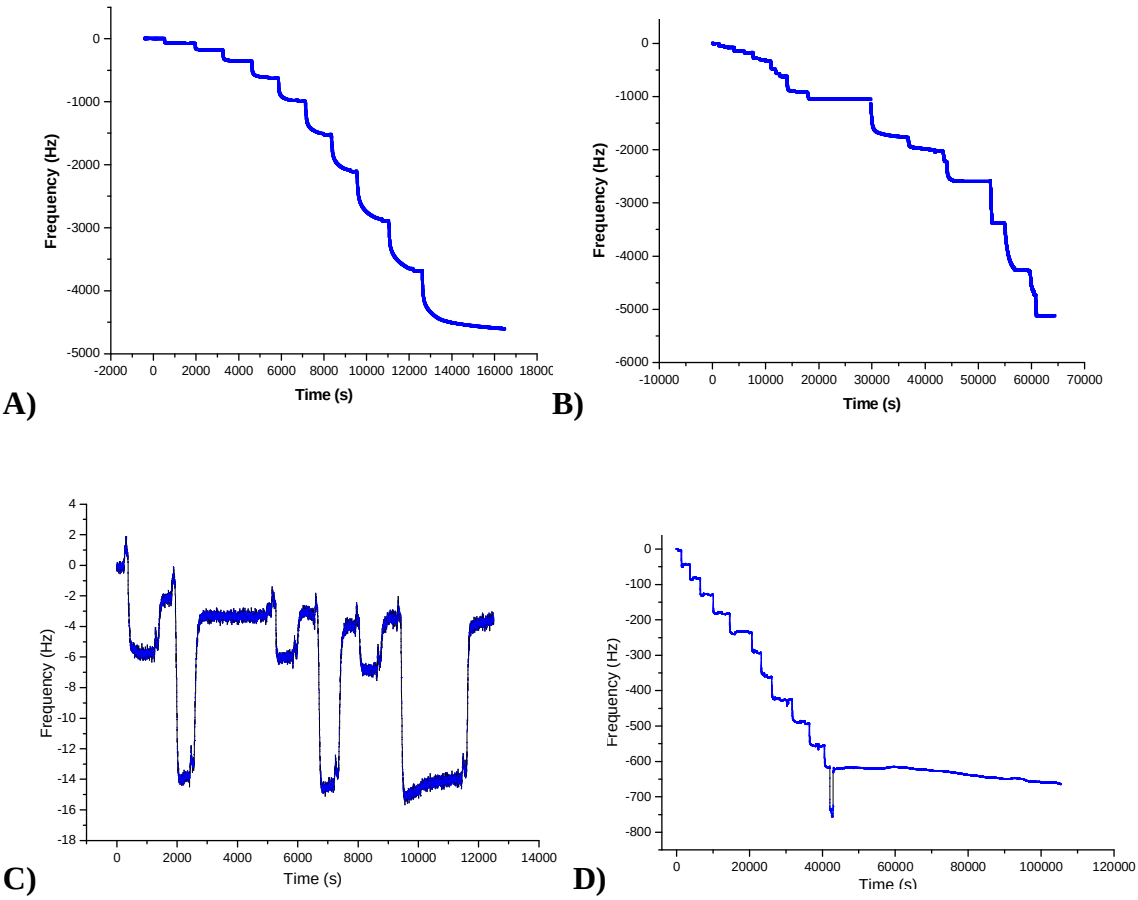

Figure 2.2: Quartz crystal microbalance data showing the frequency change during layer-by-layer, protamine-enabled deposition using the following precursors over 10 cycles: a) TiBALDH from Sigma, b) synthesized TiBALDH (ammonium Ti(lactate) complex), c) ammonium Ti(citrate) complex, d) ammonium Ti(mandelate) complex.

From **Fig. 2.2** it can be seen that for the ammonium Ti(citrate) complex, a very small decrease in frequency (~ 10 Hz) occurred when running the precursor salt solution, which meant that the amount of material deposited was quite low. Furthermore, when running buffer through the sensor afterwards, the frequency returned to the original

plateau, which indicated that the deposit had been largely washed off from the surface of the sensor. This phenomenon repeated for 3 cycles, which indicated that this ammonium Ti(citrate) complex was not effective as a precursor for the protamine-enabled layer-by-layer coating method. As the QCM-D plots indicated, all of the other complexes (i.e., TiBALDH from Sigma, synthesized TiBALDH (ammonium Ti(lactate)), ammonium Ti(mandelate)), did act as effective precursors for the layer-by-layer deposition by protamine.

The evolution of $-\Delta F$, from QCM-D analyses of the above 3 precursors, versus the number of deposition cycles, is presented in **Fig. 2.3**. While the Sauerbrey model is typically used to model thickness values from QCM data, the use of this model is limited to rigid films exhibiting a change in dissipation (ΔD) of less than 1.[47] After 3 deposition cycles, ΔD was much larger than 1 per 10 Hz and the measured harmonics all became divergent for all of the films. Therefore, the Sauerbrey relation between ΔF and adsorbed mass could not be used to accurately relate ΔF to film thickness, and the QCM-D data analysis was limited to analyses of trends in ΔF.

From **Figure 2.3**, it can be seen that the synthesized TiBALDH and ammonium Ti(mandelate) complex can both be successfully utilized in the protamine-enabled layer-by-layer coating process on the SiO_2 sensor. The TiBALDH from Sigma and synthesized TiBALDH both exhibited an exponential fit over cycles 1-6, and transitioned to a linear regime afterwards. For each cycle, the two precursors yielded similar deposition rates, though the ΔF values for synthesized TiBALDH were slightly higher than that of TiBALDH from Sigma. The ΔF values for the ammonium Ti(mandelate) complex

exhibited a linear fit from cycles 1 to 10, with much less deposition for each cycle compared to TiBALDH from Sigma and synthesized TiBALDH.

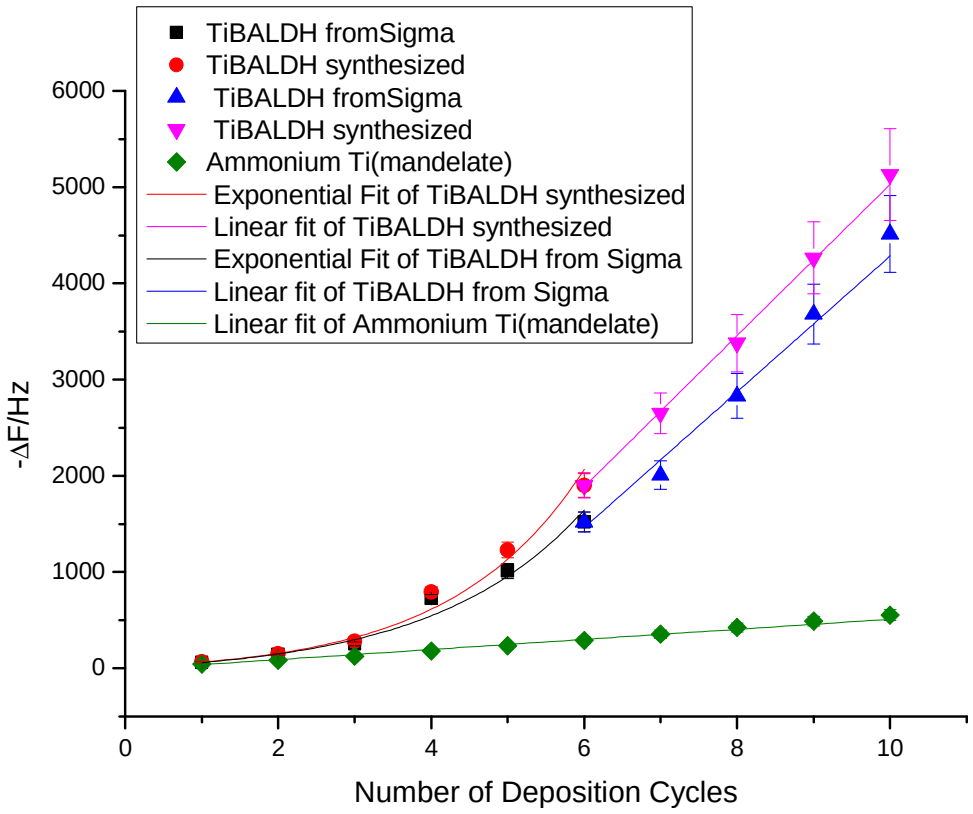

Figure 2.3: The *ΔF* evaluated using the 5th harmonic from QCM-D measurement of protamine-enabled deposition using TiBALDH from Sigma, synthesized TiBALDH, or ammonium Ti(mandelate) precursor solutions over 10 cycles. Error bars represent the standard deviation recorded from two experiments. Cycles 1 to 6 of the protamine-enabled TiBALDH and synthesized TiBALDH films were fit using an exponential equation while cycles 6 to 10 were fit with a linear regression to determine the wet film growth rate. For the ammonium Ti(mandelate) complex, cycles 1 to 10 were fit with a linear equation.

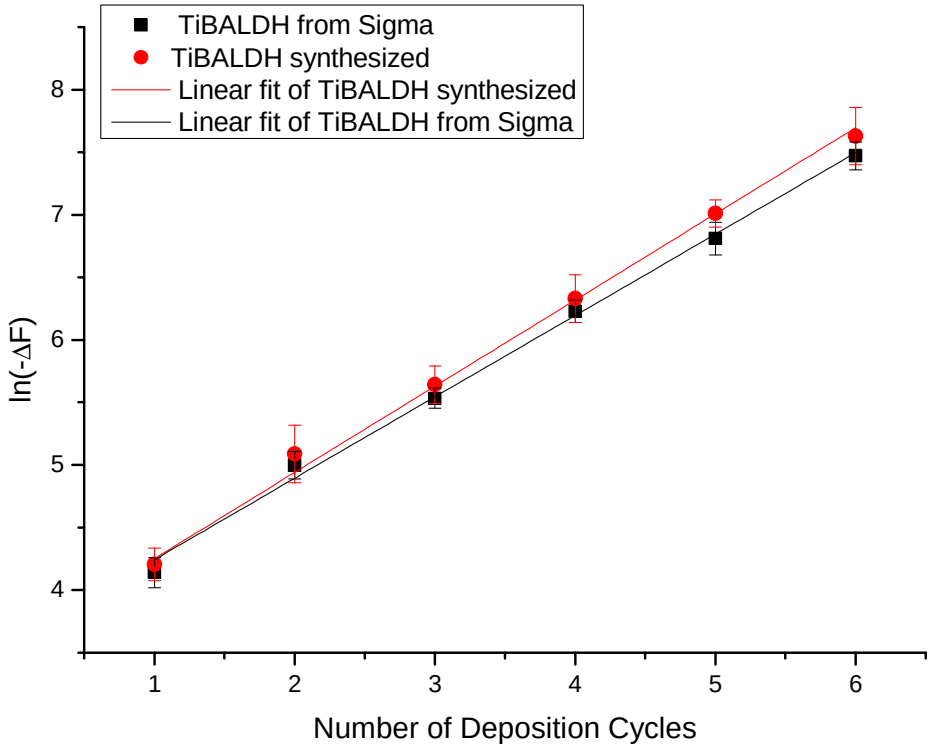

Figure 2.4: The linear dependence of ln(-*ΔF*) with *n* for films prepared using TiBALDH from Sigma or synthesized TiBALDH for deposition cycles 1 to 6.

For the synthesized TiBALDH, **Equation 2.1** was used to fit the behavior during the first 6 deposition cycles with an R^2 = 0.9856. For the TiBALDH from Sigma, **Equation 2.2** was used to fit the behavior during 1 to 6 deposition cycles with an R^2 = 0.9867. For the ammonium Ti(mandelate) complex, **Equation 1.3** was used to fit the behavior during 1 to 10 deposition cycles with an R^2= 0.9893.

$$\Delta F = -53+66^{(0.58*n)} \qquad (2.1)$$

$$\Delta F = -348+266e^{(0.33*n)} \qquad (2.2)$$

$$\Delta F = -14+52.2*n \qquad (2.3)$$

A linear dependence of ln(-ΔF), for the first six cycles with n was observed for synthesized TiBALDH and TiBALDH from Sigma (**Figure 2.4**). The linear fit of synthesized TiBALDH over cycles 1 to 6 yielded a reasonable fit (R^2=0.9962) to **Equation 2.4**. For TiBALDH from Sigma over cycles 1 to 6, a fit with R^2= 0.9959, was obtained for **Equation 2.5.**

$$\ln(-\Delta F) = 3.63 + 0.67*n \qquad (2.4)$$

$$\ln(-\Delta F) = 3.58 + 0.65*n \qquad (2.5)$$

From the plot in **Figure 2.3**, it was apparent that the exponential equation failed to fit well data points for TiBALDH from Sigma and synthesized TiBALDH beyond the sixth deposition cycle. After the sixth deposition cycle, the ΔF of TiBALDH from Sigma increased at a linear rate of 765 ± 47 Hz per cycle (R^2=0.9887), and the ΔF of synthesized TiBALDH increased at a linear rate of 807 ± 53 Hz per cycle (R^2=0.99749), which suggested that an exponential-to-linear transition occurred at the sixth deposition cycle.

Prior work conducted by J. D. Berrigan in our lab demonstrated that the protamine-enabled TiO-bearing films using TiBALDH from Sigma follow an active volume mechanism.[46] For a LBL deposition process that conforms to an active volume mechanism, the exponential deposition would only be maintained for a limited number of deposition steps before transitioning to a linear deposition regime. The synthesized TiBALDH proved to behave similarly as TiBALDH from Sigma in the protamine-enabled layer-by-layer deposition process, which both fall into the active volume mechanism category. However, the ammonium Ti(mandelate) complex behaved differently from the TiBALDH from Sigma and synthesized TiBALDH, as it obeyed a linear growth from cycle 1 to cycle 10. This result indicated that the ligand type of the

precursor had a significant effect on the deposition mechanism of the protamine-enabled process.

One possible reason for the difference in deposition behavior of ammonium Ti(mandelate) and ammonium Ti(lactate) is that, the deposit generated by protamine-enabled ammonium Ti(mandelate) coating was more compact than that for the ammonium Ti(lactate) coating. Thus, the protamine molecules inside the deposit were not able to diffuse out in the following step of deposition, such protamine migration is required for exponential growth behavior.[46] The *ΔD* (dissipation change) vs. *n* (number of deposition cycles) plots for protamine-enabled LbL deposition of ammonium Ti(mandelate) and ammonium Ti(lactate) shown below in Fig. 2.5 were consistent with more compact/rigid oxide films for the ammonium Ti(mandelate) precursor.

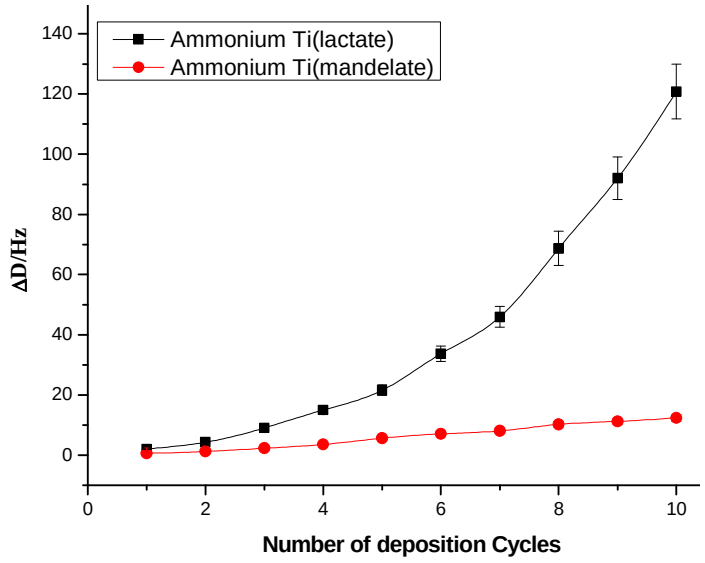

Figure 2.5: Plot of *ΔD vs. n* using the 5th harmonic from QCM-D measurement of protamine-enabled deposition using synthesized TiBALDH (i.e., ammonium Ti(lactate)), or ammonium Ti(mandelate) precursor solutions over 10 cycles. Error bars represent the standard deviation recorded from two experiments.

It can be seen from **Fig. 2.5** that, for each deposition cycle, the dissipation change for films generated by protamine-enabled deposition using ammonium Ti(lactate) was much larger than that for ammonium Ti(mandelate), which suggested that films generated using ammonium Ti(mandelate) possessed lower viscoelasticity and thus was more rigid/compact than the films generated using ammonium Ti(lactate). In this case, the protamine molecules encapsuled in the films generated by ammonium Ti(mandelate) were apparently not able to diffuse "out" of the film to react at the film/solution interface.[46] Thus, for the protamine-enabled LbL deposition using ammonium Ti(mandelate), it follows an active surface model, instead of the active volume model was obeyed.

(2) Comparison of the deposition behavior of ammonium Zr(lactate), ammonium Zr(mandelate), and ammonium Hf(mandelate) precursors

The frequency change (ΔF) of the 5th harmonic of the quartz crystal during the deposition process over 10 cycles with ammonium Zr(citrate), ammonium Zr(lactate), ammonium Zr(mandelate), ammonium Hf(mandelate) or ammonium Hf(citrate) precursors were shown in **Fig. 2.6.** The evolution of $-\Delta F$ from QCM-D analyses using the above three precursors (i.e., ammonium Zr(lactate), ammonium Zr(mandelate) and ammonium Hf(mandelate)) versus the number of deposition cycles is presented in **Figs. 2.7 - 2.10**. .

From **Fig. 2.6,** it can be seen that ammonium Zr(citrate) and ammonium Hf(citrate) exhibited similar deposition behavior as for ammonium Ti(citrate) in the previous section, in which the deposit generated with a given precursor solution has been

largely washed off from the surface of the sensor during subsequent exposure to the buffer solution. The underlying mechanism explaining why ammonium Zr(citrate), ammonium Hf(citrate), and ammonium Ti(citrate), are ineffective precursors as for the protamine-enabled, layer-by-layer coating method is not precisely known. A possible reason for this big difference between the citrates and the other complexes (i.e., the lactates and mandelates), could be that the citrate has a stronger complexation with the metal ion,[47,48] which makes it harder for protamine to strip the ligand off the precursor to form TiO-, ZrO- and HfO-bearing coatings.

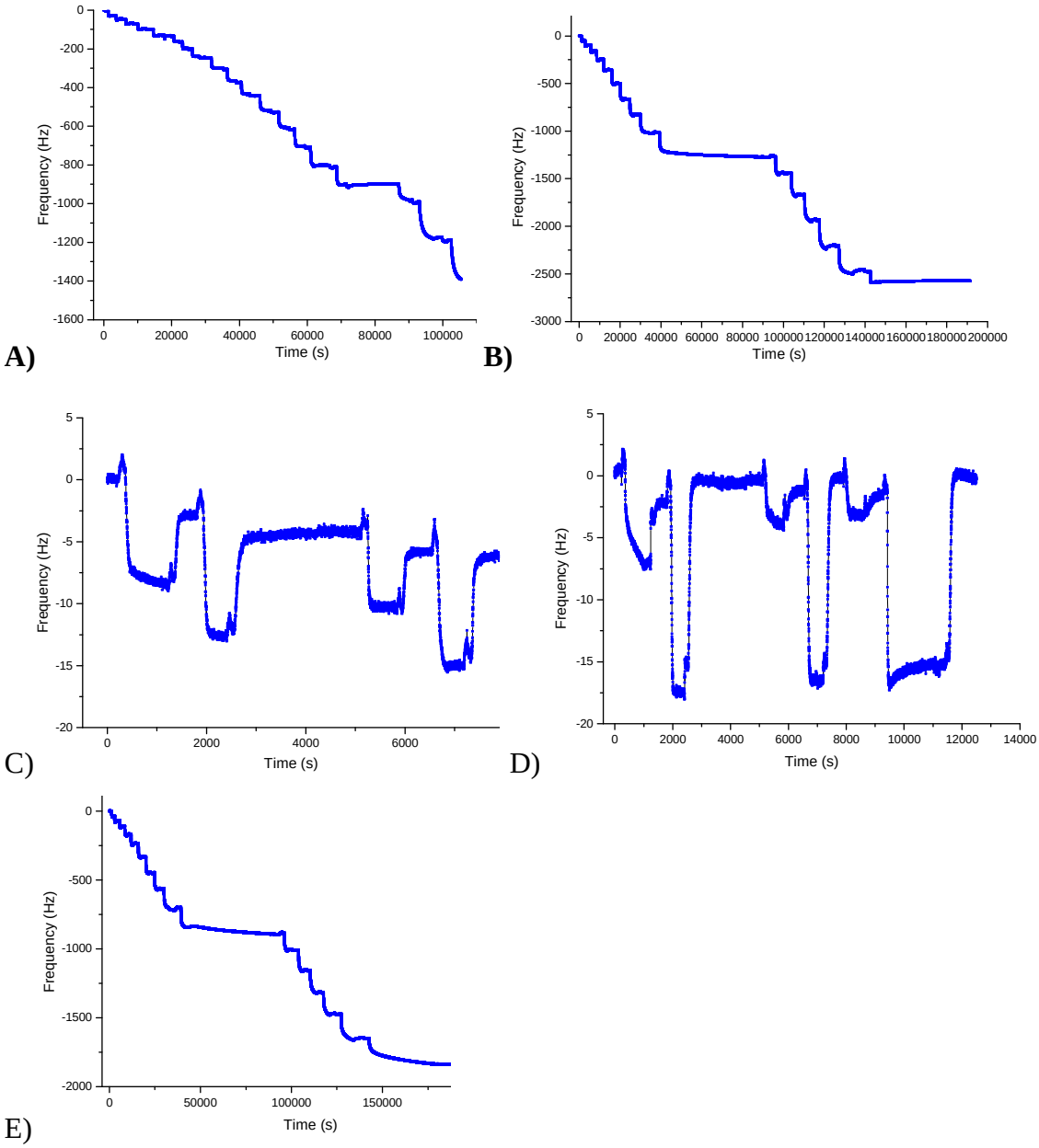

Figure 2.6: Quartz crystal microbalance data showing the frequency change during layer-by-layer, protamine-enabled deposition of the following precursors over 16 cycles: a) ammonium Zr(lactate) complex, b) ammonium Zr(mandelate) complex, c) ammonium Zr(citrate) complex, d) ammonium Hf(citrate) complex, e) ammonium Hf(mandelate) complex.

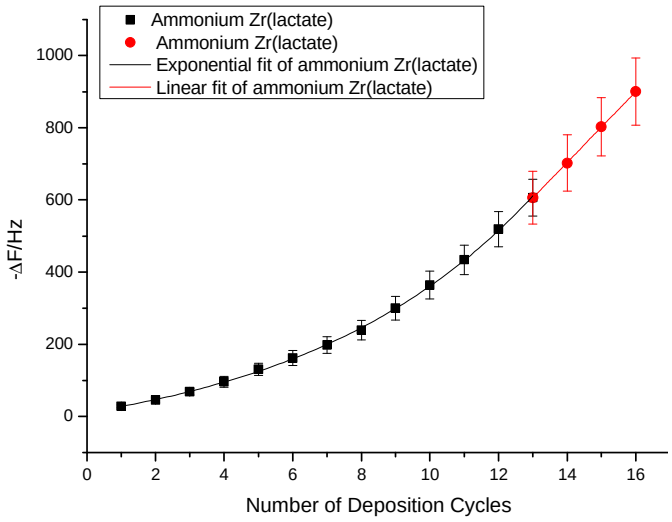

Figure 2.7: The *ΔF* evaluated using the 5th harmonic from QCM-D analyses of protamine-enabled deposition using an ammonium Zr(lactate) complex over 16 cycles. Error bars represent the standard deviation recorded from two experiments. Cycles 1 to 13 of the protamine-enabled, ammonium Zr(lactate) synthesized film were fit using an exponential equation while cycles 13 to 16 were fit with a linear regression.

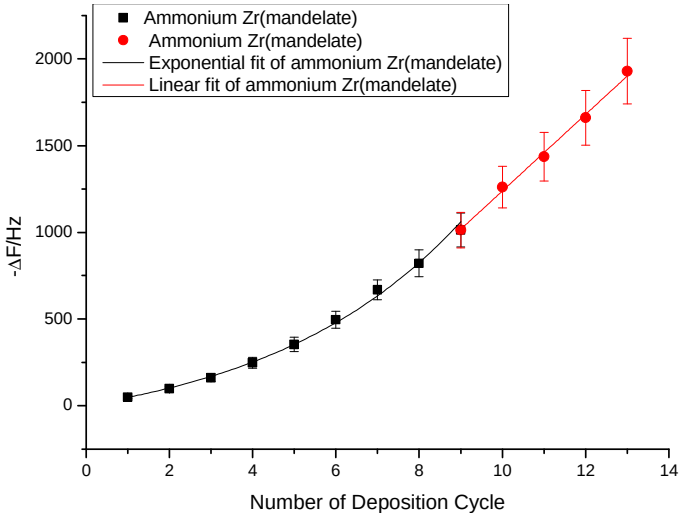

Figure 2.8: The *ΔF* evaluated using the 5th harmonic from QCM-D analyses of protamine-enabled deposition using an ammonium Zr(mandelate) complex over 13 cycles. Error bars represent the standard deviation recorded from two experiments. Cycles 1 to 9 of the protamine-enabled ammonium Zr(lactate) synthesized film were fit using an exponential equation while cycles 9 to 13 were fit with a linear regression.

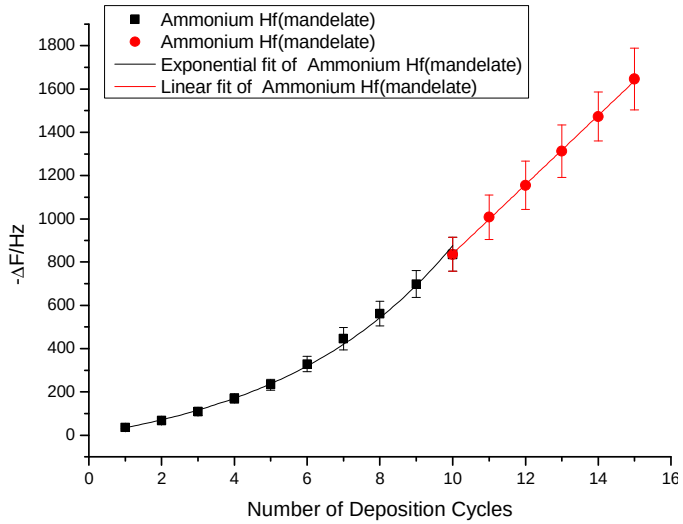

Figure 2.9: The *ΔF* evaluated using the 5th harmonic from QCM-D analyses of protamine-enabled deposition using an ammonium Hf(mandelate) complex over 15 cycles. Error bars represent the standard deviation recorded from two experiments. Cycles 1 to 10 of the protamine-enabled ammonium Zr(lactate) synthesized film were fit using an exponential equation while cycles 9 to 13 were fit with a linear regression.

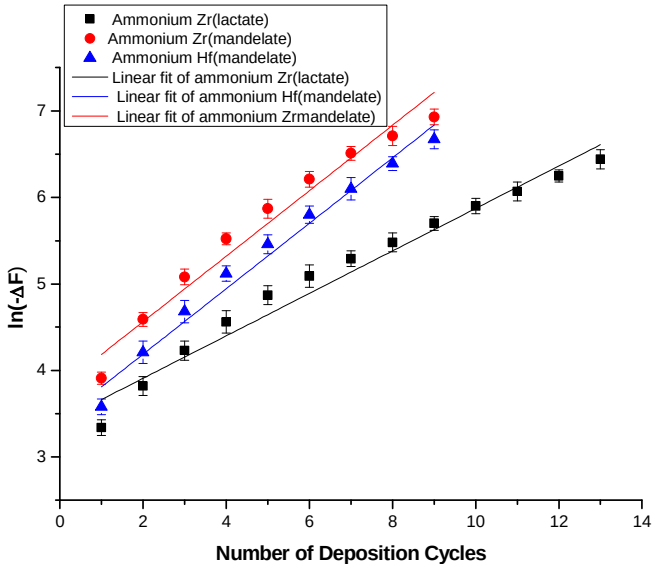

Figure 2.10: The linear dependence of ln(-*ΔF*) with *n* of ammonium Zr(lactate) from cycles 1 to 13, ammonium Zr(mandelate), or ammonium Hf(mandelate) complex from cycles 1 to 9.

From **Fig. 2.7** to **Fig. 2.9**, it can be seen that the ammonium Zr(lactate), ammonium Zr(mandelate), and ammonium Hf(mandelate) complexes could all be successfully utilized in the protamine-enabled, layer-by-layer coating process on the SiO_2 sensor. Deposition with each of these precursors followed exponential behavior at first, and transitioned to a linear regime, which was consistent with an active volume mechanism (as for TiBALDH from Sigma and synthesized TiBALDH (i.e., ammonium Ti(lactate)).

For ammonium Zr(lactate), **Equation 2.6** was used to fit the behavior during the first 13 deposition cycles with an $R^2 = 0.9994$. For ammonium Zr(mandelate), **Equation 2.7** was used to fit the behavior during 1 to 9 deposition cycles with an $R^2 = 0.99705$. For ammonium Hf(mandelate) complex, **Equation 2.8** was used to fit the behavior during 1 to 9 deposition cycles with an $R^2 = 0.99718$.

$$\Delta F = 95.5+106\exp^{(0.145*n)} \qquad (2.6)$$

$$\Delta F = -184+188\exp^{(0.21*n)} \qquad (2.7)$$

$$\Delta F = -130+134\exp^{(0.20*n)} \qquad (2.8)$$

The linear dependence of $\ln(-\Delta F)$ for the first 13 cycles with n using ammonium Zr(lactate), and of $\ln(-\Delta F)$ for 1 to 9 cycles with n using ammonium Zr(mandelate) and ammonium Hf(mandelate) complexes, verified the exponential nature of the deposition process (**Figure 2.9**). The linear fit for deposition with ammonium Zr(lactate) for cycles 1 to 13 yielded a reasonable value of $R^2=0.97127$, as shown in **Equation 2.9**. For deposition using ammonium Zr(mandelate), the behavior for cycles 1 to 9 yielded a fit

with R^2= 0.97797, as shown in **Equation 2.10**. For ammonium Hf(mandelate) complex, the behavior for cycles 1 to 9 yielded a fit with R^2 = 0.96207, as shown in **Equation 2.11.**

$$\ln(-\Delta F) = 3.417 + 0.245*n \quad (2.9)$$

$$\ln(-\Delta F)=3.433+0.378*n \quad (2.10)$$

$$\ln(-\Delta F)=3.806+0.381*n \quad (2.11)$$

From the data in **Figs. 2.7** and **2.8**, and in **Fig. 2.9**, it was apparent that the exponential equation failed to fit data points beyond the 13th and 9th deposition cycles, respectively. After the 13th deposition cycle, the -ΔF of ammonium Zr(lactate) increased at a linear rate of 98 ± 11 Hz per cycle (R^2=0.9913). After the 9th deposition cycle, the -ΔF of ammonium Zr(mandelate) increased at a linear rate of 220 ± 16 Hz per cycle (R^2=0.9967), and the -ΔF of ammonium Hf(mandelate) increased at a linear rate of 160 ± 15 Hz per cycle (R^2=0.9994); that is, an exponential-to-linear transition occurred at the 13th cycle for deposition with ammonium Zr(lactate) and at the 9th cycle for deposition with ammonium Zr(mandelate) and ammonium Hf(mandelate).

2.4.2 SEM & TEM Characterization of the TiO_2, ZrO_2, HfO_2 Thin Film

(1) SEM analyses of Si substrates coated using ammonium Ti(lactate), ammonium Ti(mandelate), ammonium Zr(lactate), ammonium Zr(mandelate), and ammonium Hf(mandelate) complexes

Si wafer substrates coated with 6 deposition cycles using ammonium Ti(lactate), ammonium Ti(mandelate), ammonium Zr(lactate), ammonium Zr(mandelate), and ammonium Hf(mandelate) were examined after firing by SEM.

It can be seen from **Fig. 2.12 - Fig. 2.16** that, by comparing these SEM images with **Fig. 2.11**, a SEM control image of an uncoated Si wafer, the coatings on the Si wafer substrates were all continuously and relatively uniform in appearance, which demonstrated that all of the 5 synthesized precursors (i.e., ammonium Ti(lactate), ammonium Ti(mandelate), ammonium Zr(lactate), ammonium Zr(mandelate), and ammonium Hf(mandelate)) could be successfully utilized in the protamine-enabled layer-by-layer deposition process. These results were consistent with the QCM analyses for the 5 precursors.

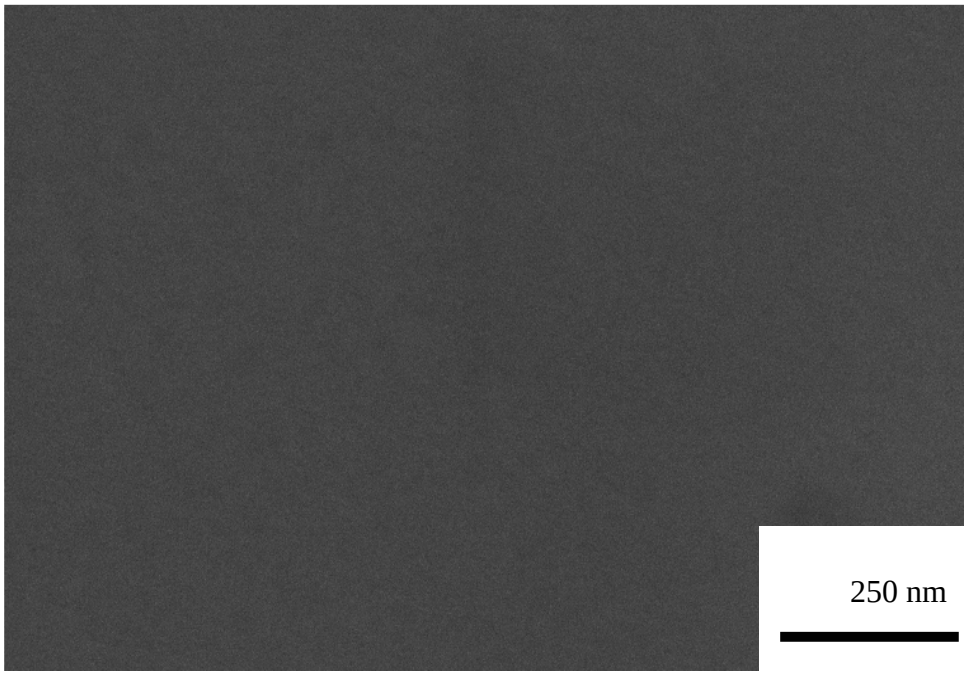

Figure 2.11: Secondary electron images of uncoated Si wafer substrate

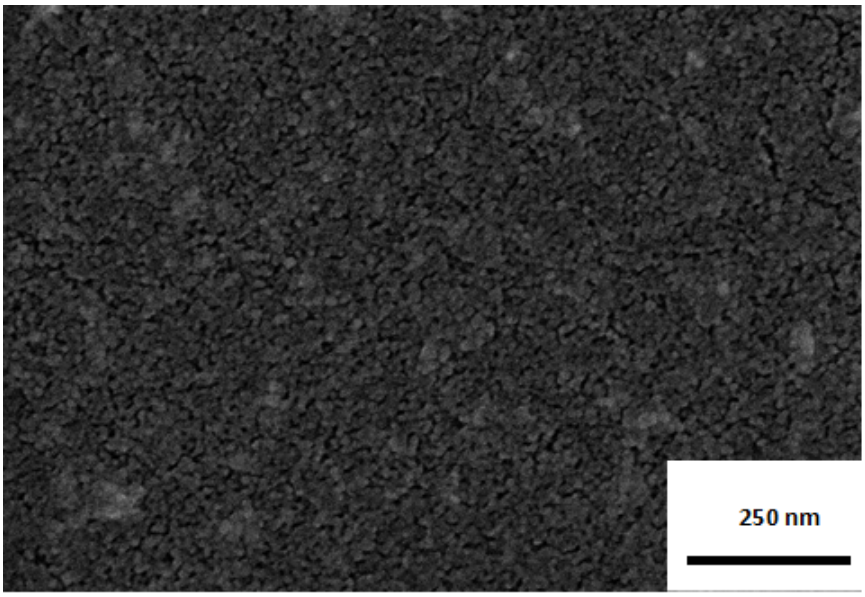

Figure 2.12: Secondary electron image of a TiO_2-coated Si wafer generated with 6 deposition cycles using an ammonium Ti(lactate) precursor after firing at 500℃ for 4 hrs in air.

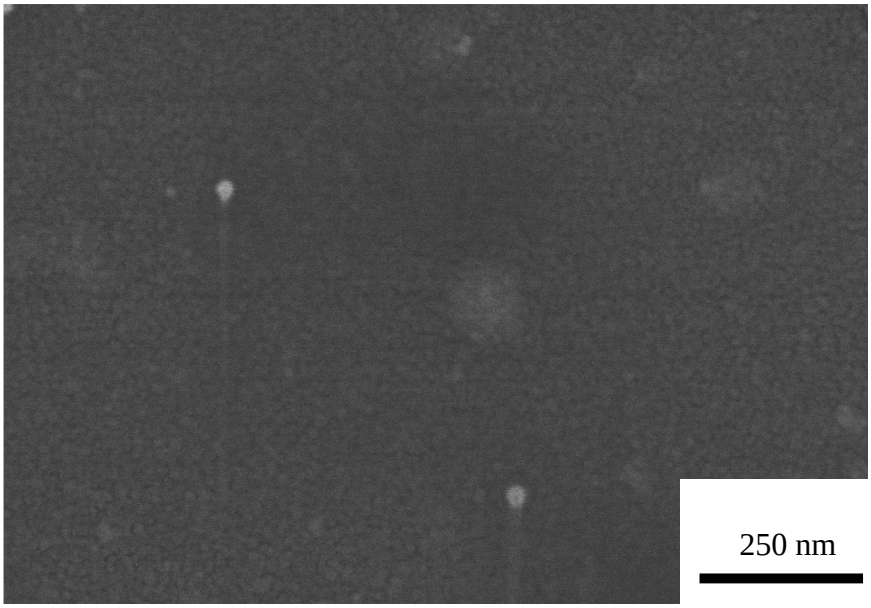

Figure 2.13: Secondary electron image of a TiO_2-coated Si wafer generated with 6 deposition cycles using an ammonium Ti(mandelate) precursor after firing at 500℃ for 4 hrs in air.

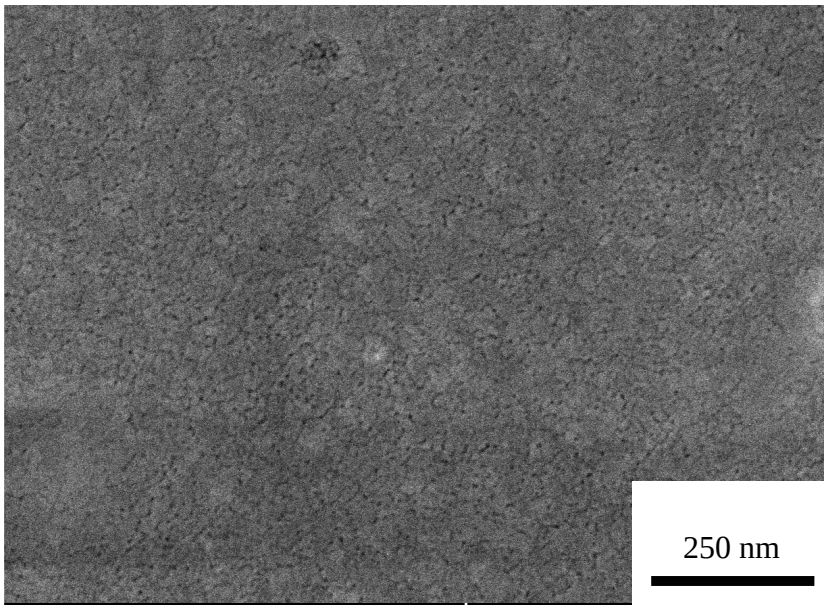

Figure 2.14: Secondary electron image of a ZrO_2-coated Si wafer generated with 6 deposition cycles using an ammonium Zr(lactate) precursor after firing at 600℃ for 6 hrs in air.

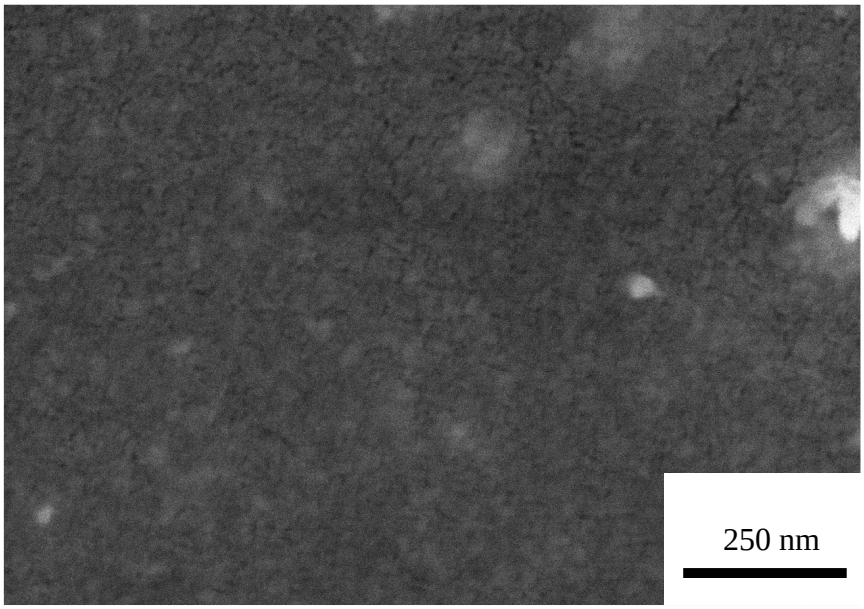

Figure 2.15: Secondary electron image of a ZrO_2-coated Si wafer generated with 6 deposition cycles using an ammonium Zr(mandelate) precursor after firing at 600℃ for 6 hrs in air.

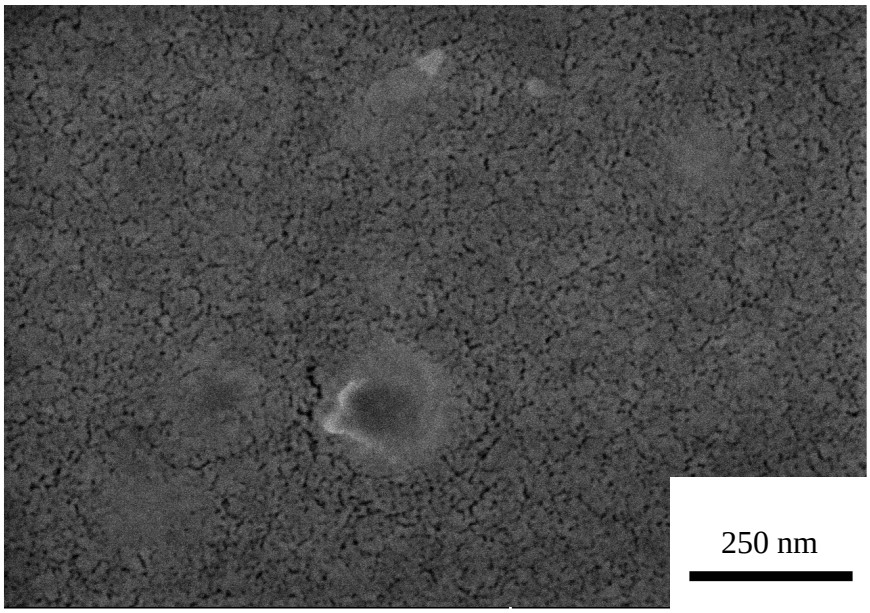

Figure 2.16: Secondary electron image of a HfO_2-coated Si wafer generated with 6 deposition cycles using an ammonium Hf(mandelate) precursor after firing at 600℃ for 6 hrs in air.

From the secondary electron images above of the oxide-coated Si substrates, the coatings were seen to be porous, which was consistent with the removal of the protamine molecules in the films during firing.

(2) TEM analyses of Si substrates coated using ammonium Ti(lactate), ammonium Ti(mandelakte), ammonium Zr(lactate), ammonium Zr(mandelate), ammonium Hf(mandelate) complexes

For TEM characterization, the same samples (i.e., 6-cycles-coated Si wafter substrates by ammonium Ti(lactate), ammonium Ti(mandelate), ammonium Zr(lactate), ammonium Zr(mandelate), and ammonium Hf(mandelate) after firing), were used as for SEM analyses for consistency.

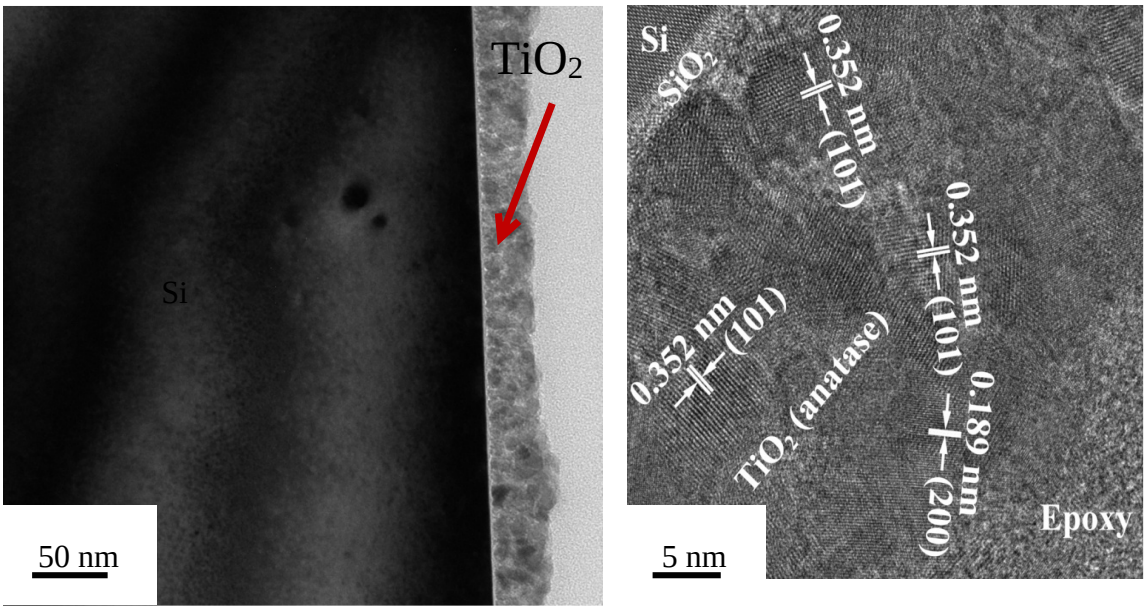

Figure 2.17: TEM images of a TiO_2-coated Si wafer generated with 6 deposition cycles using an ammonium Ti(lactate) precursor after firing at 500℃ for 4 hrs (this is the same sample as used in Fig. 2.12).

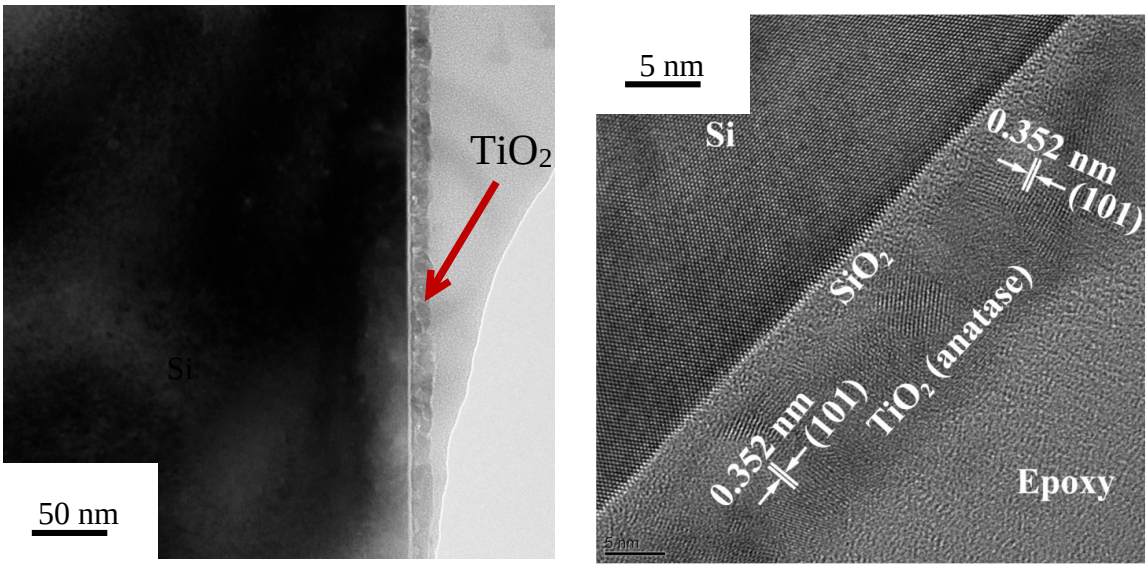

Figure 2.18: TEM images of a TiO_2-coated Si wafer generated with 6 deposition cycles using an ammonium Ti(mandelate) precursor after firing at 500℃ for 4 hrs (this is the same sample as used in Fig. 2.13).

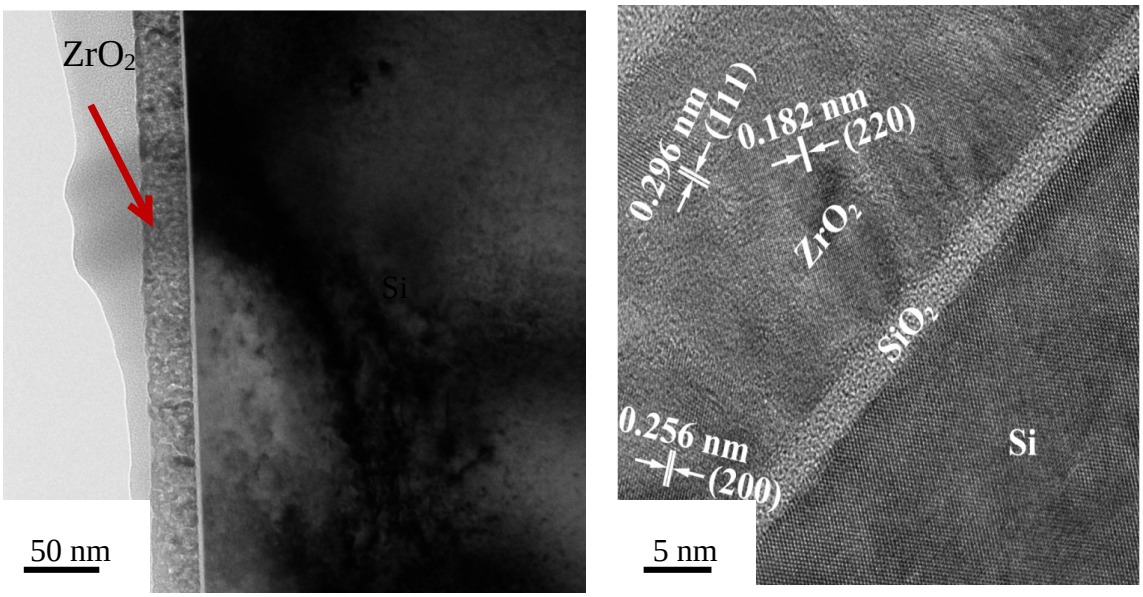

Figure 2.19: TEM images of a ZrO_2-coated Si wafer generated with 6 deposition cycles using an ammonium Zr(lactate) precursor after firing at 600℃ for 6 hrs (this is the same sample as used in Fig. 2.14).

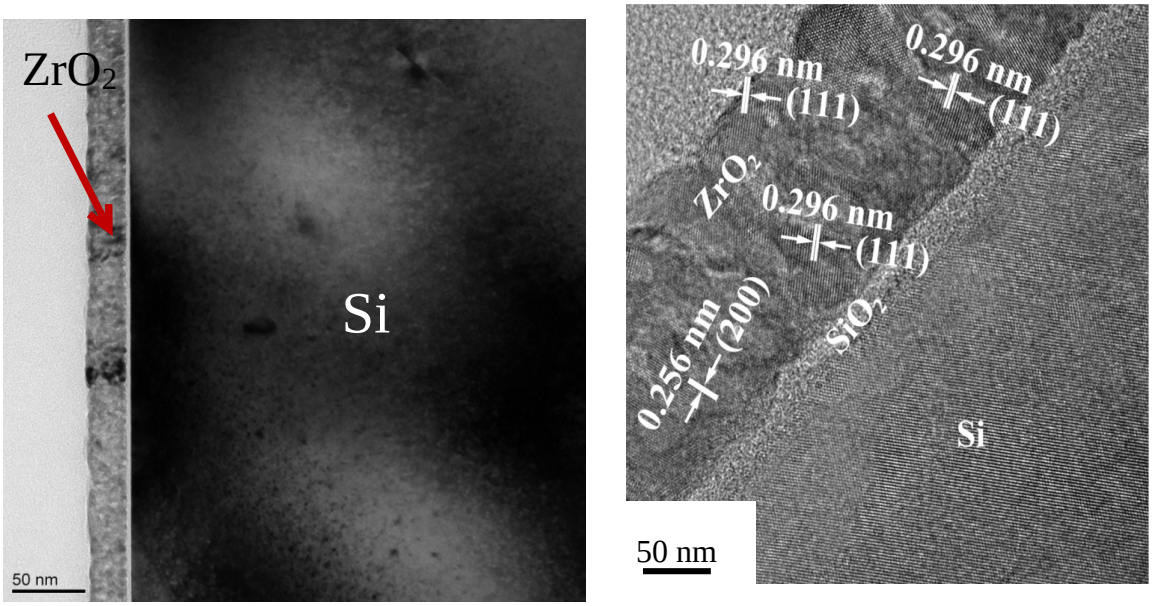

Figure 2.20: TEM images of a ZrO_2-coated Si wafer generated with 6 deposition cycles using an ammonium Zr(mandelate) precursor after firing at 600℃ for 6 hrs (this is the same sample as used in Fig. 2.15).

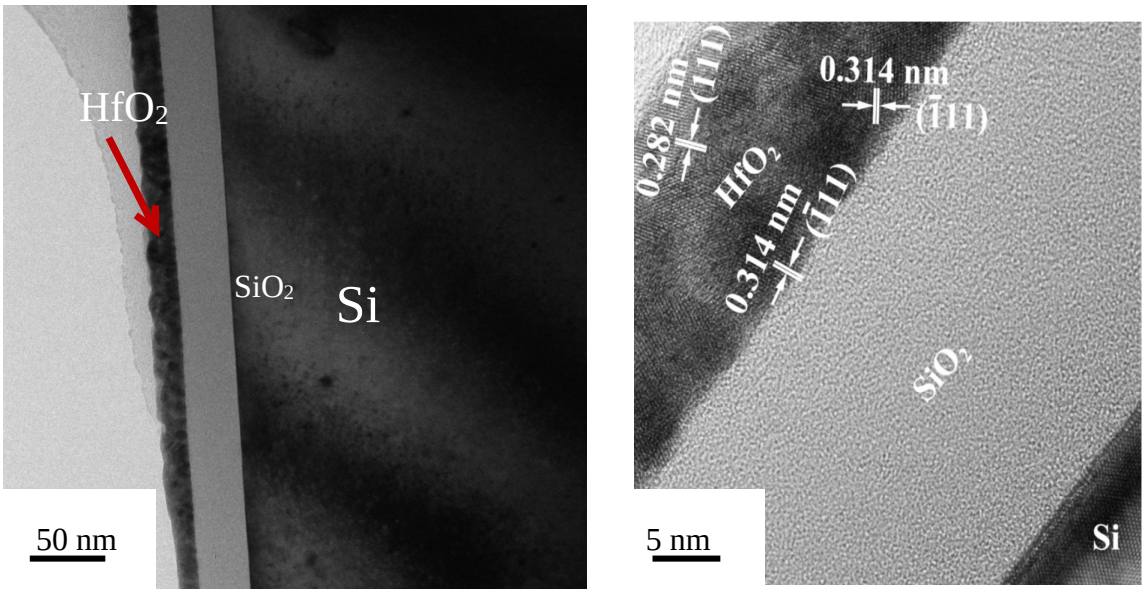

Figure 2.21: TEM images of a HfO_2-coated Si wafer generated with 6 deposition cycles using an ammonium Hf(mandelate) precursor after firing at 600℃ for 6 hrs (this is the same sample as used in Fig. 2.16).

Figs. 2.17 - 2.21 reveal TEM micrographs of the TiO_2, ZrO_2, and HfO_2 nanoparticle-bearing films obtained by protamine-enabled, layer-by-layer deposition using five precursors. The TEM images of these coatings demonstrated that the layer-by-layer deposition process using ammonium Ti(lactate), ammonium Ti(mandelate), ammonium Zr(lactate), ammonium Zr(mandelate), and ammonium Hf(mandelate) were successful in producing continuous and conformal coatings. From **Fig. 2.17 - 2.21** it can be seen that, for the same number of deposition cycles (all these samples were coated using 6 cycles), films generated with ammonium Ti(lactate) possessed the greatest thickness of 38 ± 3.5 nm. Films generated with ammonium Ti(mandelate) were thinner, around 16 ± 1.8 nm from the image, which coincided with the QCM-D analyses. Si wafer substrates coated using ammonium Zr(lactate) and ammonium Zr(mandelate) for the same number of cycles possessed similar thicknesses, 25 ± 1.1 nm, and 27 ± 1.3 nm

respectively. The thickness of Si wafer substrate coated using ammonium Hf(mandelate) was 15 ± 0.5 nm.

Figs. 2.17 - 2.21 also revealed that the coatings after firing contained TiO_2, ZrO_2, or HfO_2 nanocrystals. For the ammonium Ti(lactate) coated sample, the crystals exhibit lattice fringes with *d*-spacings of 3.52 and 1.89 Å, which corresponded, respectively, to the (101) and (200) lattice planes of anatase TiO_2. For the ammonium Ti(mandelate) coated sample, the crystals exhibit lattice fringes with a *d*-spacing of 3.52 Å, which corresponded to the (101) lattice plane of anatase TiO_2. For the ammonium Zr(lactate) coated sample, the crystals exhibit lattice fringes with *d*-spacings of 2.96, 2.56 and 1.82 Å, which corresponded, respectively, to the (111), (200), (220) lattice planes of cubic ZrO_2. For the ammonium Zr(mandelate) coated sample, the crystals exhibit lattice fringes with *d*-spacing of 2.96 and 2.56 Å, which corresponded, respectively, to the (111) and (200) lattice plane of cubic ZrO_2. For the ammonium Hf(mandelate) coated sample, the crystals exhibit lattice fringes with *d*-spacings of 2.82 and 3.14 Å, which corresponded, respectively, to the (111) and (-111) lattice planes of monoclinic HfO_2.

Overall, the SEM and TEM images for the Si wafer substrates coated using the 5 precursors mentioned above demonstrated that these synthesized complexes were effective for generating the corresponding TiO_2, ZrO_2 and HfO_2 films by the protamine-enabled layer-by-layer method.

2.4.3 X-ray Diffraction Analyses of the TiO_2, ZrO_2, HfO_2 Thin Films

X-ray diffraction (XRD) analysis of the coated Si wafter substrates generated with 6 deposition cycles using the ammonium Ti(lactate), ammonium Ti(mandelate),

ammonium Zr(lactate), ammonium Zr(mandelate), or ammonium Hf(mandelate) precursors after firing (the exact same samples as those in SEM and TEM characterization) are shown in **Fig. 2.22 - 2.26**.

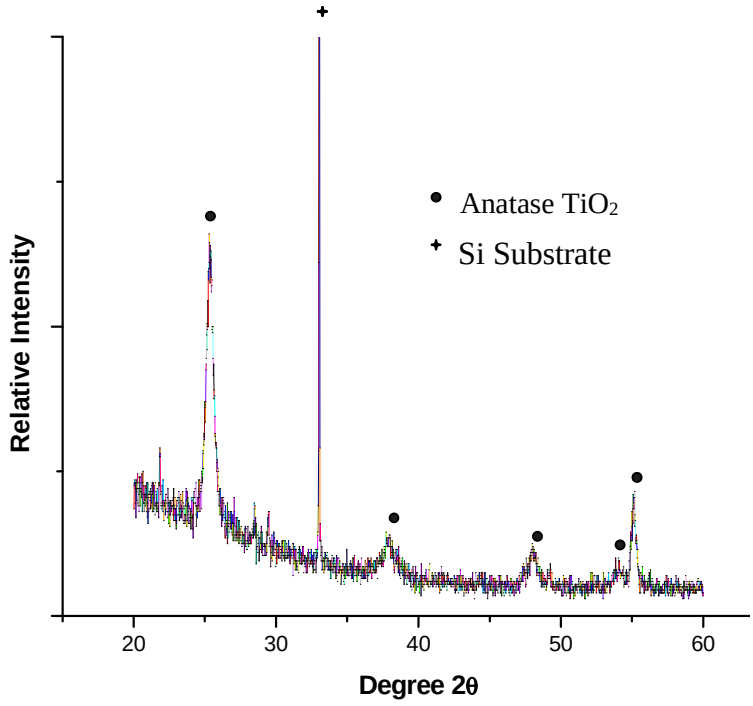

Figure 2.22: XRD analysis of a protamine-enabled TiO_2-coated Si wafer substrate generated with 6 deposition cycles using an ammonium Ti(lactate) precursor after firing at 500℃ for 4 hrs in air.

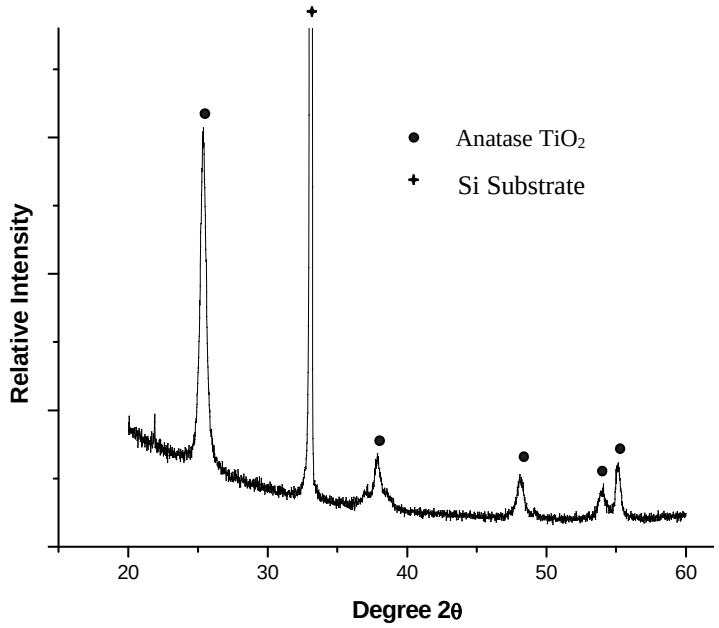

Figure 2.23: XRD analysis of a protamine-enabled TiO_2-coated Si wafer substrate generated with 6 deposition cycles using an ammonium Ti(mandelate) precursor after firing at 500℃ for 4 hrs in air.

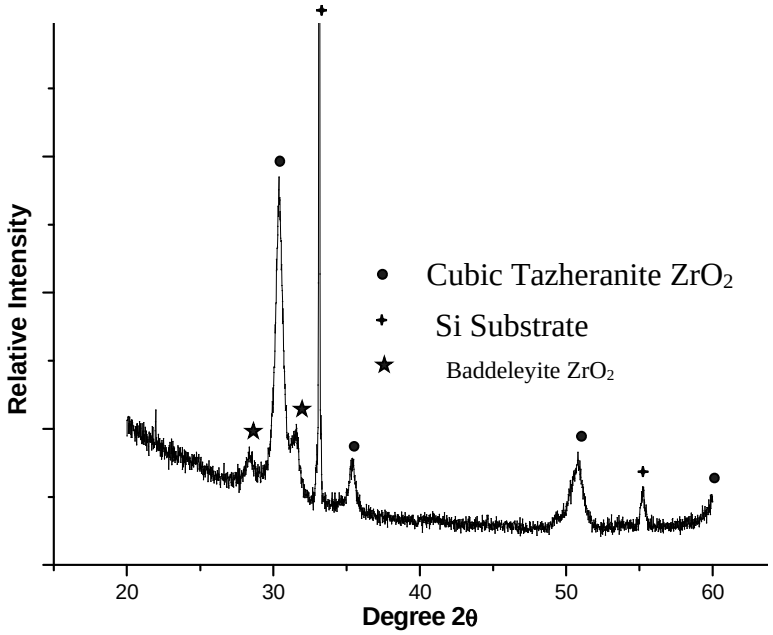

Figure 2.24: XRD analysis of a protamine-enabled ZrO_2-coated Si wafer substrate generated with 6 deposition cycles using an ammonium Zr(lactate) precursor after firing at 600℃ for 6 hrs in air.

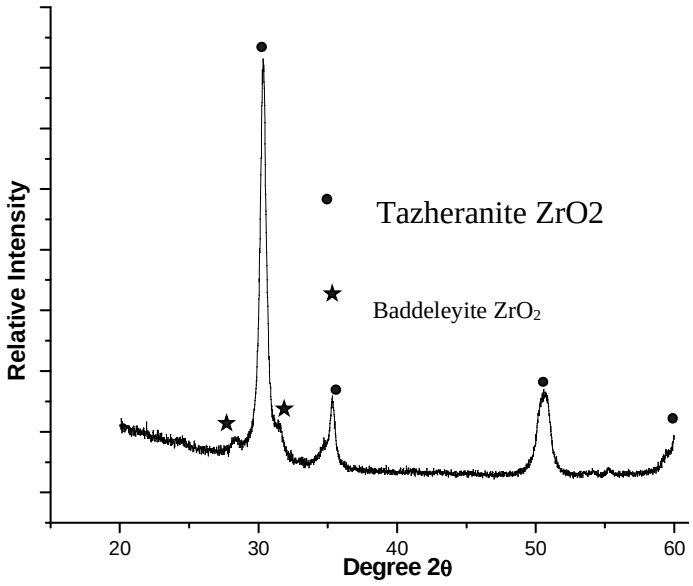

Figure 2.25: XRD analysis of a protamine-enabled ZrO_2-coated Si wafer substrate generated with 6 deposition cycles using an ammonium Zr(mandelate) precursor after firing at 600℃ for 6 hrs in air.

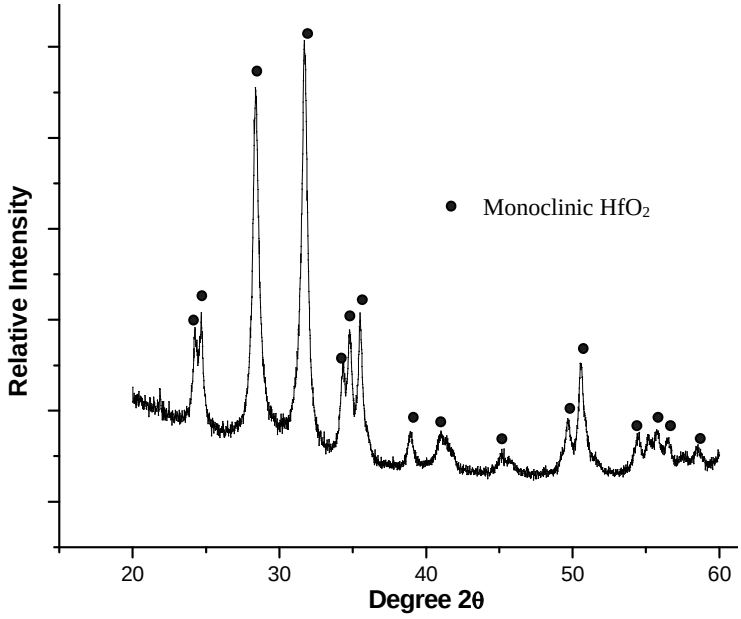

Figure 2.26: XRD analysis of a protamine-enabled HfO_2-coated Si wafer substrate generated with 6 deposition cycles using an ammonium Hf(mandelate) precursor after firing at 600℃ for 6 hrs in air.

From **Fig. 2.22 & Fig. 2.23**, XRD analysis of protamine-enabled coatings using ammonium Ti(lactate) and ammonium Ti(mandelate) precursors after firing at 500℃ for 4 hrs in air yielded peaks for anatase titania (Powder Diffraction File No. 01-71-1166). Scherrer analysis of the most intense anatase TiO_2 diffraction peak (near $2\theta = 25.3°$) in **Fig. 2.22**, for the thin films generated with ammonium Ti(lactate), yielded an average crystal size of 19 ± 1 nm. For the sample coated using ammonium Ti(mandelate), for which the XRD analysis was shown in **Fig. 2.23**, the average crystal size was 16.5± 0.8 nm.

XRD analysis of ammonium Zr(lactate) coated thin film generated with 6 deposition cycles after firing at 600℃ for 6 hrs (**Fig. 2.24**) yielded peaks of cubic tazheranite ZrO_2 (Powder Diffraction File No. 01-071-4810).There were another two peaks with low intensity compared to peaks of ZrO_2, both of which belonged to monoclinic baddeleyite ZrO_2 (Powder Diffraction File No. 01-075-4286). The peak at $2\theta = 28.128°$ corresponds to the (-111) plane of baddeleyite ZrO_2, while the other at $2\theta = 31.480°$ corresponds to the (111) plane of baddeleyite ZrO_2. Scherrer analysis of the most intense tazheranite ZrO_2 diffraction peak (near $2\theta = 30.3°$) in **Fig. 2.24** yielded an average crystal size of 15.1 ± 0.7 nm.

The peak at $2\theta = 33.017°$ in the XRD patterns for films generated using ammonium Ti(mandelate) and ammonium Ti(lactate) (**Figs. 2.22 & 2.23**) was diffracted by the main peak at $2\theta = 69.235°$ which corresponds to the (100) plane of cubic silicon (Powder Diffraction File No. 00-005-0565) of the Si wafer substrate. The XRD pattern of an uncoated Si wafer substrate in **Fig. 2.27** verified this. Similarly, the two peaks in the XRD pattern of film generated using ammonium at $2\theta = 33.017°$ and $2\theta = 55.297°$ are

also from the Si wafer substrate, diffracted by the main peak at the (100) plane of cubic silicon (Powder Diffraction File No. 00-005-0565).

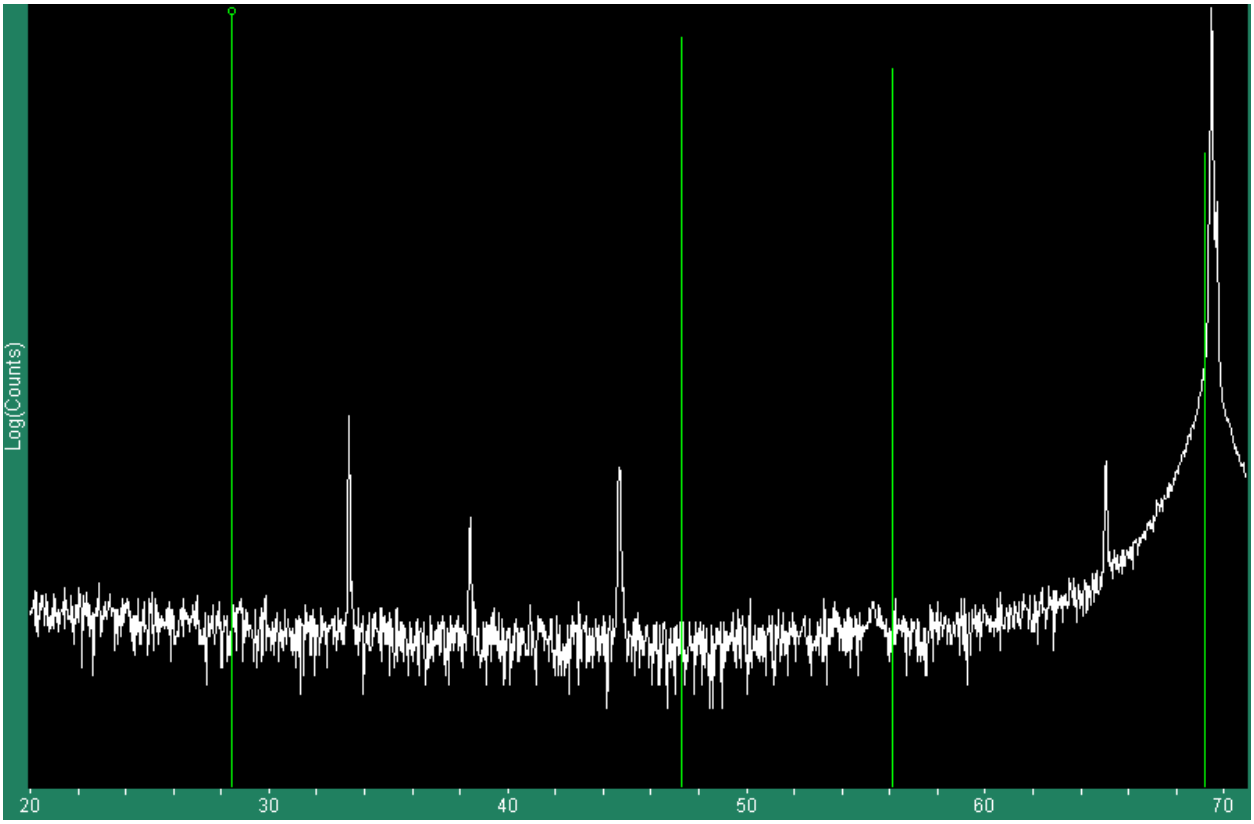

Figure 2.27: XRD analysis of an uncoated Si wafer substrate. Green lines are for the peaks of cubic silicon.

XRD analysis of ammonium Zr(mandelate) coated thin film generated with 6 deposition cycles after firing at 600℃ for 6 hrs (**Fig. 2.25**) yielded peaks of cubic tazheranite ZrO_2 (Powder Diffraction File No. 01-071-4810) with the same two peaks from monoclinic baddeleyite ZrO_2 as in the XRD pattern of ammonium Zr(lactate) coated sample as shown in **Fig. 2.24**. Scherrer analysis of the most intense tazheranite ZrO_2 diffraction peak (near $2\theta = 30.3°$) in **Fig. 2.25** yielded an average crystal size of 19.3 ± 1.2 nm.

XRD analysis of ammonium Hf(mandelate) coated thin film generated with 6 deposition cycles after firing at 600℃ for 6 hrs (**Fig. 2.26**) yielded peaks of HfO_2 (Powder Diffraction File No. 01-075-4290) with no side peaks at all. Scherrer analysis of the most intense HfO_2 diffraction peak (near $2\theta = 31.3°$) in **Fig. 2.26** showed an average crystal size of 14.7 ± 0.9 nm.

2.4.4 Atomic Force Microscopy Characterization of the TiO_2, ZrO_2, and HfO_2 Thin Films

A razor was used to make several cuts through the films generated by protamine-enabled deposition, so that AFM thickness measurements could be conducted between the coated/uncoated regions. From **Fig. 2.28** it can be seen that the coatings were peeled off thoroughly by the razor from the Si wafer substrates. To make sure that the razor only peeled the coatings, and not the silica on the Si wafer surface, a scratch test was conducted on a Si wafer. The test was conducted as follows: 1) a line was made by a marker on a 2 cm * 2 cm Si wafer; 2) a cut was made by a razor through the marker line (perpendicular to the line) on the Si wafer surface; 3) an AFM thickness measurement was conducted on the razor cut region shown in **Fig. 2.29**. The marker line was utilized to position the cut region made by the razor. From **Fig. 2.29** it can be seen that the cut region by the razor was very smooth without any scratches. The results from **Fig. 2.28** and **Fig. 2.29** indicated that this razor cut method can work well to give an accurate AFM thickness measurements of the films generated by protamine-enabled deposition.

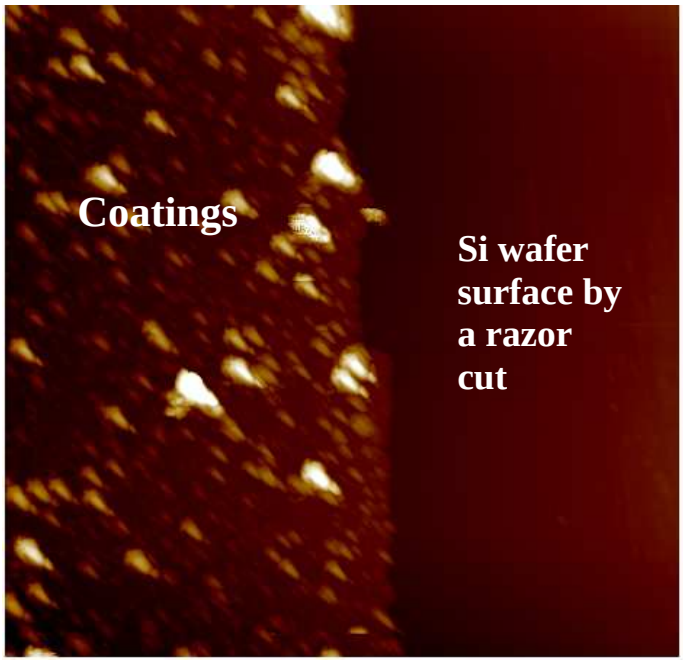

Figure 2.28: A typical *Ex-situ* AFM image (4 cycles of protamine-enabled deposition using ammonium Ti(lactate)) between the boundaries of coated and uncoated regions of Si wafer substrate

Figure 2.29: *Ex-situ* AFM image of the razor cut region in a scratch test.

Ex-situ AFM thickness measurements were taken at the boundaries between coated and uncoated regions on Si wafers to determine the dry film thickness as a function of the number of deposition cycles. Error bars were used to indicate the standard deviation calculated from these measurements. To be consistent with the QCM-D characterization results of the six precursors (i.e., TiBALDH from Sigma, TiBALDH synthesized (ammonium Ti(lactate)), ammonium Ti(mandelate), ammonium Zr(lactate), ammonium Zr(mandelate), and ammonium Hf(mandelate)), the AFM thickness analyses of the coated Si wafers after different number of deposition cycles by the 6 precursors, before and after firing, were compared.

(1) AFM Thickness Analyses of Samples coated using TiBALDH from Sigma, or Synthesized TiBALDH vs. Ammonium Ti(mandelate) precursors

For the coating *thickness* vs. *n* (number of deposition cycles) before firing, films prepared using TiBALDH from Sigma and synthesized TiBALDH both exhibited an exponential fit during cycles 1 - 6, and transitioned to the linear regime afterwards, which was consistent with QCM-D analyses. The coating thickness values for each cycle of ammonium Ti(lactate) and TiBALDH from Sigma were similar (**Fig. 2.30** & **Fig. 2.31)**. The thickness of films prepared using the ammonium Ti(mandelate) complex exhibited a linear fit from cycles 1 to 10, which also coincided with the QCM-D results.

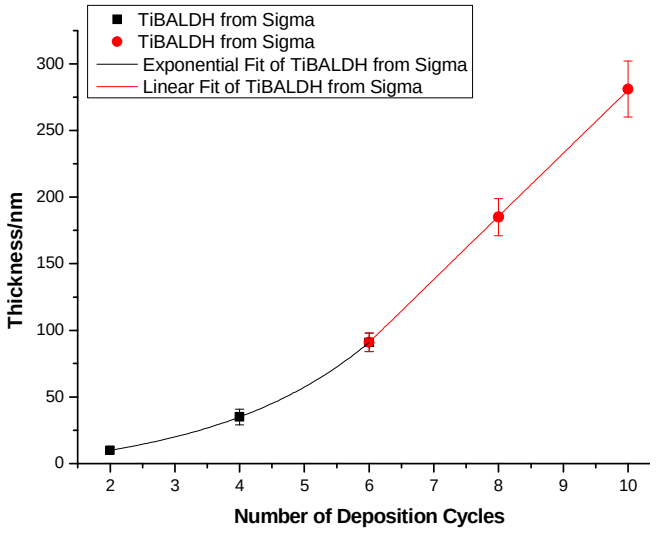

Figure 2.30: *Ex-situ* AFM characterization of the evolution of film thickness with the number of deposition cycles for protamine-enabled films using TiBALDH from Sigma, after drying under flowing N_2 gas for 5 min (after an even number of deposition cycles before firing).

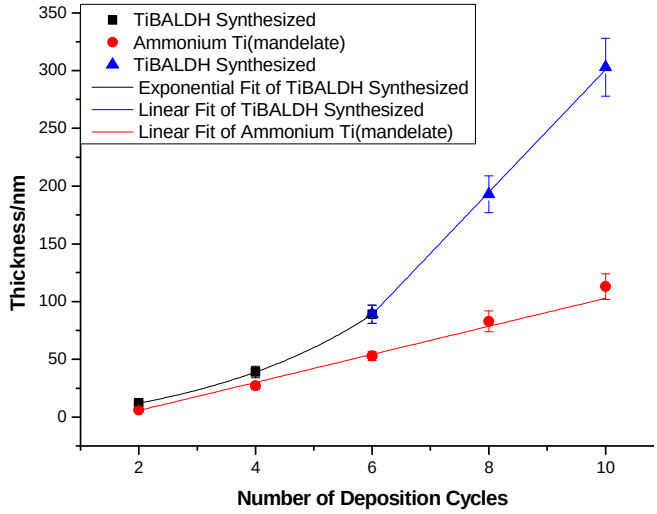

Figure 2.31: *Ex-situ* AFM characterization of the evolution of film thickness with the number of deposition cycles for protamine-enabled films using synthesized TiBALDH and ammoniu Ti(mandelate), after drying under flowing N_2 gas for 5 min (after an even number of deposition cycles before firing).

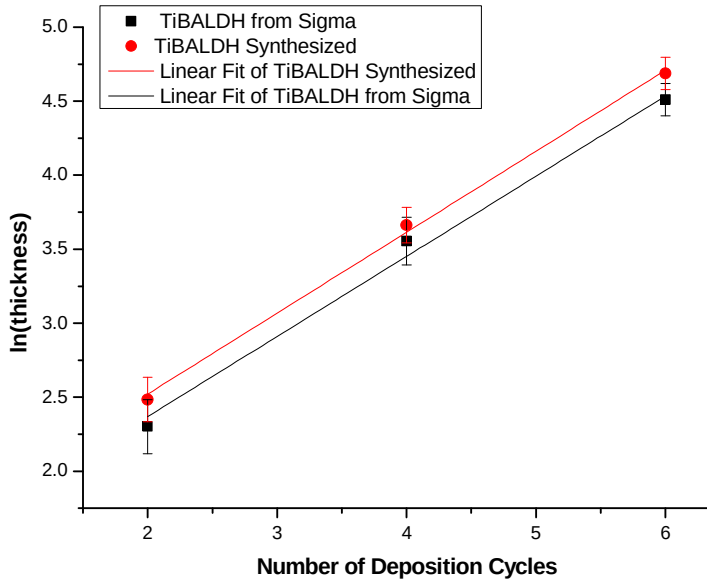

Figure 2.32: The linear dependence of ln(*film thickness*) with *n* (number of deposition cycles) using an ammonium Ti(lactate) (synthesized), or commercial TiBALDH (from Sigma) precursor, before firing.

For protamine-enabled deposition using an ammonium Ti(lactate) precursor before firing, **Equation 2.12** was used to describe the first 6 deposition cycles with an R^2 = 0.9956. For films prepared using TiBALDH from Sigma before firing, **Equation 2.13** was used to describe the deposition behavior for cycles 1 to 6 with an R^2 = 0.9917. For films prepared with the ammonium Ti(mandelate) complex before firing, **Equation 1.14** was used to describe deposition behavior for cycles 1 to 10 with an R^2= 0.99029.

$$\text{Thickness} = -19.69565+17.11565\exp^{(0.30809*n)} \qquad (2.12)$$

$$\text{Thickness} = -10.16129+9.00058\exp^{(0.40324*n)} \qquad (2.13)$$

$$\text{Thickness} = -18+12.2*n \qquad (2.14)$$

The linear dependence of ln(*thickness*) with *n* for the first six cycles for films prepared using synthesized TiBALDH and TiBALDH from Sigma are shown in **Fig. 2.32**. The linear fit for films prepared with synthesized TiBALDH for cycles 1 to 6 yielded a

reasonable R^2=0.9964, as described by **Equation 2.15**. For films prepared using TiBALDH from Sigma, the deposition behavior for cycles 1 to 6 with R^2= 0.98918 **.**

$$\ln(thickness) = 1.43 + 0.546*n \quad (2.15)$$

$$\ln(thickness) = 1.29 + 0.541*n \quad (2.16)$$

From the plots in **Fig. 2.30 & 2.31**, it was apparent that the exponential equation failed to fit data points beyond the sixth deposition cycle. After the sixth deposition cycle, the *thickness* of films prepared using the ammonium Ti(lactate) precursor increased at a linear rate of 53 ± 4 nm per cycle (R^2=0.9995). The *thickness* of films prepared using the TiBALDH from Sigma increased at a linear rate of 47 ± 5 Hz per cycle (R^2=0.9919). These results suggested that an exponential-to-linear transition occurred at the sixth deposition cycle for these films.

AFM thickness measurements were only conducted on the Si wafers coated by ammonium Ti(lactate) (i.e. synthesized TiBALDH), or ammonium Ti(mandelate) complex solutions after firing.

From **Fig. 2.33 & 2.34**, it can be seen that the evolution of the thickness of these coated films after firing followed the same pattern as before firing; that is, films prepared with synthesized TiBALDH precursor exhibited exponential deposition behavior from cycles 1 to 6, and transitioned to a linear regime afterwards. The thickness of films prepared with the ammonium Ti(mandelate) complex exhibited linear deposition behavior from cycles 1 to 10, which was also similar to the films before firing. However, the thickness of the films decreased significantly after firing. These thickness results of the films after firing also matched well with the TEM analyses. From TEM analyses, the

film generated with ammonium Ti(lactate) for 6 cycles after firing possessed a thickness of 38 ± 3.5 nm, and films generated with ammonium Ti(mandelate) for 6 cycles after firing possessed a thickness of 16 ± 1.8 nm, while in AFM results, the film prepared with the ammonium Ti(lactate) precursor for 6 cycles had a thickness of 41 ± 4 nm, the film prepared with the ammonium Ti(mandelate) precursor for 6 cycles had a thickness of 19 ± 2 nm.

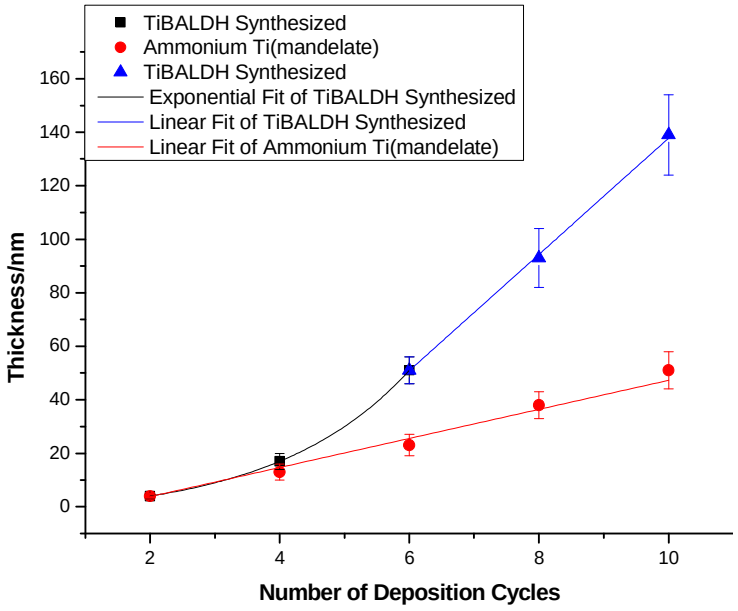

Figure 2.33: *Ex-situ* AFM characterization of the evolution of film thickness with the number of deposition cycles after firing of protamine-derived films generated using synthesized TiBALDH and ammonium Ti(mandelate) precursors.

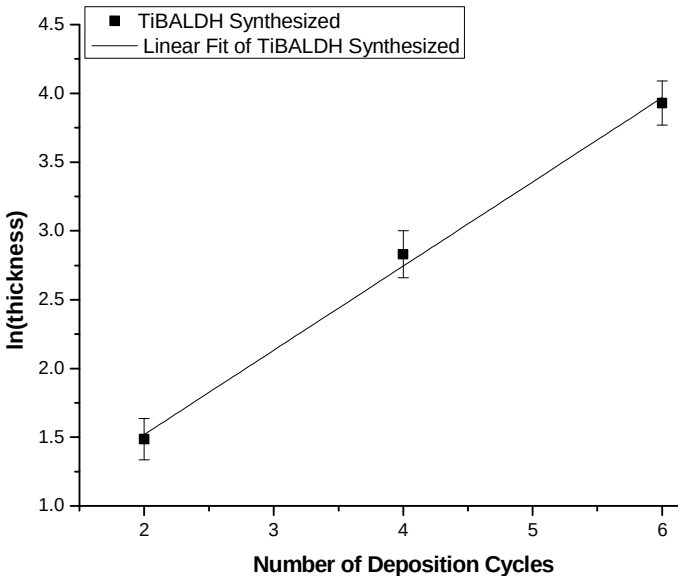

Figure 2.34: The linear dependence of ln(*film thickness*) with *n* for fired films generated with ammonium Ti(lactate) (synthesized) precursor.

For protamine-enabled films prepared using ammonium Ti(lactate) after firing, **Equation 2.17** was used to fit the deposition behavior for cycles 1 - 6 with an R^2 = 0.9986. For films prepared using the ammonium Ti(mandelate) complex after firing, **Equation 2.18** was used to fit the deposition behavior for cycles 1 to 10 with an R^2= 0.9857.

$$\text{Thickness} = -4.05+3.08\exp^{(0.48*n)} \qquad (2.17)$$

$$\text{Thickness} = -7.06+5.43*n \qquad (2.18)$$

The linear dependence of ln(*film thickness*) with *n* for the first six deposition cycles for films prepared using ammonium Ti(lactate) (i.e., synthesized TiBALDH) after firing is shown in **Fig. 2.34**. For films prepared with synthesized TiBALDH, deposition behavior followed **Equation 2.19** with R^2=0.99419.

$$\ln(thickness) = 0.295 + 0.612*n \qquad (2.19)$$

From the plot in **Fig. 2.33**, it was apparent that the exponential equation failed to fit data points beyond the sixth deposition cycle for films prepared with the synthesized TiBALDH precursor. After the sixth deposition cycle, the *thickness* of ammonium Ti(lactate) after firing increased at a linear rate of 22 ± 3 nm per cycle (R^2=0.9988), which suggested that an exponential-to-linear transition occurred at the sixth deposition cycle.

(2) AFM Analyses of Samples coated using Ammonium Zr(lactate) or Ammonium Zr(mandelate) vs. Ammonium Hf(mandelate) Precursors

The AFM thickness values for films on the Si wafer substrates of the coating with ammonium Zr(lactate), ammonium Zr(mandelate) and ammonium Hf(mandelate) (before firing) were shown in **Figs. 2.35 - 2.40**.

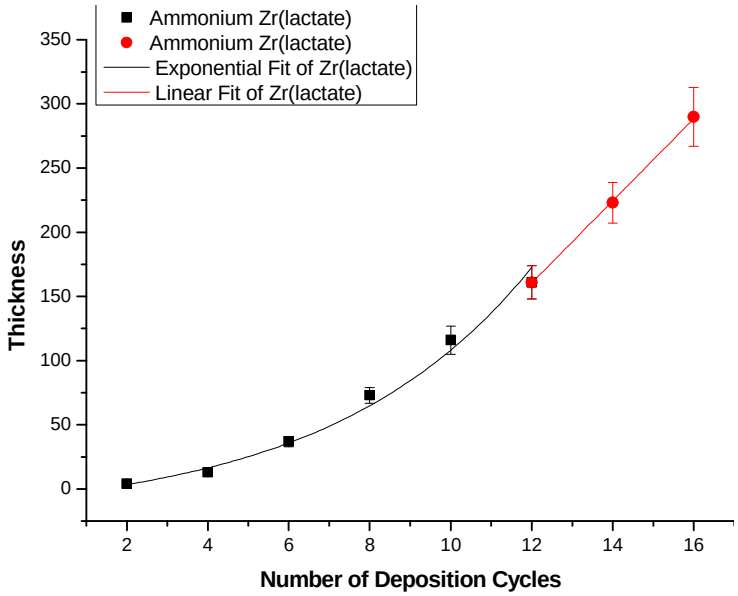

Figure 2.35: *Ex-situ* AFM characterization of the evolution of film thickness for protamine-derived films prepared using an ammonium Zr(lactate) precursor (after drying for 5 min. in flowing N_2(g) at room temperature).

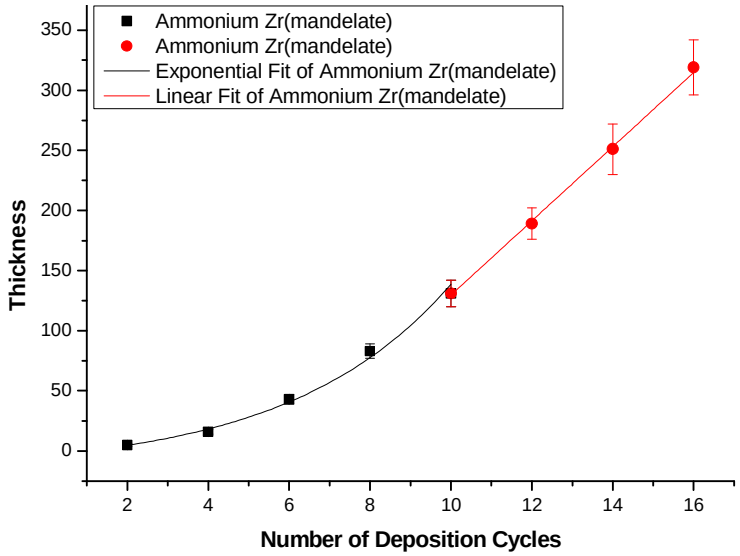

Figure 2.36: *Ex-situ* AFM characterization of the evolution of film thickness for protamine-derived films prepared using an ammonium Zr(mandelate) precursor (after drying for 5 min. in flowing N_2(g) at room temperature).

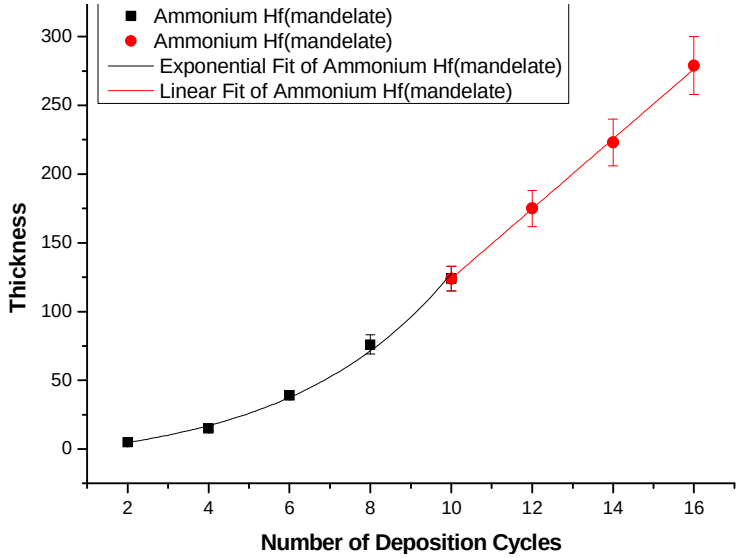

Figure 2.37: *Ex-situ* AFM characterization of the evolution of film thickness for protamine-derived films prepared using an ammonium Hf(mandelate) precursor (after drying for 5 min. in flowing N_2(g) at room temperature).

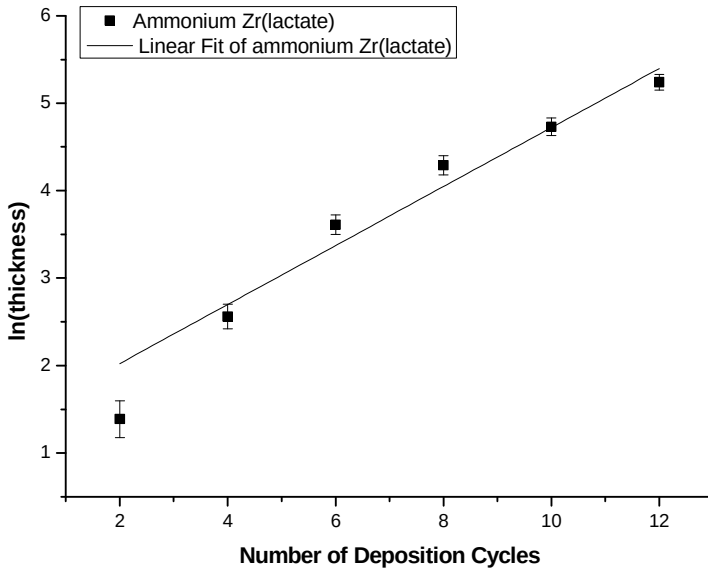

Figure 2.38: The linear dependence of ln(*film thickness*) with *n* for protamine-derived films prepared using ammonium Zr(lactate) from cycles 1 to 12, before firing (after drying for 5 min. in flowing N_2(g) at room temperature).

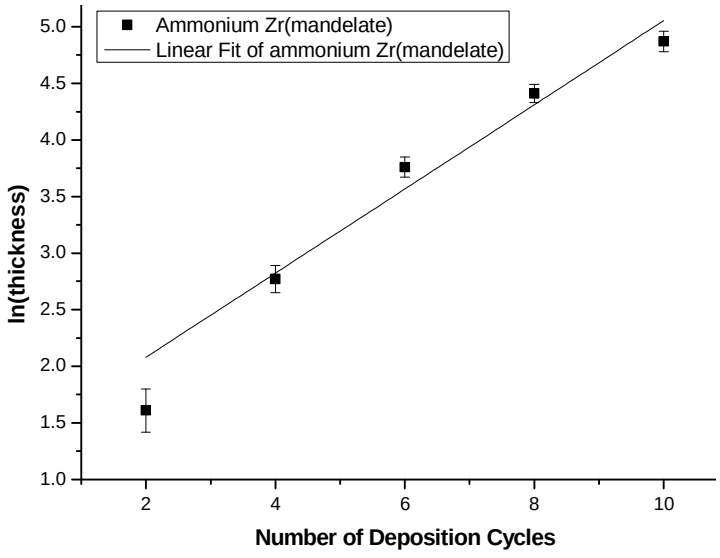

Figure 2.39 The linear dependence of ln(*film thickness*) with *n* for protamine-derived films prepared using ammonium Zr(mandelate) from cycles 1 to 10, before firing (after drying for 5 min. in flowing N_2(g) at room temperature).

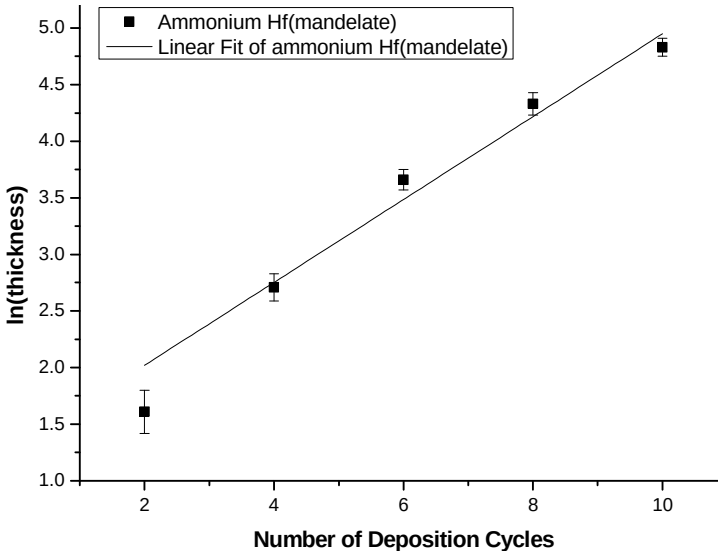

Figure 2.40: The linear dependence of ln(*film thickness*) with *n* for protamine-derived films prepared using ammonium Hf(mandelate) from cycles 1 to 10, before firing (after drying for 5 min. in flowing N_2(g) at room temperature).

From **Figs. 2.35 - 2.37**, it can be seen that the thickness growth pattern of the coated substrates by all three precursors (i.e. ammonium Zr(lactate), ammonium Zr(mandelate) and ammonium Hf(mandelate)) were in accord with the QCM-D results. The AFM-derived film thickness was only measured on samples after an even number of deposition cycles, while the transitional point from exponential to linear growth of films prepared using ammonium Zr(lactate) via QCM-D analyses occurred in the 13th cycle. From **Fig. 2.35** it can be seen that, by AFM, the transitional point was at about 12th cycle. For ammonium Zr(mandelate) and ammonium Hf(mandelate), the case was similar. The transitional points from exponential growth to linear in QCM-D analyses of ammonium Zr(mandelate) and ammonium Hf(mandelate) were both at the 9th cycle while in **Fig. 2.36** and **Fig. 2.37** such transitions appeared at about the 10th cycle. While the frequency change for each cycle with ammonium Zr(mandelate) was a little higher than that of ammonium Zr(lactate), the AFM thicknesses before firing for each cycle for these two

precursors were similar. There are several possible reasons for inconsistency of the QCM-D and AFM results for films generated by protamine-enabled deposition using ammonium Zr(lactate) and ammonium Zr(mandelate). Firstly, the Sauerbrey model is limited to rigid films exhibiting a change in dissipation (ΔD) of less than 1 Hz.[46] Thus, after 4 deposition cycles, the frequency change of QCM-D results isn't necessarily proportional to the mass of the precipitates on the sensor during the deposition process. Secondly, it can be seen from **Fig. 2.41** that for each deposition cycle, the dissipation change of films generated by protamine-enabled deposition using ammonium Zr(lactate) was larger than that for ammonium Zr(mandelate), which suggested that film generated using ammonium Zr(lactate) had larger viscoelasticity and thus was less rigid and had a lower density than the film generated using ammonium Zr(mandelate). Thus, with higher deposition frequency change, the films generated using ammonium Zr(mandelate) had similar thicknesses as that for the films generated using ammonium Zr (lactate).

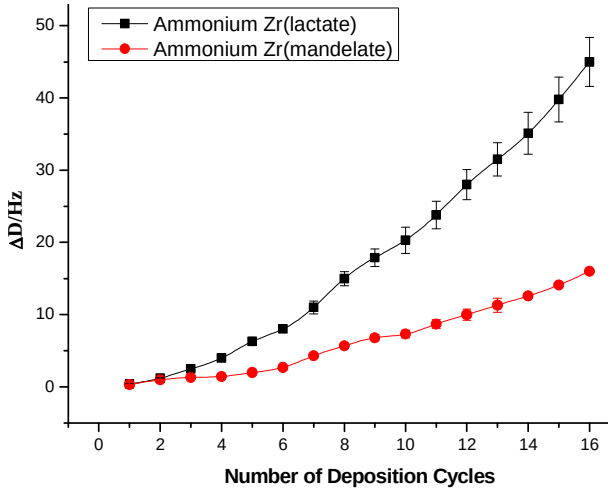

Figure 2.41: Plot of ΔD *vs.* n using the 5th harmonic from QCM-D measurement of protamine-enabled deposition using ammonium Zr(lactate) and ammonium Zr(mandelate) precursor solutions over 16 cycles. Error bars represent the standard deviation recorded from two experiments.

For protamine-enabled films prepared using ammonium Zr(lactate) before firing, **Equation 2.20** was used to fit the deposition behavior for cycles 1 - 12 with $R^2 = 0.97418$. For films prepared with ammonium Zr(mandelate) before firing, **Equation 2.21** was used to describe the deposition behavior for cycles 1 - 10 with an $R^2 = 0.98375$. For films prepared with ammonium Hf(mandelate) before firing, **Equation 2.22** was used to describe the deposition behavior for cycles 1 - 10 with $R^2 = 0.98935$.

$$\text{Thickness} = -22.9+17.7\exp^{(0.2*n)} \quad (2.20)$$

$$\text{Thickness} = -16.2+12.6\exp^{(0.25*n)} \quad (2.21)$$

$$\text{Thickness} = -13.9+11.2\exp^{(0.24*n)} \quad (2.22)$$

The linear dependence of ln(*film thickness*) with *n* for the first 12 deposition cycles for films prepared using ammonium Zr(lactate), and for the first 10 cycles using ammonium Zr(mandelate) and ammonium Hf(mandelate) before firing was shown in **Figs. 2.38 - 2.40**. The linear fit of films prepared using ammonium Zr(lactate) for cycles 1 to 12 followed **Equ. 2.23** with $R^2=0.94401$. For films prepared using ammonium Zr(mandelate), for cycles 1 to 10 deposition behavior followed **Equ. 2.24** with $R^2= 0.94302$. For films prepared using ammonium Hf(mandelate), the fitting equation is shown in **Equ. 2.25** with $R^2= 0.96007$.

$$\ln(\textit{thickness}) = 1.35 + 0.34*n \quad (2.23)$$

$$\ln(\textit{thickness}) = 1.34+ 0.37*n \quad (2.24)$$

$$\ln(\textit{thickness}) = 1.29+ 0.36*n \quad (2.25)$$

From the plots in **Fig. 2.35 - 2.37**, it can be seen that after the 12th deposition cycle, the *thickness* of films prepared using ammonium Zr(lactate) increased at a linear rate of

32 ± 4 nm per cycle (R^2=0.9989). After the 10th cycle, the *thickness* of films prepared using ammonium Zr(mandelate) increased at a linear rate of 30 ± 3.5 nm per cycle (R^2=0.99798). The *thickness* of films prepared using ammonium Hf(mandelate) increased at a linear rate of 25.5 ± 2.8 nm per cycle (R^2=0.99907). These results suggested that the thickness growth mechanism of protamine-derived films prepared using these three precursors followed the active volume model.

As the thickness growth patterns of the samples using by ammonium Zr(lactate), ammonium Zr(mandelate), and ammonium Hf(mandelate) before firing were similar, the AFM thickness measurements after firing were only conducted on the ammonium Zr(mandelate) coated samples as shown below in **Fig. 2.42 & 2.43**.

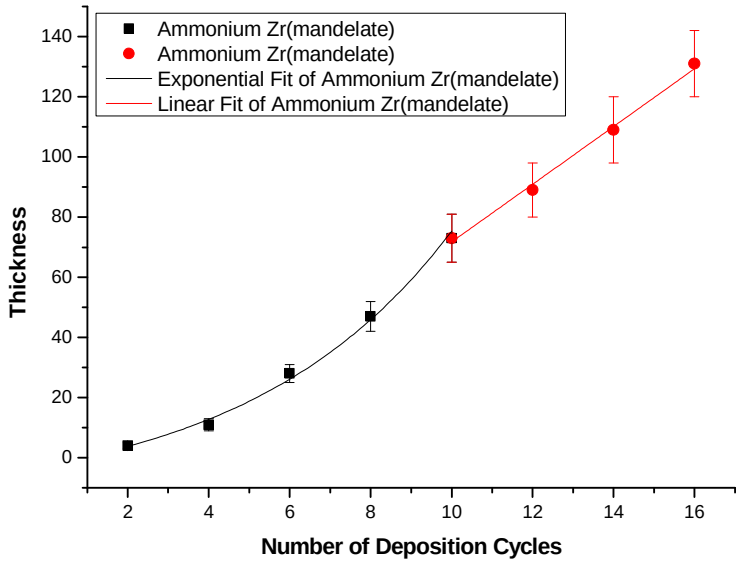

Figure 2.42: *Ex-situ* AFM characterization of the evolution of film thickness for protamine-derived films prepared using ammonium Zr(mandelate) precursor after firing.

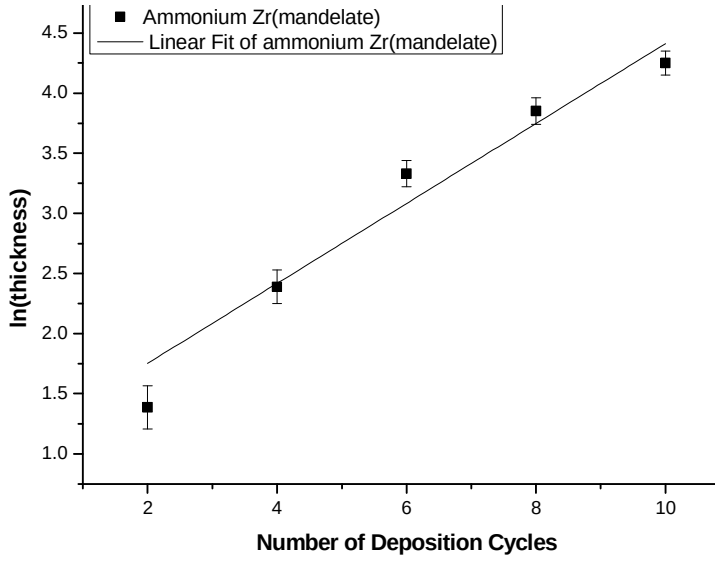

Figure 2.43: The linear dependence of ln(*film thickness*) with *n* for protamine-derived films prepared using an ammonium Zr(mandelate) precursor after firing.

From **Figure 2.42**, it can be seen that the evolution of the film thickness of these coated films prepared with ammonium Zr(mandelate), after firing followed the same pattern as before firing. The transitional point from exponential to linear growth, obtained from the *thickness* - *n* plot, occurred at the 10^{th} cycle.

For protamine-enabled films prepared with ammonium Zr(mandelate) after firing, **Equ. 2.26** was used to fit the deposition behavior for cycles 1 - 10 with $R^2 = 0.98555$.

$$\text{Thickness} = -14.7+12.4\exp^{(0.20*n)} \qquad (2.26)$$

The linear dependence of ln(*film thickness*) with *n* for the first 10 cycles for films prepared using ammonium Zr(mandelate) was shown in **Fig. 2.43**. The linear fit for cycles 1 to 10 followed **Equ. 2.27** with $R^2=0.9366$.

$$\ln(\textit{thickness}) = 1.09 + 0.33*n \qquad (2.27)$$

After the 10th deposition cycle, the *thickness* of ammonium Zr(mandelate) after firing increased at a linear rate of 9.5 ± 1.5 nm per cycle (R^2=0.9926), which suggested that an exponential-to-linear transition occurred at the 10th deposition cycle.

The thickness results of the film generated by protamine-enabled deposition using ammonium Zr(mandelate) after firing also matched well with the TEM characterization results. In TEM analyses, film generated with ammonium Zr(mandelate) for 6 cycles after firing possessed the thickness of 27 ± 1.3 nm, while in AFM results, the film prepared with the ammonium Ti(lactate) precursor for 6 cycles had a thickness of 31 ± 2.4 nm.

Overall, the AFM thickness results for ammonium Ti(lactate), ammonium Ti(mandelate), ammonium Zr(lactate), ammonium Zr(mandelate), ammonium Hf(mandelate), before and after firing, were consistent with the QCM-D analyses in confirming again that these five synthesized complexes did serve as effective precursors for the protamine-enabled layer-by-layer deposition of conformal TiO_2, ZrO_2 and HfO_2 films.

2.5 SUMMARY AND OUTLOOK

In this work, Ti-, Zr- and Hf-containing complexes with different types of ligands (discussed in the previous chapter) were utilized in a protamine-enabled, layer-by-layer deposition process for the fabrication of corresponding TiO_2, ZrO_2 and HfO_2 thin films.

QCM-D analyses of these complexes indicated that the citrate precursors (i.e., ammonium Ti(citrate), ammonium Zr(citrate), ammonium Hf(citrate) complex solutions) were ineffective in the layer-by-layer deposition process. Films prepared with ammonium Ti(lactate) were thicker after every coating cycle than films prepared with ammonium Ti(mandelate). The deposition behavior for the ammonium Ti(lactate) precursor was consistent with an active volume model, which was similar to that for films prepared using TiBALDH from Sigma. For films prepared with ammonium Ti(mandelate), linear film growth occurred during the layer-by-layer deposition process. For films prepared with ammonium Zr(lactate) and ammonium Zr(mandelate), the amount of deposition amount per cycle was similar, and the protamine enabled layer-by-layer deposition behavior was consistent with an active volume model" with a transitional point from exponential to linear growth during deposition process. Films prepared using ammonium Hf(mandelate) exhibited the same deposition behavior as for ammonium Zr(lactate) and ammonium Zr(mandelate). However, the deposition amount of material for ammonium Hf(mandelate) for each cycle was less than for ammonium Zr(lactate) and ammonium Zr(mandelate). The AFM analyses yielded similar deposition results.

The SEM, TEM, and XRD analyses of the coated substrates for all five precursors after firing revealed that the TiO_2, ZrO_2, and HfO_2 coatings were continuous and conformal.

From the QCM-D and AFM analyses, the metal and ligand types of the precursors were found to affect the deposition behavior (i.e., the deposition amount, deposition mechanism). Future work on the determination of the structure of the precursors by multiple analytical methods may help in understanding the mechanisms for such protamine-enabled deposition process. Furthermore, by synthesizing other aqueous precursors for other transitional metals, the peptide-enabled layer-by-layer deposition could be extended to the fabrication of other functional mineral oxide thin films for various technological uses.

2.6 REFERENCES

[1] M. Darder, P. Aranda, E.R. Hitzky, "Bionanocomposites: A new concept of ecological, bioinspired, and functional hybrid materials", *Adv. Mater.* 2007, **19**, 1309–1319.

[2] W. Ogasawara, W. Shenton, S.A. Davis, and S. Mann, "Template mineralization of ordered macroporous chitin-silica composites using a cuttlebone-derived organic matrix", *Chem. Mater.* 2000, **12**, 2835–2837.

[3] D. Lazos, S. Franzka, M. Ulbricht, "Size-selective protein adsorption to polystyrene surfaces by self-assembled grafted poly(ethylene glycols) with varied chain lengths", *Langmuir* 2005, **21**, 8774–8784.

[4] P. Ye, Z.K. Xu, A.F. Che, J. Wu and P. Seta, "Chitosan-tethered poly(acrylonitrile-co-maleic acid) hollow fiber membrane for lipase immobilization", *Biomaterials* 2005, **26**, 6394–6403.

[5] J. Aizenberg, J.C. Weaver, M.S. Thanawala, V.C. Sundar, D.E. Morse and P. Fratzl, "Skeleton of Euplectella sp.: Structural hierarchy from the nanoscale to the macroscale", *Science*, 2005, **309**, 275.

[6] C. Sollner, M. Burghammer, E.B. Nentwich, I. Berger, H. Schwarz, C. Riekel and T. Nicolson, "Control of crystal size and lattice formation by starmaker in otolith biomineralization", *Science*, 2003, **302**, 282.

[7] S. Mann, "Biomineralization: the form(id)able part of bioinorganic chemistry", *J. Chem. Soc., Dalton Trans.*, 1997, 3953.

[8] J. Aizenberg, D.A. Muller, J.L. Grazul and D.R. Hamann, "Direct fabrication of large micropatterned single crystals", *Science*, 2003, **299**, 1205

[9] C. Sanchez, H. Arribart and M.M.G. Guille, "Biomimetism and bioinspiration as tools for the design of innovative materials and systems", *Nat. Mater*., 2005, **4**, 277.

[10] J.S. Jan and D.F. Shantz, "Biomimetic silica formation: Effect of block copolypeptide chemistry and solution conditions on silica nanostructure"*Adv. Mater*., 2007, **19**, 2951.

[11] M. Sumper and E. Brunner, "Learning from diatoms: Nature's tools for the production of nanostructured silica", *Adv. Funct. Mater.*, 2006, **16**, 17.

[12] N. Kroger, R. Deutzmann and M. Sumper, "Polycationic peptides from diatom biosilica that direct silica nanosphere formation", *Science*, 1999, **286**.1129-1132

[13] N. Kroger, S. Lorenz, E. Brunner and M. Sumper, "Self-Assembly of Highly Phosphorylated Silaffins and Their Function in Biosilica Morphogenesis", *Science*, 2002, **298**, 584.

[14] Y. Zhou, K. Shimizu, J.N. Cha, G.D. Stucky and D.E. Morse, "Efficient Catalysis of Polysiloxane Synthesis by Silicatein α Requires Specific Hydroxy and Imidazole Functionalities", *Angew. Chem., Int. Ed.*, 1999, **38**, 779.

[15] H.R. Luckarift, J.C. Spain, R.R. Naik and M.O. Stone, "Enzyme immobilization in a biomimetic silica support", *Nat. Biotechnol.*, 2004, **22**, 211.

[16] F. Rodriguez, D.D. Glawe, R.R. Naik, K.P. Hallinan and M.O. Stone, "Study of the chemical and physical influences upon in vitro peptide-mediated silica formation", *Biomacromolecules*, 2004, **5**, 261.

[17] S.V. Patwardhan, S.J. Clarson and C.C. Perry, "On the role(s) of additives in bioinspired silicification", *Chem. Commun.*, 2005, 1113.

[18] S.V. Patwardhan and S.J. Clarson, "Silicification and biosilicification - Part 6. Poly- L-histidine mediated synthesis of silica at neutral pH", *J. Inorg. Organomet. Polym.*, 2003, **13**, 49.

[19] S.V. Patwardhan, V.P. Taori, M. Hassan, N.R. Agashe, J.E. Franklin, G. Beaucage, J.E. Mark and S.J. Clarson, "An investigation of the properties of poly(dimethylsiloxane)-bioinspired silica hybrids", *Eur. Polym. J.*, 2006, **42**, 167.

[20] S.V. Patwardhan, and S.J. Clarson, "Bioinspired mineralisation: macromolecule mediated synthesis of amorphous germania structures", *Polymer*, 2005, **46**, 4474-4479.

[21] M.B. Dickerson, R.R. Naik, M.O. Stone, Y. Cai and K.H. Sandhage, "Identification of peptides that promote the rapid precipitation of germania nanoparticle networks via use of a peptide display library", *Chem. Commun.*, 2004, 1776-1777.

[22] M.T. Klem, M.Young and T.Douglas, "Biomimetic magnetic nanoparticles", *Materials Today*, 2005, **8**(9), 28-37.

[23] M. Uchida, M. T. Klem, M. Allenm P. Suci, M. Flenniken, E. Gillitzer, Z. Varpness, L.O. Liepold, M. Young and T. Douglas, "Biological containers: Protein cages as multifunctional nanoplatforms", *Adv. Mater.*, 2007, **19**, 1025-1042.

[24] M. Okuda, Y. Suzumoto, K. Iwahori, S. Kang, M. Uchida, T. Douglas and I. Yamashita, "Bio-templated CdSe nanoparticle synthesis in a cage shaped protein, Listeria-Dps, and their two dimensional ordered array self-assembly", *Chem. Commun*., 2010, **46,** 8797-8799.

[25] G. Ahmad, M. B. Dickerson, Y. Cai, S. E. Jones, E.M. Ernst, J.P. Vernon, M.S. Haluska, Y. Fang, J. Wang, G. Subramanyam, R.R. Naik and K.H. Sandhage, "Rapid

bioenabled formation of ferroelectric $BaTiO_3$ at room temperature from an aqueous salt solution at near neutral pH", *J. Am. Chem. Soc.* , 2008, **130**, 4-5

[26] J.L. Sumerel, W. Yang, D. Kisailus, J.C. Weaver, J. H. Choi and D.E. Morse, "Biocatalytically templated synthesis of titanium dioxide", *Chem. Mater.*, 2003, **15**, 4804.

[27] S.L. Sewell and D.W. Wright, "Biomimetic synthesis of titanium dioxide utilizing the R5 peptide derived from Cylindrotheca fusiformis", *Chem. Mater.*, 2006, **18**, 3108.

[28] H.R. Luckarift, M.B. Dickerson, K.H. Sandhage and J.C. Spain, "Rapid, room-temperature synthesis of antibacterial bionanocomposites of lysozyme with amorphous silica or titania", *Small*, 2006, **2**, 640.

[29] K.E. Cole and A.M. Valentine, "Spermidine and spermine catalyze the formation of nanostructured titanium oxide", *Biomacromolecule*s, 2007, **8**, 1641.

[30] T. Shiomi, T. Tsunoda, A. Kawai, F. Mizukami and K. Sakaguchi, "Biomimetic synthesis of lysozyme-silica hybrid hollow particles using sonochemical treatment: Influence of pH and lysozyme concentration on morphology", *Chem. Mater.*, 2007, **19**, 4486.

[31] J.J. Yuan and R.H. Jin, "Multiply shaped silica mediated by aggregates of linear poly(ethyleneimine)", *Adv. Mater.*, 2005, **17**, 885.

[32] R.H. Jin and J.J. Yuan, "Shaped silicas transcribed from aggregates of four-armed star polyethyleneimine with a benzene core", *Chem. Mater.*, 2006, **18**, 3390.

[33] K.M. Roth, Y. Zhou, W.J. Yang and D.E. Morse, "Bifunctional small molecules are biomimetic catalysts for silica synthesis at neutral pH", *J. Am. Chem. Soc.*, 2005, **127**, 325.

[34] D. Belton, G. Paine, S. V. Patwardhan and C. C. Perry, "Towards an understanding of (bio)silicification: the role of amino acids and lysine oligomers in silicification", *J. Mater. Chem.*, 2004, **14**, 2231.

[35] D. Belton, S. V. Patwardhan and C. C. Perry, "Putrescine homologues control silica morphogenesis by electrostatic interactions and the hydrophobic effect", *Chem. Commun*., 2005, 3475.

[36] M.B. Dickerson, K.H. Sandhage and R.R. Naik, "Protein- and Peptide-Directed Syntheses of Inorganic Materials", *Chem. Rev.*, 2008, **108**, 4935.

[37] Y. Fang, Q. Wu, M.B. Dickerson, Y. Cai, S. Shian, J.D. Berrigan, N. Poulsen, N. Kröger, and K.H. Sandhage, "Protein-Mediated Layer-by-Layer Syntheses of Freestanding Microscale Titania Structures with Biologically Assembled 3-D Morphologies", *Chem. Mater*., 2009, **21**, 5704

[38] Y. Jiang, D. Yang, L. Zhang, L. Li, Q. Sun, Y. Zhang, J. Li, , and Z. Jiang, "Biomimetic synthesis of titania nanoparticles induced by protamine", *Dalton Trans*, 2008, **37**, 4165.

[39] Y. Zhang, H. Wu, J. Li, Y. Jiang, Y. Jiang, and Z. Jiang, "Protamine-templated biomimetic hybrid capsules: Efficient and stable carrier for enzyme encapsulation", *Chem. Mater.*, 2008, **20**, 1041.

[40] Y. Jiang, Q. Sun, Z. Jiang, L. Zhang, J. Li, L. Li, and X. Sun, "The improved stability of enzyme encapsulated in biomimetic titania particles", *Mater. Sci. and Eng. C* , 2009, **29**, 328.

[41] Y. Jiang, D. ang, L. Zhang, Q. Sun, X. Sun, J. Li, and Z. Jiang, "Preparation of Protamine-Titania Microcapsules Through Synergy Between Layer-by-Layer Assembly and Biomimetic Mineralization", *Adv. Funct. Mater.*, 2009, **19**, 150.

[42] J. Li, Z. Jiang, H. Wu, L. Zhang, L. Long, and Y. Jiang, "Constructing inorganic shell onto LBL microcapsule through biomimetic mineralization: A novel and facile method for fabrication of microbioreactors", *Soft Matter*, 2010, **6**, 542.

[43] L. Zhang, Y. Jiang, J. Shi, X. Sun, J. Li, and Z. Jiang, , "Biomimetic polymer-inorganic hybrid microcapsules for yeast alcohol dehydrogenase encapsulation", *Reac. & Funct. Polym.*, 2008, **68**, 1507.

[44] Y. Zhang, H. Wu, L. Li, J. Li, Z. Jiang, Y. Jiang, and Y. Chen, "Enzymatic conversion of Baicalin into Baicalein by beta-glucuronidase encapsulated in biomimetic core-shell structured hybrid capsules", *J. Molec. Catal. B: Enzym.*, 2009, **57**, 130.

[45] J.D. Berrigan, T.S. Kang, Y. Cai, J.R. Deneault, M.F. Durstock, and K.H. Sandhage, "Protein-Enabled Layer-by-Layer Syntheses of Aligned, Porous-Wall, High-Aspect-Ratio TiO2 Nanotube Arrays*Adv. Funct. Mater.*, 2011, **21**, 1693.

[46] J. D. Berrigan, , Ph.D thesis, "Biological and Inorganic Syntheses of Nanostructured Energy-harvesting Electrodes", *Georgia Institute of Technology*, May 2012, 81.

[47] A.V. Zholnin and V.N. Podchainova, "Complexing of Ti(IV) with lactic acid" *Zhur. neorg. Khim.*, 1971, **16**, 1162.

[48] A.V. Zholnin, "Complexing of Ti(IV) with citric acid", *Zhur. neorg. Khim.*, 1971, **16**, 1010.

CHAPTER 3: LAYER-BY-LAYER BIO-INSPIRED FBABRICATION OF POROUS TIO_2 NANO-FILM COATINGS WITH CONTROLLED PORE SIZE ON MICROSPHERE RESONATORS

3.1 SUMMARY

A novel coating method, which can provide uniform pores in thin films based on the established protamine-enabled layer-by-layer deposition process, was developed. This process has been demonstrated on Si wafter substrates and glass microsphere resonators. Carboxylated polystyrene spheres with different sizes (26 nm and 110 nm in diameter) were used in this process to create pores.

SEM images of the coatings showed that the TiO_2 coatings on both Si wafer substrates and glass microsphere resonators fabricated by this novel layer-by-layer method were continuous, uniform, conformal, and porous. QCM-D and AFM thickness analyses indicated that this novel coating method exhibited an exponential deposition behavior, as the established protamine-enabled layer-by-layer deposition proces. However, the use of carboxylated polystyrene spheres resulted in a much higher frequency change than for the original protamine method.

A porous TiO_2-coated glass microsphere resonators was loaded with a green fluorescence protein, bfloGFPal. Confocal fluorescence microscopy revealed a high degree of loading of this green fluorescence protein.

This method can be extended to provide highly-porous coatings of other functional materials than TiO_2, such as ZrO_2 and HfO_2, that can be generated by the use of other water-soluble salts described in the previous chapter.

3.2 INTRODUCTION

3.2.1 Introduction to Electrostatic Layer-By-Layer self-assembly coating method

The ability to construct thin films on a variety of surfaces has multiple applications. For example, coatings on medical devices can improve biocompatibility, reduce the immunological response, and deliver a drug locally.[3,6,10] It is thus useful to find a method to coat thin films with required properties on a variety of surfaces. Currently-available thin film methods include spin coating and solution casting, thermal deposition, polyion layer-by-layer assembly, chemical self-assembly, the Langmuir-Blodgett technique, and free-standing films. The optimal combination of molecular order and stability of films determines the practical usefulness of these technologies[1–6]

A primary advantage of the electrostatic layer-by-layer self-assembly technique is its ability to coat thin films with ordered structure and nanometer thickness on supports of various shapes and sizes. Thus, during recent years, it has been applied by researchers to micropatterning[7–9], nanobioreactors[10,11], artificial cells[12], drug delivery systems[13-15], and electronic devices[16,17]. The LbL technique is based on alternate adsorption of oppositely charged materials, such as linear polycations and polyanions. Multilayers of materials can be assembled on two-dimensional (2-D) supports of any area (slides, silicon wafers, plastic surfaces) and on three-dimensional (3-D) micro/nano-templates (colloidal particles, such as latex, or cells). Charged materials, including linear polyelectrolytes (synthetic and natural), enzymes, antibodies, viruses and inorganic nanoparticles have been used in 2-D and 3-D nanoassembly processes[1–24]. The architecture of the resulting film can be designed with nanometer precision (in cross-section) to meet different

requirements, such as thickness, biocompatibility, controlled permeability, targeting, and optical or magnetic properties.

The assembly procedure is briefly shown in **Fig. 3.1**. A substrate with negative surface charge is incubated in the solution containing the cationic polyelectrolytes, and a layer of polycation is adsorbed (step 1). Because the adsorption is carried out at a relatively high concentration of polyelectrolytes, a number of ionic groups remain exposed at the interface with the solution, and thus the surface charge is effectively reversed. The reversed surface charge prevents further polyion adsorption. The substrates are then rinsed with pure water to remove excess free polyions. The surface is then immersed in a solution of anionic polyelectrolytes (step 2). Again, a layer is adsorbed, but now the original surface charge (negative) is restored and the surface is ready for further assembly (step 3). These two steps are repeated alternately until a layer of the desired thickness is obtained.

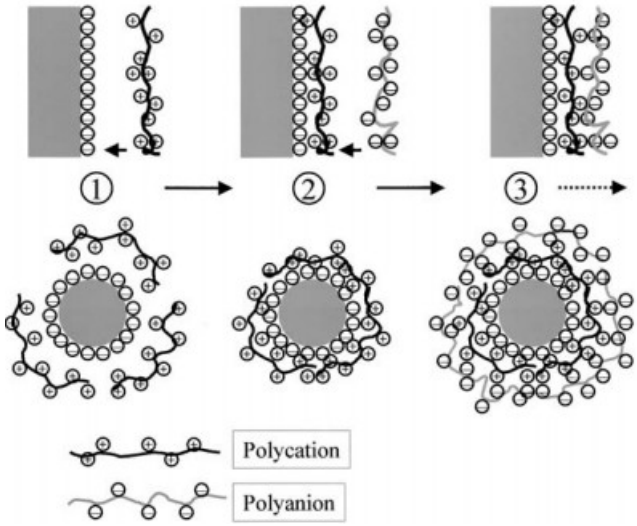

Figure 3.1: The procedure of electrostatic layer-by-layer self-assembly on 2-D substrates and 3-D micro/nanotemplates.

From the introduction part in Chapter 2 of this thesis, it can be seen many materials scientists have already applied this layer-by-layer self-assembly method in the biomineralization field. The mechanism of peptide-enabled layer-by-layer fabrication of functional mineral oxide thin films was illustrated in Figure 2.1.

Y. Fang, et al.[25] and J. D. Berrigan, et al[26] from the Sandhage group has done appreciable work on the protamine-enabled layer-by-layer coating of TiO_2 on different substrates, such as diatoms, through-pore anodic aluminum oxide templates (TP-AAO), etc. From J. D. Berrigan's work illustrated in his Ph.D dissertation, the average pore size of the TiO_2 coating by this protamine method is very low. The pores in these coatings are not big enough to be utilized for certain engineering purposes, such as dye loading. Thus, a novel protamine/polystyrene-sphere coating method was conceived by Dr. Yunshu Zhang from the Sandhage research group and developed by this author. The scheme of this coating method is illustrated in **Fig. 3.2**.

The key step of this revised protamine-enabled layer-by-layer deposition process is bringing carboxylated polystyrene spheres into the coating process. These carboxylated polystyrene spheres are commercially-available polymers with highly negatively charges and very uniform size. These polystyrene spheres can possess different uniform sizes with different molecular weight. When the protamine-absorbed substrate is exposed to the negatively-charged polystyrene spheres, the substrate surface became loaded with polystyrene spheres, which changes the charges on the substrate surface to negative. By exposing this negatively-charged substrate again to the protamine solution, another layer of protamine molecules bind to the surface, which then can precipitate the precursors for functional mineral oxides. After repeating the coating process for the desired number of

cycles, the coating can be fired in oven under proper conditions, to remove all the protamine molecules and polystyrene spheres, thus creating uniform pores of the same size (similar to that of the polystyrene spheres in the unfired coating).

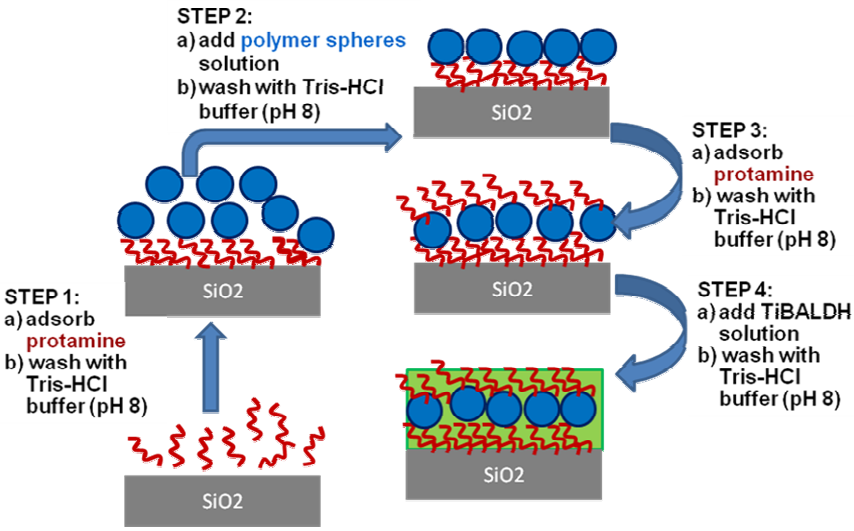

Figure 3.2: The protamine/polystyrene sphere-enabled Layer-by-layer deposition of TiO-bearing coatings

3.2.2 Introduction to porous materials

Porous solids are of scientific and technological interest because of their ability to interact with atoms, ions and molecules not only at their surfaces, but throughout the bulk of the material[28-34]. According to the IUPAC definition, porous materials are divided into three classes;microporous (pore size < 2 nm), mesoporous (2 - 50 nm), and macroporous (>50 nm) materials[35]. Many kinds of porous materials, such as pillared clays, carbon nanotubes and other related porous materials have been extensively described in the literature[36-38,43].

Well-known members of the microporous class are the zeolites, which provide excellent catalytic properties by virtue of their crystalline aluminosilicate network.

However, their applications are limited by the relatively small pore openings. Therefore, pore enlargement has been one of the main aspects in zeolite chemistry research.[39-42] Larger pores are present in porous glasses and porous gels, which were known as mesoporous materials at the time of the discovery of MCM-41.[44] The discovery of ordered mesoporous solids of the MCM-41 type and related materials in the early 1990s has been a breakthrough in materials engineering, and since then there has been impressive progress in the development of many new mesoporous solids based on templating mechanisms related to the one used for the original MCM-41 syntheses. Depending on the syntheses conditions, the silica source or the type of surfactant used, many other mesoporous materials can be synthesized following the co-operative assembly pathway[45-47]. In addition to the co-operative pathways, the true liquid crystal templating pathway[48] and nanocasting using already-formed ordered mesoporous materials as hard templates[49,50] have been developed over the past few years.

The first-ordered mesoporous materials were prepared from ionic surfactants, such as quaternary ammonium ions. The formation of the inorganic-organic composites is based on electrostatic interactions between the positively-charged surfactants and the negatively charged silicate species in solution. Che, et al. invented a synthetic route for meso-porous silica by the use of anionic surfactants[51,52]. In their work, the negatively charged head group of the anionic surfactant, such as palmitic acid or N-lauroyl-L-glutamic acid, interacts with the positively-charged amine or ammonium groups of 3-aminopropyltrimethoxysi-lane or N-trimethyoxysilylpropyl-N,N,N-trimethylammonium, which are used as additives for co-condensation of TEOS (tetra ethyl ortho silicate).

The mesopore size of these kinds of materials is primarily controlled by the length of the alkyl chain of the surfactant used. However, the addition of auxiliary organic molecules such as aromatics[53], n-alkanes[54], or fatty acid[55] can lead to an expansion of the mesopore size. Mixing of two alkyl ammonium surfactants with different alkyl chain lengths can be used to fine-tune the pore size between those of the long and the short chain surfactants[56]. Many silica-based mesoporous materials, but those with non-silica frameworks, have been reported to be formed via these electrostatic assembly pathways.

In this work, commercially-available polystyrene spheres were utilized to create pores of sizes similar to that of the polystyrene spheres. By incorporating the polystyrene spheres in a layer-by-layer pattern in the coatings, pores were then created in the coatings after firing to pyrolyze the polystyrene spheres. The detailed mechanism for this coating method was illustrated in the introduction above. As the polystyrene spheres are commercially-available in several sizes (i.e., 26 nm, 52 nm, 110 nm, 200 nm, 400 nm diameter), coatings with different sized pores can be fabricated using this method. In this chapter, polystyrene spheres with 26 nm or 110 nm diameters were used in the coating process.

Moreover, a porous TiO_2-coated glass microsphere resonator was utilized to encapsulate a green fluorescent protein, bfloGFPal[58]. Its optical properties are to be investigated in collaboration with Dr. Robert Norwood's research group at the University of Arizona.

3.3 EXPERIMENTAL PROCEDURES

The chemicals used in these experiments are as follows: deionized (DI) water (18.2 MΩ·cm), protamine sulfate (Grade X, Sigma-Aldrich, St. Louis, MO), carboxylated polystyrene spheres (Bangs Laboratories, Fishers, IN), pH 8 Tris-HCl buffer (Alfa Aesar, Ward Hill, MA), sodium dodecyl sulfate (SDS, 99+% purity, Amresco, Solon, OH, USA), 50% w/w TiBALDH (Ti(IV) bis-ammoniumlactato-dihydroxide, Sigma-Aldrich, St. Louis, MO), Sylgard® 184 Silicone elastomer base (Dow Corning Corp., Midland, MI), Sylgard® 184 Silicone elastomer curing agent (Dow Corning Corp., Midland, MI), 98% w/w H_2SO_4 (Alfa Aesar, Ward Hill, MA), and 98% w/w H_2O_2 (Alfa Aesar, Ward Hill, MA).

3.3.1 Protamine & Polystyrene Sphere Layer-By-Layer Coating of Si Substrates

A protamine & polymer sphere LbL coating process. without the use of mineral oxide precursors, was first evaluated to determine the feasibility of the desired coating method.*

Firstly, the silica wafer substrate was incubated in a 5 mg/mL protamine solution in pH 8.0 Tris-HCl buffer for 10 min. After rinsing with this buffer for 3 times, the substrate was exposed to a suspension (1 mg/mL) of polystyrene spheres (110 nm diameter) for 10 min, followed by rinsing in the buffer 3 times. Three different such Si wafer substrate samples were prepared with 1, 2, or 3 coating cycles.

*: This work was conducted by Dr. Yunshu Zhang in the Sandhage group.

3.3.2 Comparison of the Protamine/polystyrene sphere-Enabled TiO_2 Deposition Process with Protamine-Enabled TiO_2 deposition Process by Quartz Crystal Microbalance analysis

Comparison of the TiO_2 deposition behavior of the protamine-enabled process with that of the protamine/polystyrene sphere-enabled process was investigated with a quartz crystal microbalance with simultaneous dissipation monitoring (QCM-D, Q-sense E1 system, Biolin Scientific, Inc., Vastra Frolunda, Sweden). Standard gold-coated quartz sensors were coated with a thin layer (~50 nm) of SiO_2 (Model QSX303, Biolin Scientific, Inc., Vastra Frolunda, Sweden). The 1^{st}, 3^{rd}, 5^{th}, 7^{th}, 9^{th}, 11^{th} , and 13^{th} harmonics were measured simultaneously during all QCM-D experiments. The 5^{th} harmonic was selected for analysis because smaller harmonics (1^{st} and 3^{rd}) corresponded to large sensitivity areas that should be affected by the O-ring used to hold the sensor, and analyses with higher harmonics (11^{th} and 13^{th}) became less sensitive with thicker coatings.

All sensors were cleaned by 10 min. UV-ozone treatment (UV/Ozone ProCleaner, Bioforce Nanoscience, Inc., Ames, IA, USA) followed by incubation for 30 min. in a 2% v/v sodium dodecyl sulfate solution. The sensors were rinsed thoroughly with water, dried under nitrogen flow at room temperature for 5 min, and then cleaned by UV-ozone treatment for 10 min. QCM-D analysis was used over five deposition cycles at a solution flow rate of 0.1 mL/min and 22 ℃.

For protamine-mediated TiO_2 deposition, the process for each cycle was as follows: 1) exposure to protamine (100 ug/ml in pH 8 100 mM Tris-HCl buffer) for 10 min.; 2) buffer (pH 8 100 mM Tris-HCl) rinse for 5 min.; 3) exposure to TiBALDH (5 mM in pH 8 100 mM Tris-HCl buffer) for various time according to the number of cycles,

and 4) buffer (pH 8 100mM Tris-HCl) rinse for 5 min. The TiBALDH exposure time varied for each cycle due to changes in reaction kinetics, and TiBALDH flow continued until the resonance frequency change plateaued (i.e., until ΔF varied less than 1 Hz per min.), which indicated that the sensor surface had effectively completed the reaction of TiBALDH with the deposited protamine.

For protamine/polystyrene-spheres (26 nm)-mediated TiO_2 deposition, the process was conducted as follows: 1) exposure to protamine (100 ug/ml in pH 8 100 mM Tris-HCl buffer) for 10 min., 2) exposure to buffer (pH 8 100 mM Tris-HCl) rinse for 5 min.; 3) exposure to a 26 nm polystyrene spheres solution (100 ug/ml in pH 8 100 mM Tris-HCl buffer) for 10 min., 4) exposure to a buffer (pH 8 100 mM Tris-HCl) rinse for 5 min.; 5) exposure to protamine (100 ug/ml in pH 8 100 mM Tris-HCl buffer) for 10 min., 6) exposure to a buffer (pH 8 100 mM Tris-HCl) rinse for 5 min.; 7) exposure to TiBALDH (5 mM in pH 8 100 mM Tris-HCl buffer) for various times according to the number of cycles, and 8) exposure to a buffer (pH 8 100 mM Tris-HCl) rinse for 5 min; TiBALDH exposure time varied for each cycle due to changes in reaction kinetics, and TiBALDH flow continued until the resonance frequency change plateaued (i.e., ΔF varied less than 1 Hz per min.), which indicated that the sensor surface had effectively completed the reaction of TiBALDH with the deposited protamine.

For protamine/polystyrene-sphere (110 nm)-mediated TiO_2 deposition, the procedure for each cycle was exactly the same as that for the 26 nm polystyrene sphere method (except that the 26 nm polystyrene sphere suspension was replaced with the 110 nm polystyrene spheres suspension of the same sphere concentration).

3.3.3 Layer-By-Layer Coatings of Porous TiO_2 on Si Wafers and Glass Microsphere Resonators with the Protamine/Polystyrene Sphere Method

(1): Fabrication of Porous Ti-O-bearing Coatings on Si wafers

Ti-O-bearing films were deposited onto silicon wafer substrates (Wafernet, Inc., San Jose, CA, USA) that had been incubated in piranha solution (9M H_2SO_4 and 3M H_2O_2 in H_2O) for 30 min. After rinsing with a large amount of water, the wafers were then rinsed in ethanol, and dried with flowing nitrogen at room temperature for 5 min. The wafers were then cleaned by rinsing in ethanol followed by water, and dried with flowing nitrogen at room temperature for 5 min. Next the wafers were cut into 1.7 cm by 0.7 cm pieces for coating.

Prior to deposition, the Si substrates were incubated in a 100 mM pH 8 Tris-HCl buffer solution for at least 15 min to allow the surface to equilibrate with this this solution. For each cycle, the coating procedure was as follows: 1) the silica wafers were incubated in a 5 mg/mL protamine sulfate solution in the 100 mM pH 8 Tris-HCl buffer for 10 min. (to allow for protamine binding to the silica surface); 2) the protamine-treated substrates were rinsed three times with the Tris-HCl buffer, and then incubated in a 100 ug/ml suspension of 26 nm carboxylated polystyrene spheres (PS) for 10 min (to let the PS microspheres attach to the protamine-binding surface of the silica wafers); 3) after rinsing in buffer 3 times, the substrates were incubated in the protamine solution again for 10 min (to allow for protamine binding to the PS-treated surface), followed by rinsing in buffer for 3 times; 4) finally, the substrates were exposed with a freshly-prepared solution of 5 mM TiBALDH for 10 min. By repeating such deposition cycles, *n* number of layers were deposited. Each specimen was cut in half lengthwise and heated to 500°C in a tube

furnace (Lindberg / Blue M, NC USA) at 1.5°C/min for 4 h (AutoFire® Controller, Orton Ceramic Foundation, OH, USA outfitted with a k-type thermocouple, OMEGA Engineering, Inc., CT, USA) in air to allow for organic pyrolysis of the protamine for subsequent inorganic film thickness characterization after heat treatment.

By substituting the 26 nm diameter polystyrene sphere suspension with 110 nm diameter polystyrene sphere suspension, another batch of TiO_2-bearing Si wafers were coated with the same process.

(2): Porous Ti-O-bearing Coatings on GMRs (Glass Microsphere Resonators)

In order to allow for a high degree of loading of organic luminescent material onto the surfaces of GMRs, conformal porous TiO_2 coatings with different pore sizes were applied to such GMRs via a LbL protamine/polystyrene-sphere-enabled deposition process. The GMRs, obtained from the group of Pro. Robert Norwood (University of Arizona), were exposed to a Piranha solution (9 M H_2SO_4 and 3 M H_2O_2 in H_2O) for 2 hours. After rinsing several times with DI water, the GMRs were coated with porous TiO_2 via the protamine/polystyrene-sphere method using 2, 4, or 6 deposition cycles.

The coating procedures for protamine/polystyrene-sphere (26 nm & 110 nm)-enabled deposition on GMRs were the same as for Si wafers illustrated above in **Section 3.3.3.1**. The only difference was that, to prevent the GMRs' surface contacting with the walls of the coating template (that would make the coatings on the GMR surface uneven and have cracks with higher cycles), the GMRs (which were located at the ends of fibers) were attached to cardboard which can stand above the well of the coating plates. The tip GMRs could then be immersed in the coating solution without contacting the walls of the coating plates. This specially-designed apparatus is shown below in **Fig. 3.3.**

A)

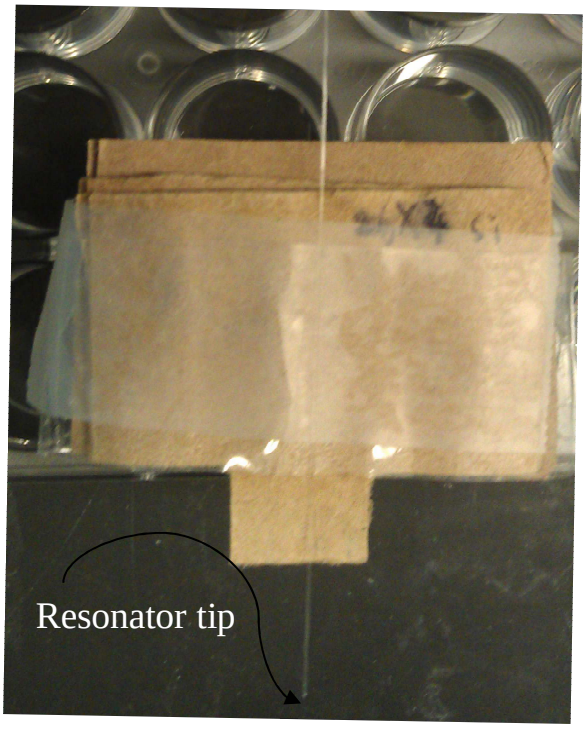

B)

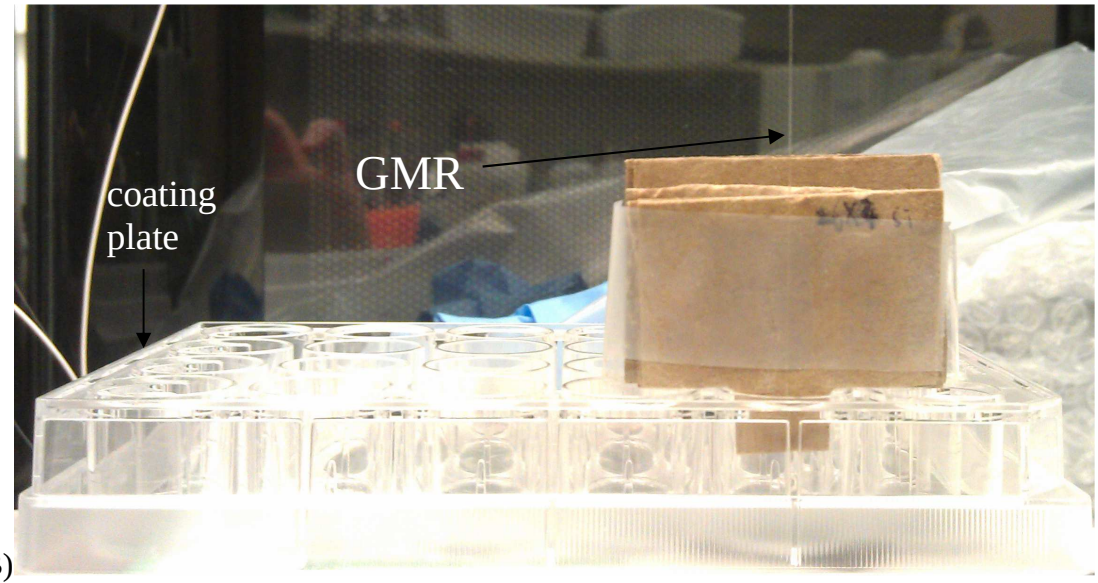

Figure 3.3: Coating apparatus for GMR samples: A) GMR (located at the end of a glass fiber) attached to a cardboard support; B) GMR attached to cardboard standing above the well of the coating plates.

3.3.4 Atomic Force Microscopy Characterization

Atomic force microscopy (AFM, Digital Instruments Nanoscope@ III, Tonawanda, NY, USA) was performed on protamine/polystyrene sphere (26 nm and 110 nm in diameters)-derived films before and after the 500℃ heat treatment for 4 h in air (1.5℃/min ramp rate) on silicon wafers after *n* number of deposition cycles (where *n* = 2, 4, 6). The measurements were conducted in tapping-mode using 10 nm radius-of-curvature general purpose probes (Mikromasch AFM NSC36, Mikromasch USA, San Jose, CA, USA) with a spring constant of 0.6 N/m and a resonant frequency of 75 Hz. Half of the Si wafer surface was masked prior to deposition using a silicone elastomer (Sylgard 184, Dow Corning, Co., Midland, MI, USA). The procedure to coat the silicone elastomer was as follows: 1) the base and curing agent were thoroughly mixed together in one container in a ratio of 10 parts base to one part curing agent, by weight; 2) the mixture was gently agitated to reduce the amount of air introduced; 3) the mixture was allowed to set for 30 min before pouring; 4) the mixture was poured onto a Si wafer surface and then heated to 60 ℃ for 5 hrs. A half-surface-coated Si wafer was obtain by peeling the elastomer coating off half of the Si wafer surface.

After deposition was completed, the elastomer mask was peeled off the surface, and 10 thickness measurements were conducted across the coated/uncoated boundary with a scan area of 10 μm by 20 μm defined within the Nanoscope Analysis software V1.4r1 (Veeco Instruments, Plainview, NY, USA).

Topographical images of the coated area, on as-coated and heat treated films, were obtained over a 15 μm by 15 μm area. The images were plane-leveled and the root-

mean square roughness of the films was measured using Nanoscope Analysis software over five different 5 μm by 5 μm areas.

3.3.5 SEM Characterization

Scanning electron microscopy was conducted with a field emission scanning electron microscope (Leo 1530 FEG SEM, Carl Zeiss SMT Ltd., Cambridge, UK) equipped with an energy dispersive X-ray spectrometer (INCA EDS, Oxford Instruments, Bucks, UK).

The samples characterized by SEM were as follows: 1) the Si wafer substrates coated by only protamine & polymer spheres without the use of mineral oxide precursors for 1, 2, or 3 cycles; 2) Si wafters coated with TiO_2 by protamine/polystyrene-sphere (both 26 nm and 110 nm)-enabled deposition using 4 cycles after firing at 500℃ for 4 hrs in air; 3) glass microsphere resonators coated with TiO_2 by the protamine/polystyrene-sphere (both 26 nm and 110 nm)-enabled process using 4 deposition cycles after firing at 500℃ for 4 hrs in air.

3.3.6 Loading and Characterization of a Green Fluorescent Protein bfloGFPa into the Porous TiO_2-Coated Microsphere Resonators

The glass microsphere resonators coated with porous TiO_2, by the protamine/polystyrene-sphere (26 nm in diameter)-enabled process for 4 cycles after firing at 500℃ for 4 hrs in air, were incubated in a solution of green fluorescent protein, which was obtained from the cordate Branchiostoma florisae (identified by the Deheyn group[58]). Exposure to this His-bfloGFPal solution in 100 mM phosphate-citrate buffer (pH 6.0) was followed with extensive rinsing with the phosphate-citrate buffer.

Confocal fluorescence microscopic analyses were conducted on the TiO_2/bfloGFPal-coated glass microsphere resonator with a UV confocal microscope (LSM 510, Carl Zeiss MicroImaging, LLC, Thornwood, NY USA). Fluorescence imaging was obtained with the use of 488 nm (30 mW Ar-ion) laser excitation.*

*: This work was conducted by Dr. Yunnan Fang in the Sandhage group.

3.4 RESULTS AND DISCUSSION

3.4.1 Protamine & Polystyrene Spheres Layer-By-Layer Coatings on Silica Wafer

A protamine/polystyrene sphere LbL coating process without the use of mineral oxide precursors was conducted on Si wafers to determine the feasibility of the desired coating method. The SEM images of 1-, 2-, and 3-cycle-coated Si wafers by protamine and polystyrene spheres (110 nm in diameter) are shown in **Fig. 3.4**.

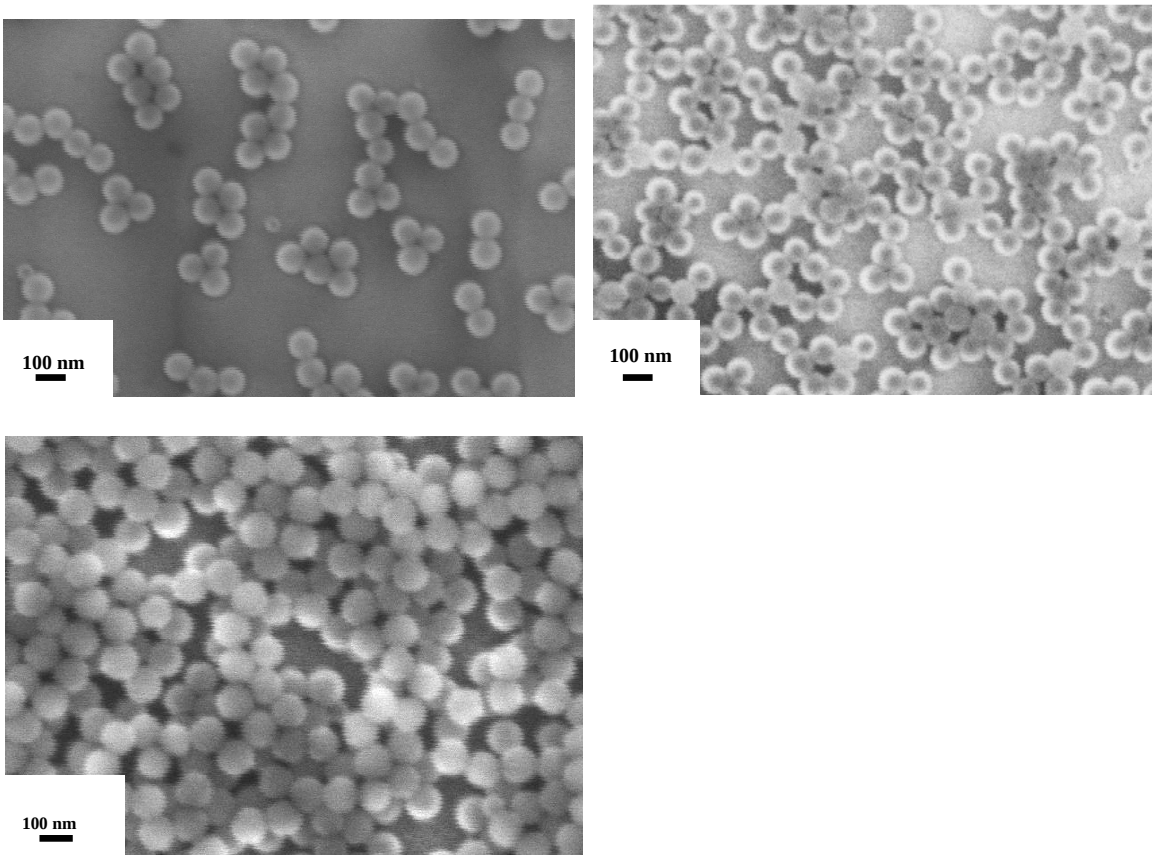

Figure 3.4: SEM images of protamine & polystyrene sphere (110 nm)-coated Si wafer surfaces after 1 (left above), 2 (right above), and 3 deposition cycles (left below).

It can be seen, from **Fig. 3.4** that, the Si wafer surface was increasingly covered from 1 to 3 cycles, which demonstrates the layer-by-layer nature of this coating process.

3.4.2 Comparison of the Protamine/polystyrene sphere-enabled TiO_2 Deposition vs. protamine-enabled TiO_2 deposition by Quartz Crystal Microbalance

Comparison of the established protamine-enabled LbL deposition process with the novel protamine/polystyrene sphere-enabled LbL coating method was made with a quartz crystal microbalance analysis. The evolution of $-\Delta F$ from QCM-D results of the protamine/polystyrene sphere (26 nm & 110 nm)-enabled deposition process versus the number of deposition cycles is presented in **Fig. 3.5 & 3.6**. For protamine/polystyrene sphere (26 nm & 110 nm)-enabled deposition, the polystyrene spheres and TiBALDH incubation times varied during each cycle as shown in following Table **3.1**.

Table 3.1. Polystyrene spheres and TiBALDH incubation time used during protamine/polystyrene sphere (26 nm & 110 nm)-enabled deposition

Cycles / Time (min)	1	2	3	4	5
26 nm PS	5	10	15	20	30
TiBADLH after 26 nm PS	5	10	15	20	30
110 nm PS	5	15	25	40	60
TiBALDH after 110 nm PS	5	10	15	20	30

Owing to the measurement limitation of frequency in the quartz crystal microbalance analyses, it was conducted only to the 5^{th} coating cycle for this protamine/polystyrene sphere method.

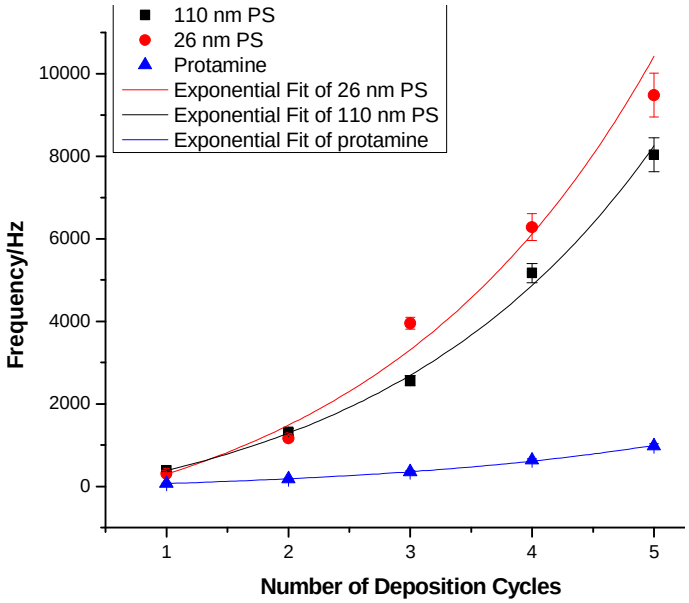

Figure 3.5: The ΔF evaluated using the 5th harmonic from QCM-D measurement of protamine/polystyrene sphere (26 nm & 110 nm)-enabled deposition and protamine-enabled deposition process vs. *n* (number of deposition cycles). Error bars represent the standard deviation recorded from two experiments. Data for cycle 1 to 5 of these 3 deposition processes were all fit using exponential equations.

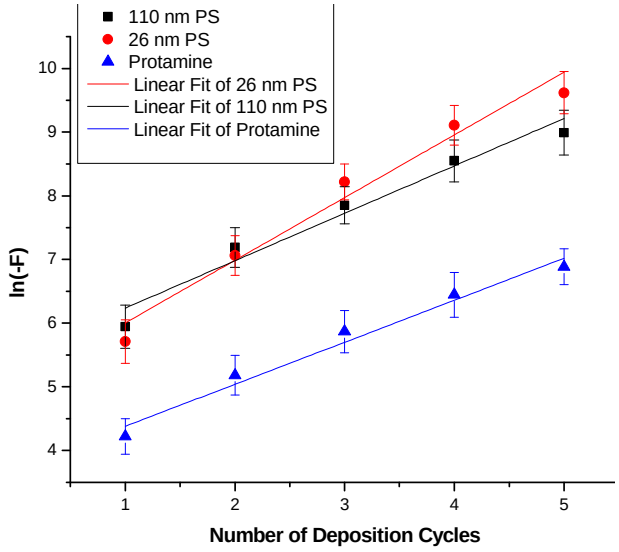

Figure 3.6: The linear dependence of ln(-ΔF) with *n* for protamine/polystyrene sphere (26 nm & 110 nm)-enabled deposition and protamine-enabled deposition from cycles 1 to 5.

For protamine/polystyrene sphere (26 nm)-enabled deposition, **Equ. 3.1** was used to fit the deposition behavior with R^2 = 0.9875. For protamine/polystyrene sphere (110 nm)-enabled deposition, **Equ. 3.2** was used to fit the deposition behavior with R^2 = 0.9943. For protamine-enabled TiBALDH deposition, the QCM-D analysis from the previous chapter was shown.

$$\Delta F = -5022+4448\exp^{(0.245*n)} \qquad (3.1)$$

$$\Delta F = -1807+1450\exp^{(0.384*n)} \qquad (3.2)$$

The linear dependence of ln(-ΔF) for 5 cycles of the protamine/polystyrene spheres (26 nm & 110 nm) enabled deposition process verified the exponential nature of the deposition process (**Fig. 3.6**). The linear fit of protamine/polystyrene sphere (26 nm) deposition behavior yielded R^2 = 0.9633, with the fitting **Equ. 3.3**. For protamine/polystyrene sphere (110 nm) deposition behavior for cycles 1 to 5 obeyed **Equ. 3.4** with R^2 = 0.9544. For protamine-enabled TiBALDH depositions, the QCM-D analysis from the previous chapter is shown.

$$\ln(-\Delta F) = 4.983 + 0.986*n \qquad (3.3)$$

$$\ln(-\Delta F) = 5.4+0.745*n \qquad (3.4)$$

From **Fig. 3.5 & 3.6**, it can be seen that the deposition amount for each cycle of the protamine/polystyrene sphere method was much higher than for the original protamine method without the incorporation of polystyrene spheres. One reason for this enhanced deposition would be that, after polystyrene spheres were attached to the protamine-saturated surface of the substrate, the roughness and surface area of the coated surface would be much higher, with a relatively large number of negative charges on the

coated surface. Hence, a much higher amount of protamine should be deposited on the surface of Si wafer, leading to much more TiO_2 deposition on the surface. The QCM-D analyses showed that, for different sizes of polystyrene spheres (i.e, 26 nm and 110 nm diameter), the difference in frequency change difference for each cycle was not large. From **Fig. 3.5** it seems that the 26 nm polystyrene sphere-coated process yielded a slightly higher frequency change than for the 110 nm polystyrene sphere process.

3.3.3 SEM Characterization of Porous TiO_2 Coatings on Silica Wafers and Microsphere Resonators Generated by the Protamine/Polystyrene Sphere Method

The SEM images in **Figs. 3.7 - 3.10** revealed the morphology of porous TiO_2 coatings on Si wafers and glass microsphere resonators. From **Fig. 3.7**, it can be seen that the TiO_2 coating on the Si wafer substrate was porous, with many pores ~ 30 nm in diameter, which were similar to the diameter of the polystyrene spheres (26 nm). Similarly, the SEM image of a TiO_2 coating generated with the protamine/polystyrene sphere (110 nm) method on Si wafer is shown in **Fig. 3.8**. The film was also highly porous with an average pore size around 92 nm, which was slightly lower than the size of 110 nm polystyrene spheres, perhaps due to the shrinkage of the pores during firing.

For the protamine/polystyrene sphere (26 nm and 110 nm)-coated glass microsphere resonators, the SEM images of the coating on the surface are shown below in **Fig. 3.9 & 3.10**. The TiO_2 coating morphology on the glass microsphere resonators was similar to that of the coated Si wafer substrates shown above. The coatings were both highly porous with the pore sizes close to the sizes of polystyrene spheres used in the coating process.

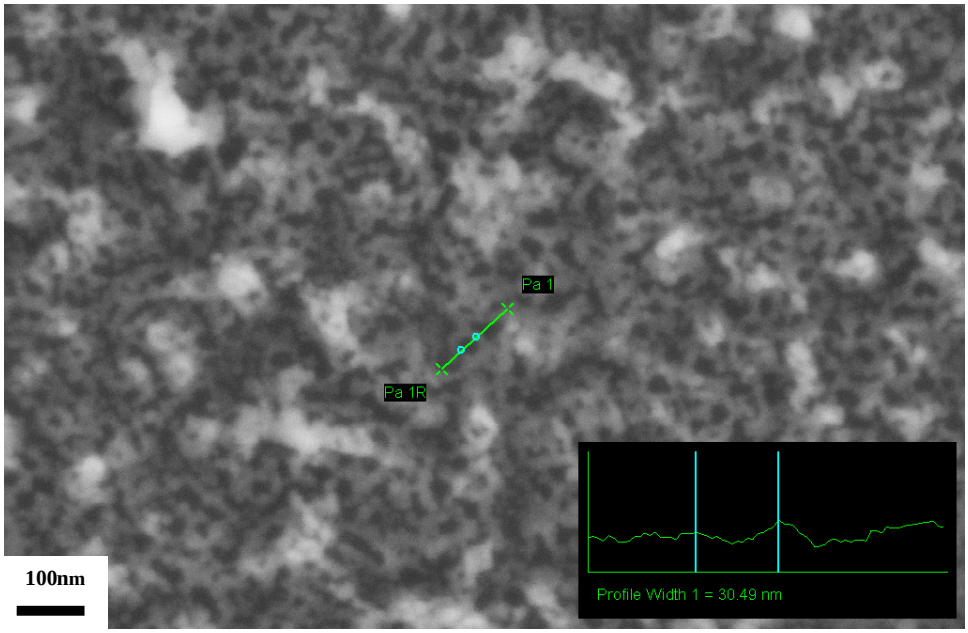

Figure 3.7: Secondary electron image of a porous TiO_2 coating generated by the protamine/polystyrene sphere (26 nm) method on a Si wafer substrate using 4 deposition cycles, after firing at 500℃ for 4 hrs in air.

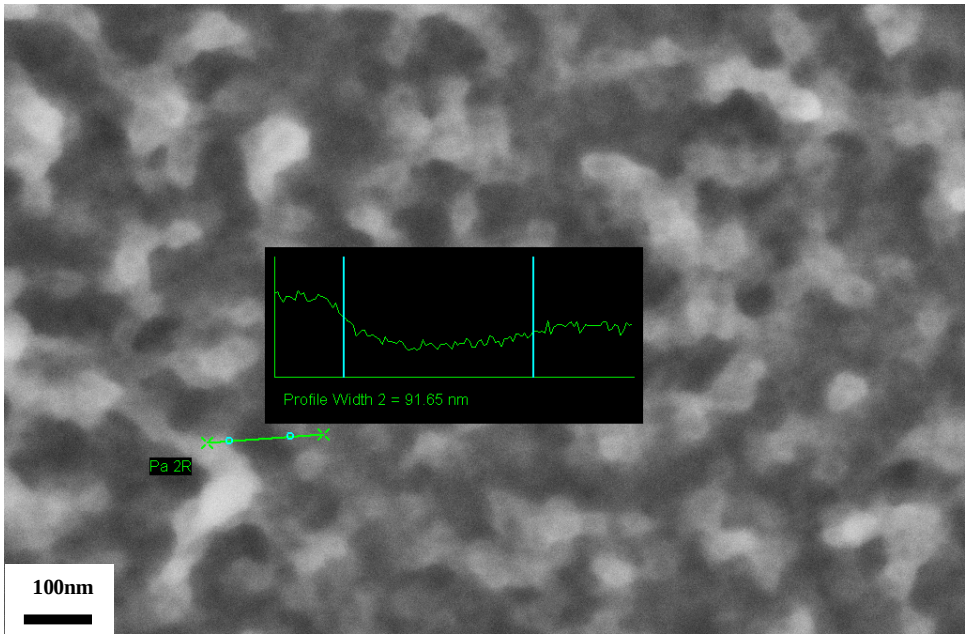

Figure 3.8: Secondary electron image of a porous TiO_2 coating generated by the protamine/polystyrene sphere (110 nm) method on a Si wafer substrate using 4 deposition cycles, after firing at 500℃ for 4 hrs in air.

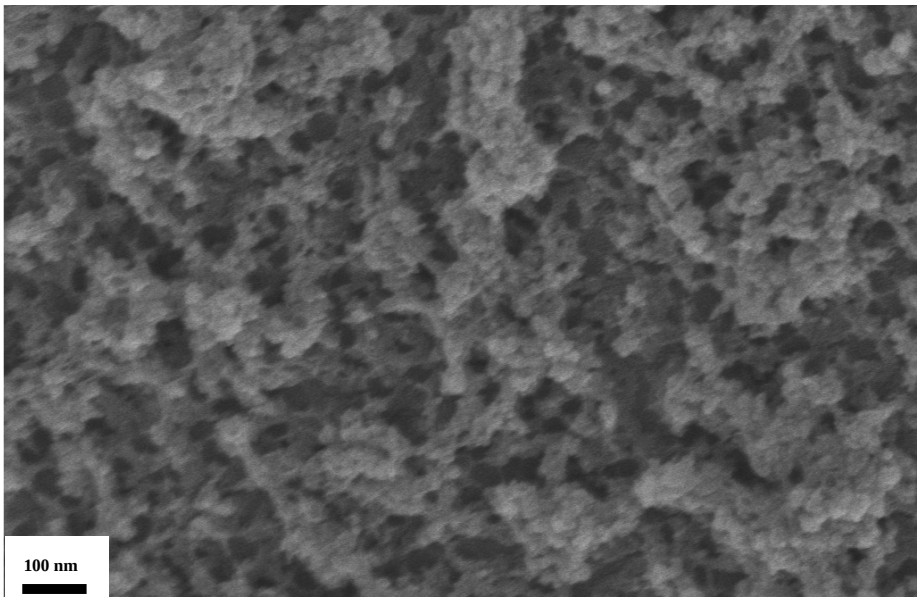

Figure 3.9: Secondary electron image of a porous TiO_2 coating generated by the protamine/polystyrene sphere (26 nm) method on a glass microsphere resonator substrate using 4 deposition cycles, after firing at 500℃ for 4 hrs in air.

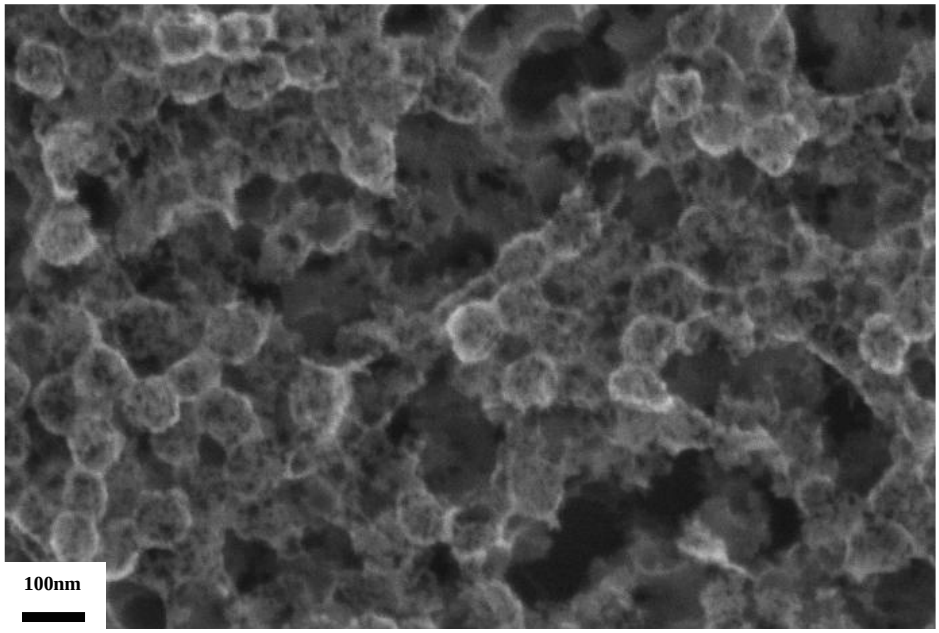

Figure 3.10: Secondary electron image of a porous TiO_2 coating generated by the protamine/polystyrene sphere (110 nm) method on a glass microsphere resonator substrate using 4 deposition cycles, after firing at 500℃ for 4 hrs in air.

The SEM images of the coatings on both Si wafers and glass microsphere resonators reveal that this novel protamine/polystyrene sphere LbL deposition method can create continuous, uniform, conformal and highly porous coatings on the substrates.

3.3.4 Atomic Force Microscopy Characterization

Ex-situ AFM thickness measurements were obtained at the boundaries between coated and uncoated regions on Si wafers to determine the dry film thickness as a function of the number of deposition cycles.

The AFM thickness results for Si wafers coated by the protamine/polystyrene spheres (26 nm and 110 nm) enabled TiO_2 deposition, both before and after firing, were shown below in **Figs. 3.11 - 3.14**.

From **Figs. 3.11 & 3.12**, it can be seen that the coating thickness vs. *n* (number of deposition cycles) of 26 nm & 110 nm polystyrene sphere-coated samples, before firing, exhibited exponential deposition behavior from cycles 1 to 6. This AFM result was consistent to the QCM-D result in the previous section. The thicknesses of polystyrene coated samples were much higher than for thin films generated by the protamine LbL method. From **Fig. 3.11**, it can be seen that the thickness of 110 nm polystyrene coated sample was slightly higher than that of the 26 nm polystyrene spheres coated sample for the same number of coating cycles, while in the QCM-D results suggested the opposite. This difference between the QCM-D and AFM analyses may indicate that the frequency change from QCM-D analysis was not exactly proportional to the thickness of the deposited material on the sensor. As mentioned in previous chapter, when the change in dissipation (ΔD) is larger than 1, the Sauerbrey relation between ΔF and adsorbed mass could not be used to accurately relate ΔF to film thickness.

For protamine/polystyrene sphere (26 nm)-enabled TiO_2 deposition before firing, **Equ. 3.5** was used to fit the deposition behavior with R^2 = 0.9936. For protamine/polystyrene sphere (110 nm)-enabled TiO_2 deposition before firing, **Equ. 3.6** was used to fit the deposition behavior with R^2 = 0.9947.

$$\text{Thickness} = 47.14+17.1\exp^{(0.466*n)} \quad (3.5)$$

$$\text{Thickness} = 36.6+28.9\exp^{(0.503*n)} \quad (3.6)$$

The linear dependence of ln(*film thickness*) with *n* for the first six cycles of protamine/polystyrene sphere (26 nm & 110 nm)-enabled TiO_2 deposition before firing is shown in **Fig. 3.12**. The linear fit over cycles 1 to 6 is shown in **Equ. 3.7** with R^2=0.9565. For the 110 nm polystyrene sphere process, the fitting equation is shown in **Equ. 3.8** with R^2= 0.9837.

$$\ln(\textit{thickness}) = 3.92+ 0.413*n \quad (3.7)$$

$$\ln(\textit{thickness}) = 3.96 + 0.442*n \quad (3.8)$$

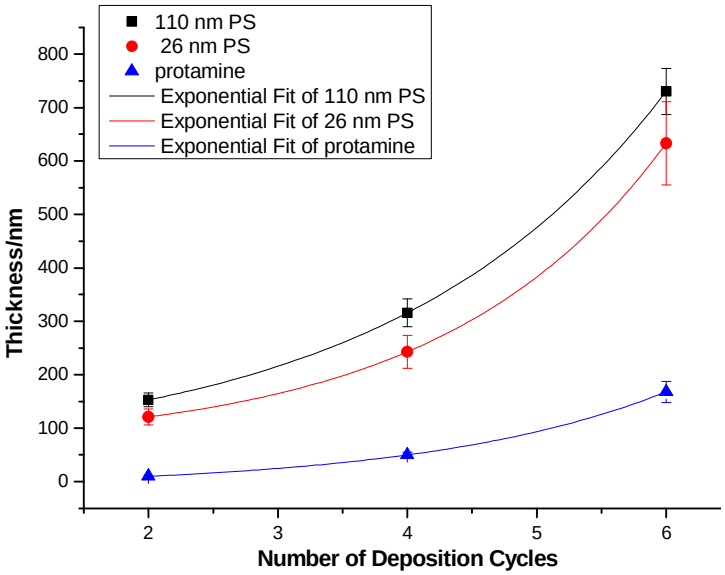

Figure 3.11: The film *thickness* from AFM measurements of protamine/polystyrene sphere (26 nm & 110 nm)-enabled films and protamine-enabled films vs. *n* (number of deposition cycles) before firing. Error bars represent the standard deviation obtained from three experiments.

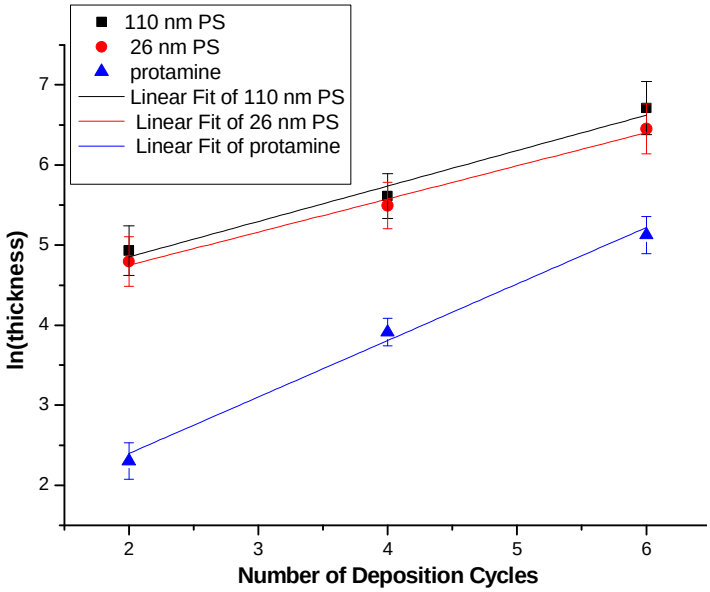

Figure 3.12: The linear dependence of ln(*film thickness*) with *n* of protamine/polystyrene sphere (26 nm & 110 nm)-enabled films and protamine-enabled films, before firing, for 2, 4, or 6 deposition cycles.

For the samples after firing, from **Figs. 3.13 & 3.14**, it can be seen that the evolution of the thickness of these coated films after firing followed the same pattern as before firing. The thicknesses of both 26 nm and 110 nm polystyrene sphere-coated samples exhibited exponential deposition behavior from cycles 1 to 6. However, the thicknesses of the samples after firing decreased greatly (by 43% to 59%) from before firing.

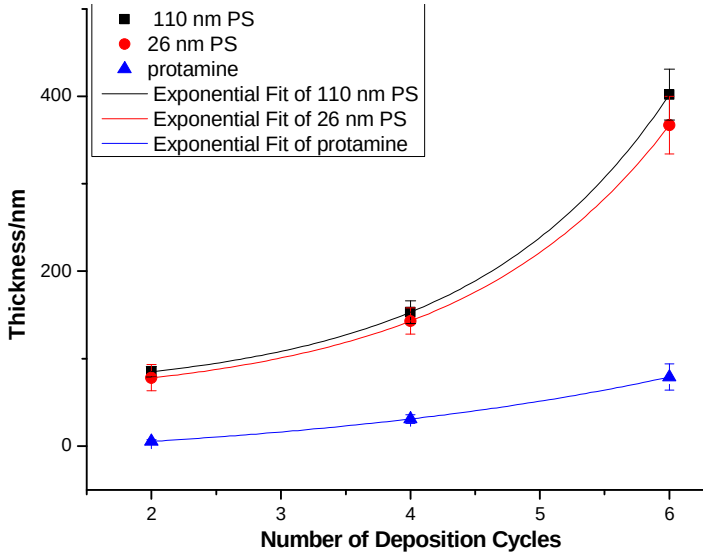

Figure 3.13: The film thickness from AFM measurements of protamine/polystyrene sphere (26 nm & 110 nm)-enabled films and protamine-enabled films vs. *n* (number of deposition cycles), after firing. Error bars represent the standard deviation obtained from three experiments.

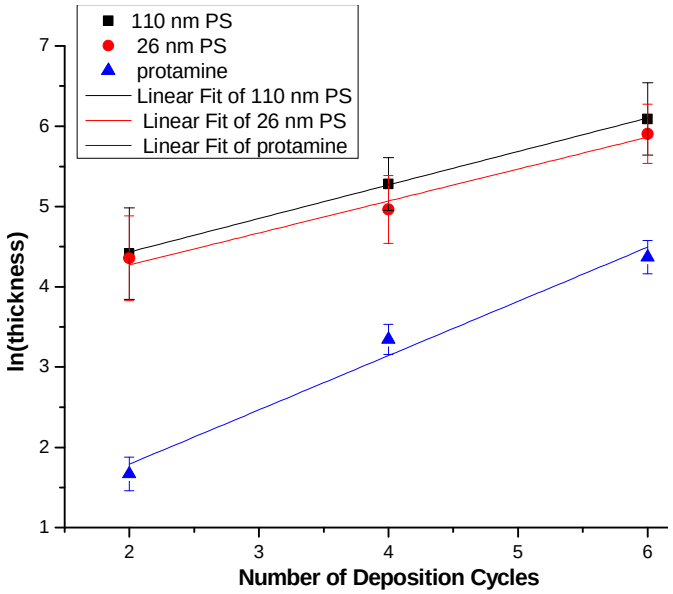

Figure 3.14: The linear dependence of ln(*film thickness*) with *n* of protamine/polystyrene sphere (26 nm & 110 nm)-enabled films and protamine-enabled films, after firing, for 2, 4, or 6 deposition cycles.

For protamine/polystyrene sphere (26 nm)-enabled TiO_2 deposition after firing, **Equ. 3.9** was used to fit the deposition behavior with R^2 = 0.9941. For protamine/polystyrene sphere (110 nm)-enabled TiO_2 deposition, after firing, **Equ. 3.10** was used to fit the deposition behavior with R^2 = 0.9897.

$$\text{Thickness} = 51.14+7.71\exp^{(0.618*n)} \qquad (3.9)$$

$$\text{Thickness} = 59.4+6.97\exp^{(0.648*n)} \qquad (3.10)$$

The linear dependence of ln(*film thickness*) with *n* for the first six cycles of protamine/polystyrene sphere (26 nm & 110 nm)-enabled TiO_2 deposition after firing is shown in **Fig. 3.14**. The linear fit of the 26 nm polystyrene sphere deposition behavior yielded to **Equ. 3.11** with R^2=0.9639. For the 110 nm polystyrene sphere method, the deposition behavior followed **Equ. 3.12** with R^2= 0.9783.

$$\ln(thickness) = 3.52 + 0.397 * n \quad (3.11)$$

$$\ln(thickness) = 3.59 + 0.417 * n \quad (3.12)$$

Overall, the AFM results of the films generated by this novel protamine/polystyrene spheres method were consistent with the QCM-D results. Both types of analyses confirmed that this method provided a much higher deposition amount than that of the original protamine method for the same number of coating cycles.

3.3.5 Loading of a Green Fluorescent Protein bfloGFPal the Porous TiO_2-Coated Microsphere Resonators

A confocal fluorescence microscopy image of a TiO_2/bfloGFPal-coated glass microsphere resonator is shown below in **Fig. 3.15**.

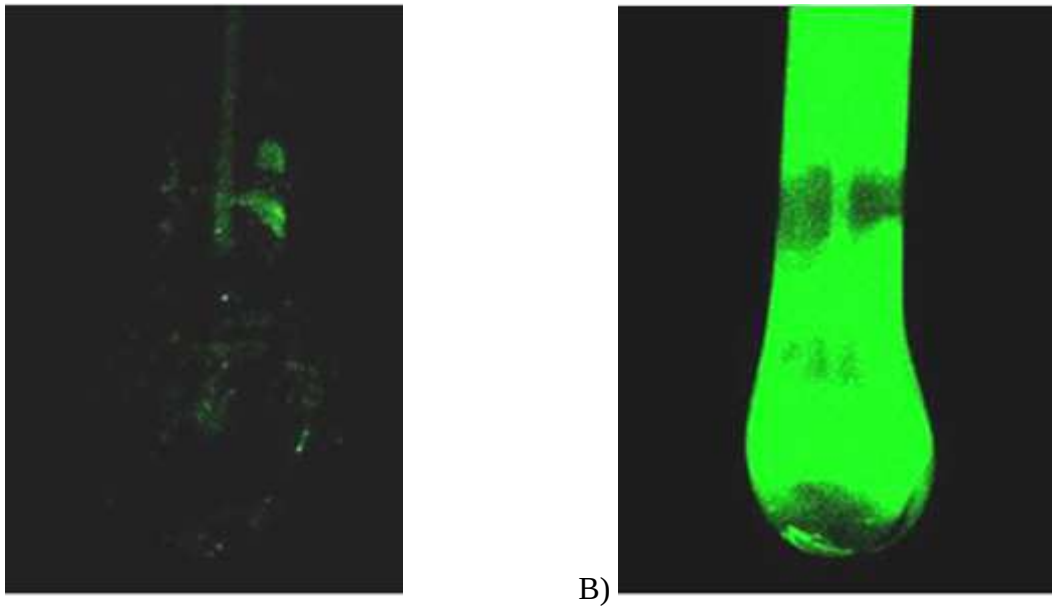

Figure 3.15: A. Confocal fluorescence microscopy image of a blank GMR coated with green fluorescent protein bfloGFPal ; B. Confocal fluorescence microscopy image of the 4-cycles protamine/polystyrene sphere (26 nm)-enabled porous TiO_2-coated GMR specimen after the loading of green fluorescent protein bfloGFPal.

From **Fig. 3.15**, it can be seen that the porous TiO_2-coated GMR could be loaded with much more green fluorescence protein bfloGFPa than for the non-TiO_2-coated GMR. This means that the porous TiO_2 coatings on GMR do help to encapsulate large protein molecules into the resonator.

3.5 SUMMARY AND OUTLOOK

A novel, low-cost, and facile modification of the established protamine-enabled layer-by-layer deposition process has been developed to deposit highly porous TiO_2 coatings on different kinds of substrates. The porosity of the resulting coatings could be finely tuned by controlling a number of parameters, such as the size of the polymer spheres, the number of layers/thickness of the coatings, and the concentration of protamine.

The SEM images of the coatings indicated that the TiO_2 coatings on both Si wafer substrates and glass microsphere resonators fabricated by this novel layer-by-layer method were continuous, uniform, and highly porous. QCM-D and AFM thickness analyses indicated that this novel coating method exhibited exponential deposition behavior as the established protamine-enabled layer-by-layer deposition process. However, the use of carboxylated polystyrene spheres resulted in a much higher amount of deposition on the substrate surfaces than for the original protamine method.

The porous TiO_2-coated glass microsphere resonator was loaded with a green fluorescence protein, bfloGFPal. Confocal fluorescence microscopy revealed a high degree of loading of this green fluorescence protein.

This method can be extended to provide highly-porous coatings of other functional materials than TiO_2, such as ZrO_2 and HfO_2, that can be generated by the use of other water-soluble salts described in the previous chapter.

3.6 REFERENCES

[1] G. Decher, “Fuzzy Nanoassemblies: Toward Layered Polymeric Multicomposites”, *Science,* 1997, **227**, 1232–1237.

[2] P. Bertrand, A. Jonas, A. Laschevsky and R. Legras, “Ultrathin polymer coatings by complexation of polyelectrolytes at interfaces: suitable materials, structure and properties *Macromol. Rapid Commun.,* 2000, **21**, 319–348.

[3] Y. Lvov and H.*M.* Möhwald, “Electrostatic layer-by-layer assembly of proteins and polyions. In Protein Architecture: Interfacial Molecular Assembly and Immobilization Biotechnology”, *Dekker*, New York, 2000, 125–167.

[4] Y. Lvov, G. Decher, and H. Möhwald, “Assembly, structural characterization, and thermal-behavior of lary-by-layer deposited ultrathin films of poly(vinyl sulfate) and poly(allylamine)”, *Langmuir*, 1993, **9**, 481–486.

[5] J.D. Mendelsohn, S. Yang, J. Hiller, A.I. Hochbaum and M.F. Rubner, “Rational design of cytophilic and cytophobic polyelectrolyte multilayer thin films”, B*iomacromolecules*, 2003, **4** , 96–106.

[6] D. Elbert, C. Herbert and J. Hubbell, “Thin polymer layers formed by polyelectrolyte multilayer techniques on biological surfaces”, *Langmuir*, 1999, **15**, 5355–5362.

[7] J. Schlenoff, S. Dubas and T. Farhat, “Sprayed polyelectrolyte multilayers”, *Langmuir*, 2000, **16,** 9968–9969.

[8] F. Hua, T. Cui and Y. Lvov, “Lithographic approach to pattern self-assembled nanoparticle multilayers”, *Langmuir*, 2002, **18**, 67123- 6715.

[9] H. Zheng, I. Lee, M. Rubner and P. Hammond, “Two component particle arrays on patterned polyelectrolyte multilayer templates”, *Adv. Mat.*, 2002, **14**, 569-572.

[10] H. Ai, Y.M. Lvov, D.K. Mills, J.S. Alexander and S.A. Jones, “Coating and selective deposition of nanofilm on silicone rubber for cell adhesion and growth”, *Cell. Biochem. Biophys.*, 2003, **38**, 103–114.

[11] Y. Lvov and F. Caruso, “Biocolloids with ordered urease multilayer shells as enzymatic reactors”, *Anal. Chem.*, 2001, **73(17)**, 4212–4217.

[12] M. Fang, P.S. Grant, M. McShane, G. Sukhorukov, V. Golub and Y. Lvov, “Magnetic bio/nanoreactor with multilayer shells of glucose oxidase and inorganic nanoparticles”, *Langmuir*, 2002, **18**, 6338–6344.

[13] H. Ai, M. Fang, S.A. Jones and Y. Lvov, “Electrostatic layer-by-layer nanoassembly on biological microtemplates: Platelets”, *Biomacromolecules*, 2002, **3**, 560–564.

[14] X. Qiu, S. Leporatti, E. Donath and H. Möhwald, “Studies on the drug release properties of polysaccharide multilayers encapsulated ibuprofen microparticles”, *Langmuir*, 2001, **17**, 5375–5380.

[15] H. Ai, S.A. Jones, M.M. de Villiers and Y. Lvov, “Nano-encapsulation of furosemide microcrystals for controlled drug release”, *J. Control. Release*, 2003, **86**, 59–68.

[16] P. Ho, J. Kim and J.H. Burroughes, “Molecular-scale interface engineering for polymer light-emitting diodes”, *Nature*, 2000, **404**, 481–484.

[17] J.K. Lee, H. Mattoussi, D. Yoo, A. Wu and M. Rubner, “Thin film light emitting heterostructures: From conjugated polymers to ruthenium complexes to inorganic nanocrystallites", *Polymer Prep.*, 1997, **38**, 351–352.

[18] M. Gao, B. Richter and S. Kirstein, “White-light electroluminescence from a self-assembled Q-CdSe/PPV multilayer structures”, *Adv. Mater.*, 1997, **9**, 802–805.

[19] Y. Lvov, A.A. Antipov, A. Mamedov, H. Möhwald and G.B. Sukhorukov, “Urease encapsulation in nanoorganized microshells”, *Nano. Lett.*, 2001, **1**, 125–128.

[20] G. Mao, Y. Tsao, M. Tirrell, H.T. Davis, V. Hessel and H. Ringsdorf, “Interactions, structure, and stability of photoreactive bolaform amphiphile multilayers”, *Langmuir*, 1995, **11**, 942–952.

[21] J. Cheung, A. Fou, and M. Rubner, “Molecular self-assembly of conducting polymers”, *Thin Solid Films*, 1994, **244**, 985–989.

[22] E. Kleinfeld, and G. Ferguson, “Stepwise formation of multilayered nanostructural films from macromolecular precursors”, *Science*, 1994, **265**, 370–373.

[23] J.A. He, L. Samuelson, L. Li, J. Kumar, and S. Tripathy, “Oriented bacteriorhodopsin/polycation multilayers by electrostatic layer-by-layer assembly”, *Langmuir*, 1998, **14**, 1674–1679.

[24] A. Ulman, “ An Introduction to Ultrathin Organic Films: From. Langmuir-Blodgett to Self-Assembly”, *Academic Press, Boston*, 1991, 401–440

[25] Y. Fang, Q. Wu, M.B. Dickerson, Y. Cai, S. Shian, J.D Berrigan, N. Poulsen, N. Kröger, and K.H. Sandhage, “Protein-Mediated Layer-by-Layer Syntheses of Freestanding Microscale Titania Structures with Biologically Assembled 3-D Morphologies”, *Chem. Mater*., 2009, **21**, 5704

[26] J.D. Berrigan, T.S. Kang, Y. Cai, J.R. Deneault, M.F. Durstock, , and K.H.

Sandhage, "Protein-Enabled Layer-by-Layer Syntheses of Aligned, Porous-Wall, High-Aspect-Ratio TiO_2 Nanotube Arrays", *Adv. Funct. Mater.*, 2011, **2**1, 1693.

[27] J.D. Berrigan, Ph.D thesis, "Biological and Inorganic Syntheses of Nanostructured

Energy-harvesting Electrodes", *Georgia Institute of Technology*, May 2012.

[28] Q. Huo, D.I. Margolese, and G.D. Stucky, "Surfactant control of phases in the synthesis of mesoporous silica-based materials", *Chem. Mater.*, 1996, **8**, 1147.

[29] Z. Luan, C.F. Cheng, W. Zhou, J. Klinowski, "Thermal-stability of structural aluminum in the mesoporous molecular-sieve MCM-41", *J. Phys. Chem.*1995, **99**, 1018 - 1024.

[30] J.S. Beck, J.C. Vartuli, W.J. Roth, M.E. Leonowicz, C.T. Kresge, K.D. Schmitt, C.T. Chu, D.H. Olson, E.W. Sheppard, S.B. McCullen, J.B. Higgins, and J.L. Schlenker, "A new family of mesoporous molecular -sieves prepared with liquid-crystal templates", *J. Am. Chem. Soc.*, 1992, **114**, 10834-10843.

[31] D.A. Loy, and K. Shea, "Bridged polysilsesquioxanes - higly porous hybrid organic-inorganic materials", *Chem. Rev.* 1995, **95**, 1431-1442

[32] C.E. Fowler, S.L. Burkett, and S. Mann, "Synthesis and characterization of ordered organo-silica-surfactant mesophases with functionalized MCM-41-type architecture", *Chem. Commun.*1997, 1769-1770.

[33] H.W. Oviatt and K.J. Shea, J. H. Small, "Alkylene-bridged silsequioxane sol-gel synthesis and xerogel characterization - molecular requirements for porosity", *Chem. Mater.* 1993, **5**, 943-950.

[34] D. Zhao, Q. Huo, J. Feng, B.F. Chmelka, and G.D. Stucky, "Nonionic triblock and star diblock copolymer and oligomeric surfactant syntheses of highly ordered, hydrothermally stable, mesoporous silica structures", *J. Am. Chem. Soc.* 1998, **120**, 6024-6036

[35] U. Ciesla, D.G. Demuth, R. Leon, P.M. Petroff, G.D. Stucky, K.K. Unger, and F. Schuth, "Surfactant contolled preparation of mesostructured transition-metal oxide compounds", *J. Chem. Soc. Chem. Commun.*, 1994, 1387.

[36] K.S. Sing, D.H. Everett, R.A. Haul, L. Moscou, R.A. Pierotti, J. Rouquerol, and T. Siemieniewska, "Reporting physisorption data for gas solid systems with special reference to the determination of surface-area and porosity", *Pure Appl. Chem.*, 1985, **57**, 603.

[37] F. DiRenzo, H. Cambon, and R. Dutartre, “A 28-year-old synthesis of micelle-templated mesoporous silica”, *Microporous Mater.*,1997, **10**, 283.

[38] S. Inagaki, Y. Fukushima, and K. Kuroda, “Synthesis of highly ordered mesoporous materials from a layered polysilicate”, *J. Chem. Soc., Chem. Commun.*, 1993, 680.

[39] S. Inagaki, A. Koiwai, N. Suzuki, Y. Fukushima, and K. Kuroda, “Syntheses of highly ordered mesoporous materials, FSM-16, derived from kanemite”, *Bull. Chem. Soc. Jpn.*, 1996, **69**, 1449.

[40] M.E. Davis, C. Saldarriaga, C. Montes, J. Garces, and C. Crowder, “A molecular-sieve with 18-membered rings”, *Nature*, 1988, **331**, 698.

[41] B.J. Schoeman, J. Sterte, and J.E. Otterstedt, “Synthesis and size tailoring of colloidal zeolite particles”, *J. Chem. Soc. Chem. Commun*., 1993, 994.

[42] A.H. Janssen, A.J. Koster, and K.P. de Jong, “Three-dimensional transmission electron microscopic observations of mesopores in eealuminated zeolite Y” *Angew. Chem. Int. Ed.*, 2001, **40**, 1102.

[43] I. Schmidt, A. Boisen, E. Gustavsson, K. Stahl, S. Pehrson, S. Dahl, A. Carlsson, and C. J.H.Jacobsen, “Carbon nanotube templated growth of mesoporous zeolite single crystals”, *Chem. Mater.*, 2001, **13**, 4416.

[44] J.S. Beck, C.T.W. Chu, I.D. Johnson, C.T. Kresge, M.E. Leonowicz, W.J. Roth, J.W. Vartuli, “Synthetic porous crystalline material, its preparation, and use”, *PCT Int. Appl.*, WO Patent 91/11390, 1991.

[45] A. Monnier, F. Schuth, Q. Huo, D. Kumar, D. Margolese, R.S. Maxwell, G. Stucky, M. Krishnamurty, P. Petroff, A. Firouzi, M. Janicke, and B. Chmelka, “Cooperative formation of inorganic-organic interfaces in the synthesis of silicate mesostructures”, *Science*, 1993, **261**, 1299.

[46] Q. Huo, D. Margolese, U. Ciesla, P. Feng, T. Gier, P. Siege, R. Leon, P.M. Petroff, U. Ciesla, F. Schuth, and G. Stucky, “Generalized synthesis of periodic surfactant inorganic composite-materials”, *Nature*, 1994, **368**, 317.

[47] Q. Huo, D. Margolese, U. Ciesla, D. Demuth, P. Feng, T. Gier, P. Siege, A. Firouzi, B. Chmelka, F. Schuth, and G. Stucky, “Organization of organic-molecules with inorganic molecular-species into nanocomposite biphase arrays”, *Chem. Mater.*, 1994, **6**, 1176.

[48] G.S. Attard, J.C. Glyde, and C.G. Goltner, “Liquid-crystalline phases as templates for the synthesis of mesoporous silica”, *Nature*, 1995, **378**, 366

[49] R. Ryoo, S.H. Joo, and S. Jun, "Synthesis of highly ordered carbon molecular sieves via template-mediated structural transformation", *J. Phys. Chem. B*, 1999, **103**, 7743

[50] A.H. Lu, W. Schmidt, A. Taguchi, B. Spliethoff, B. Tesche, and F. Schuth, "Taking Nanocasting One Step Further: Replicating CMK-3 as a Silica Material", *Angew. Chem. Int. Ed.* 2002, **41**, 3489

[51] S. Che, A.E. Garcia-Bennett, T.Yokoi, K. Sakamoto, H. Kunieda, O. Terasaki, and T. Tatsumi, "A novel anionic surfactant templating route for synthesizing mesoporous silica with unique structure", *Nature Mater.*, 2003, **2**, 801.

[52] A.E. Garcia-Bennett, O. Terasaki, S. Che, and T. Tatsumi, "Structural investigations of AMS-n mesoporous materials by transmission electron microscopy", *Chem. Mater.*, 2004, **16**, 813.

[53] M. Linden, P. Agren, S. Karlsson, P. Bussian, and H. Amenitsch, "Solubilization of oil in silicate-surfactant mesostructures", *Langmuir*, 2000, **16**, 5831.

[54] N. Ulagappan, and C.N.R. Rao, "Evidence for supramolecular organization of alkane and surfactant molecules in the process of forming mesoporous silica", *Chem. Commun.*, 1996, **21**, 2759.

[55] A. Lind, J. Andersson, S. Karlsson, P. Agren, P. Bussian, H. Amenitsch, and M. Linden, "Controlled solubilization of toluene by silicate-catanionic surfactant mesophases as studied by in situ and ex situ XRD", *Langmuir*, 2002, **18**, 1380.

[56] S. Namba, A. Mochizuki, and M. Kito, "Fine control of pore size of highly ordered MCM-41 by using template mixtures of dodecyltrimethylammonium bromide/hexadecyltrimethylammonium bromide with various molar ratios", *Chem. Lett.*, 1998, 569.

[57] E.K. Bomati, G. Manning, and D.D Deheyn, "Amphioxus encodes the largest known family of green fluorescent proteins, which have diversified into distinct functional classes", *BMC Evolutionary Biology*, 2009, **9**, 77